# PREDICTION OF THE ONSET OF DAMAGE IN UNI-DIRECTIONAL LAMAINATES UNDER TRANSVERSE IMPACT LOADING USING FINITE ELEMENT ANALYSIS

Jeremy Ryatt

A thesis
Submitted in partial fulfillment of the
Requirements for the degree of

Master of Science

University of Washington
2016

Committee:
Ramulu Mamidala
John Kramlich
Daniel Sanders

Program Authorized to Offer Degree
Mechanical Engineering

University of Washington

## Abstract

Prediction of the onset of damage in uni-directional laminates under transverse impact loading using Finite Element Analysis

**Jeremy Ryatt**

**Chair of the Supervisory Committee:**
**Professor Ramulu Mamidala, PhD**
**Mechanical Engineering**

With the increase in application of Carbon Fiber Reinforced Plastics (CFRP) as principle materials in commercial airlines, the ability to predict the damage from transverse impact events has become an important parameter in the design of airframe sections that can be exposed to impact events. The purpose of this research is to investigate the applicability of Finite Element Analysis (FEA), particularly using the commercial solver Abaqus/Explicit, to predict the onset of damage in laminated plates. Closed forms solutions have been developed in the past to predict the onset of damage, but only in terms of mid ply delaminations. The research presented in this thesis looks to use a Continuum Damage Mechanics material model in Abaqus, coupled with surface based cohesive interactions to simulate the interlaminar bonds between the lamina.

To evaluate the predictive capability of the methodology, the onset of damage prediction will be compared against experimental data, examining when the damage begins to accumulate in the FEM and if there is a corresponding change in slope of the experimental Force vs. Displacement curve.

# TABLE OF CONTENTS

# LIST OF FIGURES

# LIST OF TABLES

# ACKNOWLEDGEMENTS

A special thanks to Professor Ramulu Mamidala and the Boeing Company.

# DEDICATION

For Hyeon Jeong and Oliva.

# Chapter 1. INTRODUCTION

The aerospace industry has always had a need for lighter and more efficient planes since the genesis of manned flight in Kitty Hawk, N.C. The need for lighter planes is driven by economics: the lighter a plane, the more cargo can be moved for a lower amount of fuel burned. Advancements in aerospace materials as well as manufacturing and design techniques has allowed for the creation of larger, quieter and more efficient commercial airliners than ever. The first commercial airliner to use CFRP as a major structural material in critical structure was the Boeing 737 classic, which was given a CFRP Horizontal Stabilizer in 1984. This was followed by the Boeing 777, which extensively used CFRP in its empennage (Horizontal and Vertical Stabilizers). While earlier planes had used CFRP for non-critical structure, the customer airlines had complained about the sensitivity of the materials to impact damage and the difficulty to repair them [1], let alone the types of damage that can happen to the body of the airframe in service. Noteworthy aircraft impact damage on the materials and structures are shown in Figure 1.1.

Increase in application of Carbon Fiber Reinforced Plastics (CFRP) as principle materials in commercial airlines began with the Boeing 777, as Toray Composites had developed a new composite system with a toughened resin, featuring a toughened interlayer that displayed superior performance under impact conditions as shown in Figure 1.2.b [1]. With the advent of toughened resin, the ability to use CFRP in primary structural applications became viable, leading to air-framers increasingly using CFRP; for example the Airbus A380, while primarily metallic, is nearly 20% CFRP [2]. The application of CFRP in commercial airlines changed with the introduction of the Boeing 787-8, which used CFRP as the primary structural material system. Figure 1.3 shows the aerospace structural materials associated with 787, which has a CFRP fuselage wing and empennage, making it the first primarily CFRP commercial airliner, as well as the Airbus A380.


Bird Strike

Tire fragment strike

Hail Strike

Lightening Strike

*Figure 1-1: Common in-service impact events*

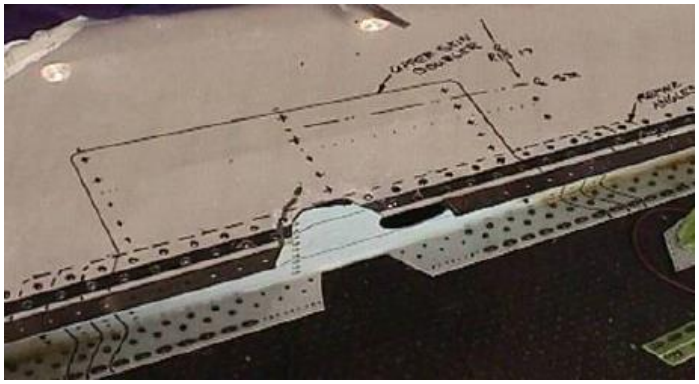

**a) Service induced Damage**

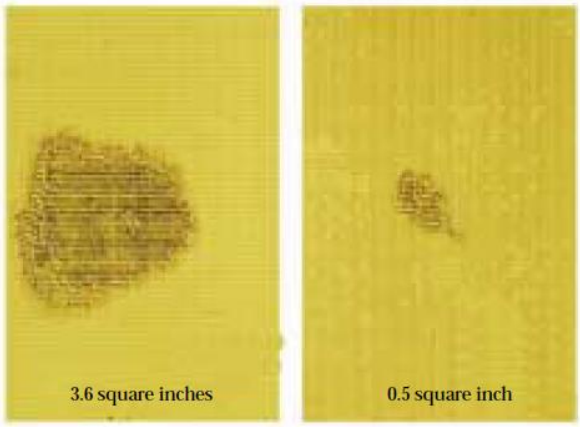


**b) Impact induced in material damage**

*Figure 1-2: a.) Service induced damage, b.) Damage from Low Velocity Impact*

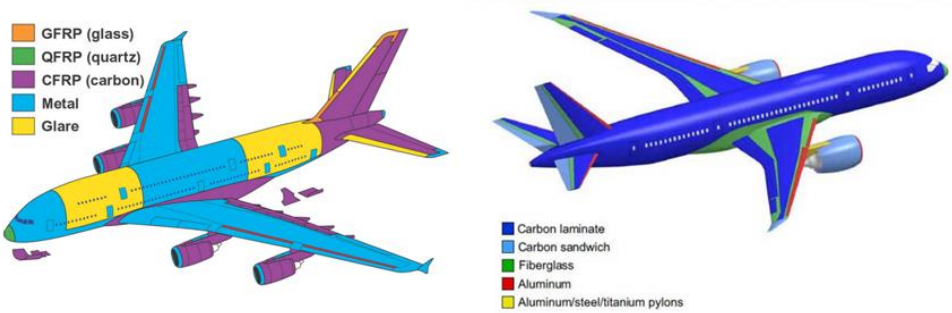


*Figure 1-3: Airbus A380 (left) and Boeing 787 (right) and the material comprising major structure*

Regardless of the improvements in CFRP resin technology, the ability to protect structure from impact damage, mostly via means of appropriately sizing structure to be damage tolerant to BVID means there needs to be adequate means of predicting impact damage in the analysis phase of the design cycle [3]. Barely Visible Impact Damage, or BVID, is a type of damage defined by the Federal Aviation Administration (FAA) as small damage that may not be found during heavy maintenance general visual inspections in typical lighting from five feet away [7]. The main issue with BVID, is there may be severe damage beneath the surface of the material in the form on delamination and/or material damage (Figure 1-4), unlike metallic materials where the damage manifests itself on the surface of the material (Figure 1-5).

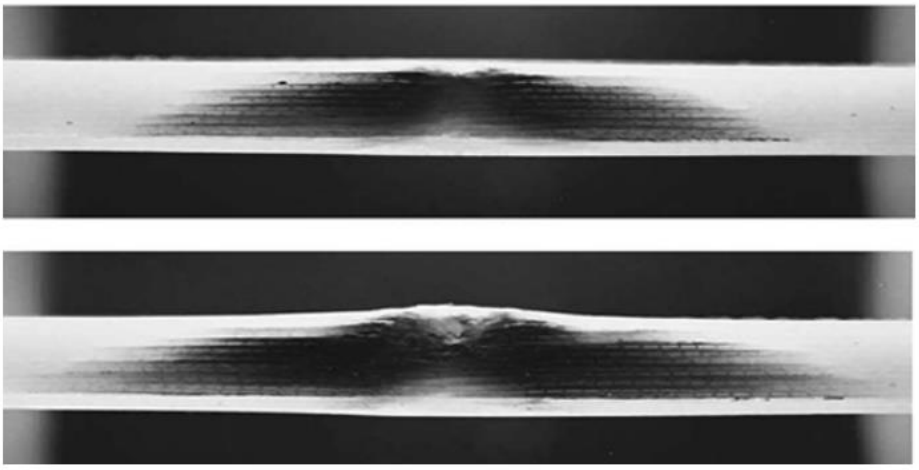

*Figure 1-4: Damage from a Low Velocity Impact on a laminated composite plate [8]*

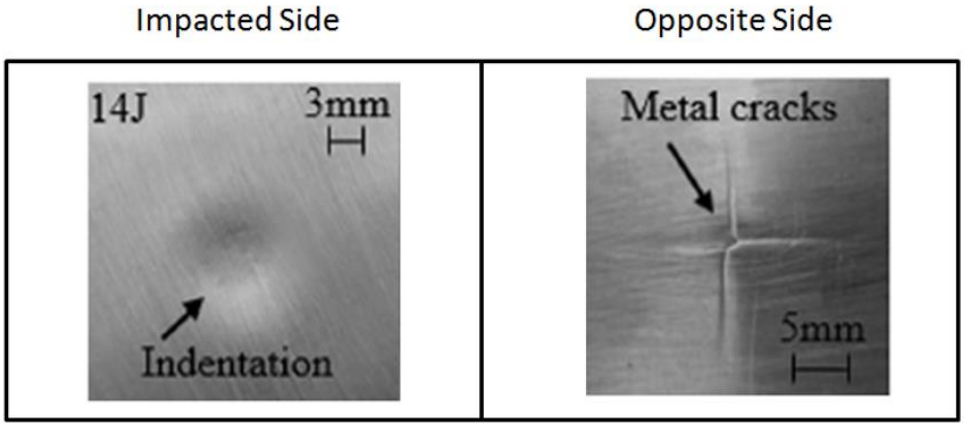


*Figure 1-5: Damage from a Low Velocity Impact on an Aluminum Plate [9]*

While some closed form solutions can predict either the load at which mid-ply delamination can occur [4] or predict the in plane damage during a transverse impact event, the use of numerical methods has become the primary way of investigating the integrity of a structure during and after an impact event. There are several types of dynamic damage simulations that can be run for a commercial airline, ranging from bird and tire-fragment impact simulations to barrel drop simulations, as well as lighting strike simulations; the focus of this research is on the simulation of low velocity impacts, similar to what would be experienced during manufacturing or servicing an airframe, e.g., a mechanic dropping a tool onto a surface of Horizontal Stabilizer. An example of a bird strike simulation in LS-Dyna is displayed in Figure 1-6.

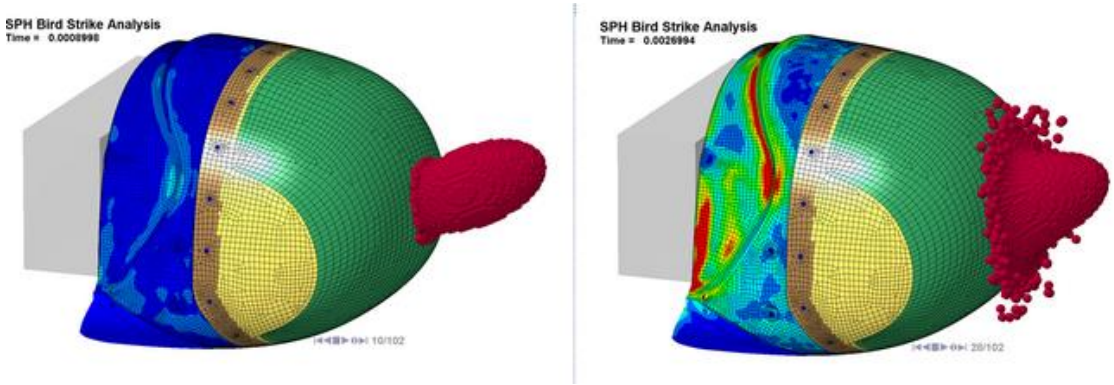


*Figure 1-6: Bird Strike Simulation of composite structure [10]*

When a laminate under goes an impact event and the level of the damage is BVID or higher, the compressive strength of the laminate in compression or shear is severely degraded, sometimes by up to as much 50% [11].

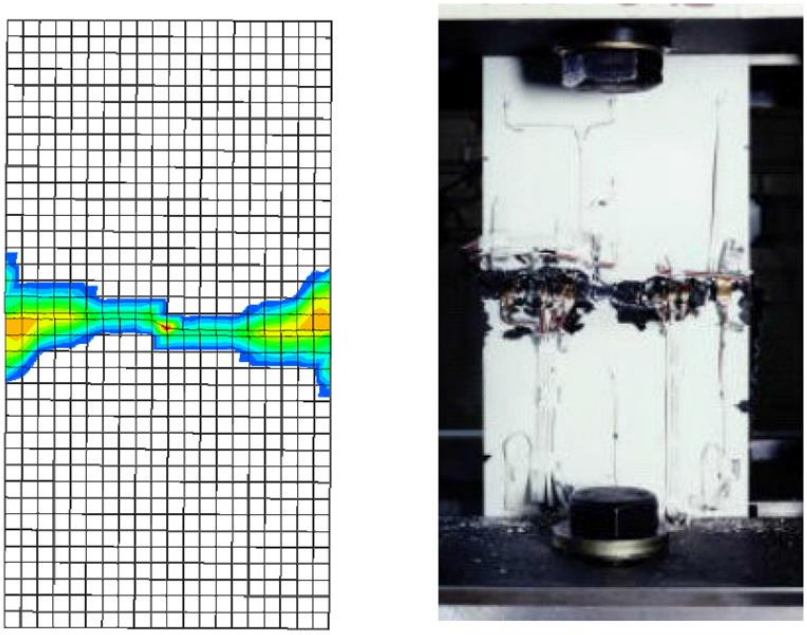

*Figure 1-7: Post damaged response of a laminated plate in compression after a low velocity impact event* [11]

Components of airframes are often sized using in-plane loads as the sizing for impact events was traditionally not seen as much of a concern for metallic airframes, which are not as sensitive to out of plane loading as composites. The primary job of an aerospace engineer is to make the airframe as safe and as light as possible and in order to do so, the engineer needs to have the best possible tools and data available to make the proper sizing decisions. This research aims to predict the onset of damage in thin composite plates subjected to Low-Velocity Impact using the two types of simulations:

- Reduced Coupon: Highly Idealized, detailed FEM's of the coupons tested by Briggs [4]. The intention of these coupons is to evaluate Abaqus ability to predict the onset of damage in the coupon and evaluate the energy absorption of the coupon as a sizing tool.

- Detailed Fixture: This is a fully featured model including the testing fixture, clamping features, and a considerably more refined mesh for the laminate. Due to the computational expense of the full fixture simulation

The objective of this analysis is to match the experimental data collected by Briggs [4] using Abaqus/Explicit as a predictive tool to evaluate the load and or transverse displacement that leads to the onset of damage in the laminate, either in the form of lamina damage or interlaminar damage. To predict the response of a structure under impact loading, the use of Explicit Finite Element Analysis is required to capture the response.

Explicit FEA varies from the more traditional Implicit in that it is more applicable for highly non-linear, transient simulations, whereas implicit simulations, with their much larger time step capabilities are better suited for static problems [5, 6]. Explicit simulations are conditionally stable, meaning the time step needs to be smaller than a certain value [12]. This leads to small time steps which are computationally inexpensive, but require far more increments than an implicit analysis [13]. Fundamentally, the two types of solver types differ on what they solve for and how they solve for them. In an Implicit analysis, nodal displacements are solved for by inverting the global stiffness matrix and multiplying the newly formed global compliance matrix by the applied force. For every increment in a non-linear analysis, the global stiffness matrix needs to be reformulated and inverted, which is computationally expensive, but because of its unconditional stability, can have much larger increments than an explicit analysis [12].

There are severally commercially available FEA codes that are capable of performing explicit analysis, including LS-Dyna, PAM-CRASH and RADIOSS, but the one chosen for this work is Abaqus/Explicit. Abaqus, founded in 1978 by Hibbert, Karlsson and Sorensen, now owned by Simulia, is multi-physics FEA package which has both Implicit and Explicit solvers. Abaqus has become a primary FEA tool for Boeing, Airbus and BMW for implicit analysis and increasingly as an explicit solver for crash and impact analysis.

While Abaqus has become a leading code in the world of crash simulation, it still has several short comings, one of which being the limit of the material models delivered with the solver [5]. To overcome this, Abaqus does provide user defined subroutines for several common materials; however it does come at a price: the externally called subroutines are significantly slower than material models that are natively compiled and have direct access to the solver. The VUMAT's

are called every increment, but have to be compiled externally and pointers are passed back and forth rather than the having direct access to each other [5].

While some authors [15, 15, 16] have employed the VUMAT to simulate the behavior of impact, the research conducted in this paper is to simulate the experiments performed by Briggs [4] using the functionality provided with the standard installation of Abaqus, in a similar fashion to work performed by Becz and Hurtado [11], Feng [15] and Muflahi [16].

The content of this thesis is arranged as follows: after introduction and the motivation for this research, as presented in the sections above, the background and literature review is presented in Chapter 2, which covers the history of FEA, as well as the basis of Implicit and Explicit FEA methods. This section also covers the means of interlaminar and composite damage, as well the results of authors who performed similar work. Chapter 3 covers the material data collected by Briggs [4] that will be used to develop the material models for the simulation of the low-velocity impact experiments, also performed by in reference [4]. The development of the material models, including the interlaminar damage model using the numerical models is presented in Chapter 4; this chapter also includes the means of developing the Hashin Failure material failure criterion employed in Abaqus [5]. Chapter 4 also includes the overview of the Finite Element Models used, including mesh generation, loads and boundary conditions. Chapter 5 is the presentation of the results and the discussion of the findings; the research is concluded with Chapter 6, which summarizes the entirety of the research performed and presents possible avenues for future work.

# Chapter 2. BACKGROUND AND LITERATURE REVIEW

There has been considerable research performed in the area of the experimental characterization of the impact of composite materials over the last 30 years, as the material system has become considerably more prevalent in commercial airlines applications; coincidentally the research into the field of simulating impact events has been researched for nearly the same period of time. With the increase in computing power over the last 20 years, numerical impact prediction models have evolved from doubly-symmetric quarter models [17, 18] to fully defined ply-by-ply models [14, 15, 16]. A graphic of an early impact from the early 2000's and one from 2015 is displayed in Figure 2-1.

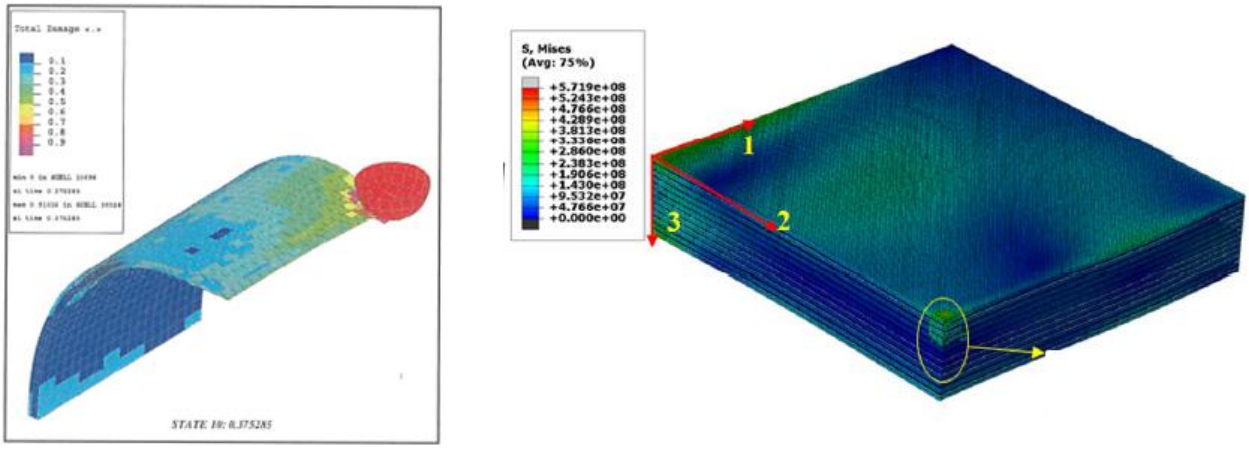


*Figure 2-1: Composite Damage models, symmetric shell model in PAM-CRASH [17] and (left) and a solid element model in Abaqus [14] (right)*

There are a number of reasons to simulate a composite impact event, ranging from simulating the elastic response of an anisotropic plate, which can be taxing when done analytically, to predicting the damage in a composite plate from an impact event and the subsequent residual compressive strength [11].

## 2.1 EXPLICIT FEA

The genesis of the Finite Element Method came from a time where the aerospace industry was in need of a better means to determine the internal forces in an airframe, which are highly indeterminate in nature. The person credited with the creation of the FEA method that we are most familiar with is Jon Turner, who generalized and perfected the Direct Stiffness Method while working at Boeing in the 1950's [19] [20], which led to the paper that is generally considered to be the beginning of modern FEA: "*Stiffness and Deflection analysis of complex structures*" by Turner, Clough, Martin and Topp [20].

As computing resources become more available in the 1970's, Dr. John Hallquist, an engineer at Lawrence Livermore National Laboratory (LLNL), developed a code to evaluate structural response for the "dial-a-yield" low altitude nuclear weapons program: DYNA3D. The original DYNA3D was a 5000 line program that allowed scientists to perform high speed transient simulations using the newly developed CRAY-1 supercomputer [21]. In 1978 LNLL released the source code for DYNA3D at the request of the French government, beginning the commercial application and development of Explicit FEA, which found immediate applications in the automotive industry [21, 22].

Explicit FEA is a means of solving partial differential equations using the Central Time Difference integration scheme [6]. This method uses small incremental steps that are computationally efficient; but for an analysis the total number calculations can be on the order of several hundred thousand, making the simulation expensive computationally [12]. In the Explicit FEA method, the nodal accelerations are solved for by solving for the body force vector on each node and dividing this by the nodal mass. Once the accelerations are solved for, the velocities and displacements can be obtained by integrating the acceleration vector. The strains are then solved for by taking the partial differentials of the displacement field and the stresses are solved for by multiplying the strains by the constitutive equation of the material.

The Explicit FEA method allows for the degradation of the material and the interlaminar interface via Continuum Damage Mechanics [23] as well as means of solving problems that are

highly non-linear (discontinuous contacts, large deformations, material degradation, etc.) as the global force tensor does not need to be solved for, and subsequently not converged on.

In the Implicit FEA method, a global stiffness matrix is formed and inverted to determine nodal displacements. The solver will iteratively calculate the force balance at the nodes within a specified tolerance; once the tolerance is met, the solution will advance and the process will repeat until the simulation completes (either through completion or termination based on requiring too many increments to feasibly solve the force balance) [5]. Like the Explicit FEA method, the strains are solved for by taking the partial derivatives of the displacement field and the stresses are solved for by multiplying the strains by the constitutive equation of the material.

While the Explicit FEA method requires several hundred thousand computationally inexpensive calculations, the implicit method conversely requires significantly lower amount of computationally expensive calculations.

## 2.2 FAILURE THEORIES

The area of composite failure mechanisms and the implementation of failure theories has been a critical area of research since the advent of modern composite materials [24]. In terms of widely accepted composite material failure models, they can be broken into two separate groups:

- Failure criteria not associated with failure modes
- Failure criteria associated with failure modes

Composite failure models not associated with failure modes are based on adjusting an expression to experimental data [3]. The most basic polynomial failure expression available was developed by Tsai and Wu in 1971; in tensor notation this failure criterion may be expressed as follows:

$$(F_i\sigma_i) + \left(F_{ij}\sigma_i\sigma_j\right) + \left(F_{ijk}\sigma_i\sigma_j\sigma_k\right) \geq 1 \qquad [1]$$

While these methods are able to predict the damage in laminate, the coefficients in the polynomials are experimentally determined and are functions of the laminate, not the lamina;

meaning the prediction of the material damage with different ply orientations and thicknesses are not feasible.

The failure models associated with material failure modes are based on the fact the composites are an inhomogeneous material and subsequently have failure modes that are extremely anisotropic in nature [3, 14, 15, 16]. These types of failure models are typically able to identify the following failure modes:

- Fiber Fracture
- Transverse Matrix Cracking
- Shear Matrix Cracking

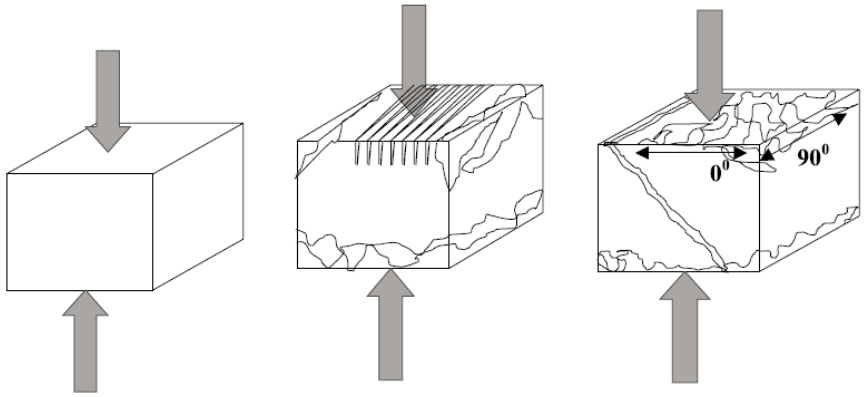


*Figure 2-2: Compressive matrix failure modes in a lamina [27]*

The criteria based on failure modes have become the standard means of predicting damage in composite materials in modern analysis, both analytical and numerical. An example of through thickness damage in a lamina is presented in Figure 2-2, which displays matrix cracking that can occur in compression. The following section highlights several common material failure models; the following conditions are presented in terms of states of plane stress.

### 2.2.1 *Maximum Stress Failure Criterion*

This criterion dictates that a given state of stress if and only if all of the following inequalities are satisfied [24].

$$-X^C < \sigma_{11} < X^T$$
$$-Y^C < \sigma_{22} < Y^T \qquad [2]$$
$$|\tau_{12}| < S_L$$

This failure criteria is the most simple, as the material is considered degraded once one of the material strengths has been exceeded, which in Tension holds true, but can yield significantly unrealistic failure in compression and shear.

### 2.2.2 *Tsai Hill Failure Criterion*

The following criterion indicates a composite will not fail if the following inequality is satisfied [24]:

$$\frac{(\sigma_{11})^2}{\left(\sigma_{11}^{ft}\right)^2} + \frac{(\sigma_{22})^2}{\left(\sigma_{22}^{ft}\right)^2} + \frac{(\tau_{12})^2}{\left(\tau_{12}^{f}\right)^2} - \sigma_{11}\sigma_{22}\left[\frac{1}{\left(\sigma_{11}^{ft}\right)^2} + \frac{1}{\left(\sigma_{22}^{ft}\right)^2} - \frac{1}{\left(\sigma_{33}^{ft}\right)^2}\right] < 1 \qquad [3]$$

While being in terms of plane stress, the Tsai-Hill does include a term for through thickness stress; obtaining a failure stress, $\sigma_{33}$, for a lamina is not feasible, leading to the common assumption that lamina based properties are transversely isotropic, where $\sigma_{22} == \sigma_{33}$ [24].

### 2.2.3 *Hashin Failure Criterion*

The Hashin initiation theory has four unique damage initiation terms [5, 24, 25]:

- Fiber Tension
  $$F_f^t = \left(\frac{\hat{\sigma}_{11}}{X^T}\right)^2 + \alpha\left(\frac{\hat{\tau}_{12}}{S^L}\right)^2$$
- Fiber Compression
  $$F_f^c = \left(\frac{\hat{\sigma}_{11}}{X^C}\right)^2$$
- Matrix Tension
  $$F_m^t = \left(\frac{\hat{\sigma}_{22}}{Y^T}\right)^2 + \alpha\left(\frac{\hat{\tau}_{12}}{S^L}\right)^2$$
- Matrix Compression
  $$F_m^c = \left(\frac{\hat{\sigma}_{22}}{2S^T}\right)^2 + \left[\left(\frac{Y^C}{2S^T}\right)^2 - 1\right]\frac{\hat{\sigma}_{22}}{Y^C} + \left(\frac{\hat{\tau}_{12}}{S^L}\right)^2$$

*[4]*

The terms from the equations above are defined as:

| **Term** | **Definition** |
|---|---|
| $X^T$ | Longitudinal Tensile Strength |
| $X^C$ | Longitudinal Compressive Strength |
| $Y^T$ | Transverse Tensile Strength |
| $Y^C$ | Transverse Compressive Strength |
| $S^L$ | Longitudinal Shear Strength |
| $S^T$ | Transverse Shear Strength |
| alpha | Shear/Tension contribution factor |

*Table 1: Damage initiation terms for Hashin failure criterion*

For the application of this material model in Abaqus, the material model is augmented with means of Continuum Damage Mechanics as implemented by Matzenmiller [26], as well as the implementation of combined Hashin criterion based on the 1973 and 1980 papers by Z. Hashin [25].

The effective stress tensor of the material can be defined as:

$$\hat{\sigma} = \boldsymbol{M}\sigma \qquad [5]$$

Where σ is the true stress and **M** is the damage operator, defined as:

$$\boldsymbol{M} = \begin{bmatrix} \frac{1}{(1-d_f)} & 0 & 0 \\ 0 & \frac{1}{(1-d_m)} & 0 \\ 0 & 0 & \frac{1}{(1-d_s)} \end{bmatrix} \qquad [6]$$

The variables $d_f$, $d_m$, and $d_s$ are the internal damage variables that represent the fiber, matrix and shear damage, respectively, which are derived from the damage variables represented in the four failure modes presented above.

The derivation for $d_f$, $d_m$, and $d_s$ is presented below:

$$d_f = \begin{cases} d_m^t \; if \; \sigma_{22} \geq 0 \\ d_m^c \; if \; \sigma_{22} \leq 0 \end{cases}$$

$$d_m = \begin{cases} d_m^t \; if \; \sigma_{22} \geq 0 \\ d_m^c \; if \; \sigma_{22} \leq 0 \end{cases} \qquad [7]$$

$$d_s = 1 - (1 - d_f^t)(1 - d_m^t)(1 - d_m^c)$$

### 2.2.4 *Chang/Chang Failure Criterion*

For the Chang/Chang model, the damage initiation terms as implemented in LS-Dyna MAT54 are presented below [6]:

- Tensile Fiber mode

$$\sigma_{aa} > 0 \Rightarrow e_f^2 = \left(\frac{\sigma_{aa}}{X_t}\right)^2 + \beta\left(\frac{\sigma_{ab}}{S_c}\right) - 1$$

- Compressive Fiber mode

$$\sigma_{aa} < 0 \Rightarrow e_c^2 = \left(\frac{\sigma_{aa}}{X_c}\right)^2 - 1 \qquad [8]$$

- Tensile Matrix mode

$$\sigma_{bb} > 0 \Rightarrow e_m^2 = \left(\frac{\sigma_{bb}}{Y_t}\right)^2 + \left(\frac{\sigma_{ab}}{S_c}\right)^2 - 1$$

- Compressive Matrix mode

$$\sigma_{bb} < 0 \Rightarrow e_d^2 = \left(\frac{\sigma_{bb}}{2S_c}\right)^2 + \left[\left(\frac{Y_c}{2S_c}\right)^2 - 1\right]\frac{\sigma_{bb}}{Y_c} + \left(\frac{\sigma_{ab}}{S_c}\right)^2 - 1$$

The implementation of Chang/Chang is the most commonly used composite material failure model in LS-Dyna and is similar to the Hashin Failure criterion employed in Abaqus in terms of damage initiation, but behaves differently in terms of material degradation.

### 2.2.5 *Composite Failure Criteria overview*

The prediction of damage in composites is a field in which the accuracy of the failure theory can vary based on load type, as well as the material type, as displayed in the work by Hinton and Kaddour [28, 29]; in one case the Puck failure theory displayed excellent correlation, but in cases where there were large geometric non-linearities, the failure strains were grossly under-predicted. The truth about composite failure theories, as evidenced in [24, 28, 29] is that there is no one failure theory that can adequately predict the failure of composites under all conditions. Regardless of the deficiencies of the composite failure methods, the commercial FEA codes have to include at least one failure theory.

LS-Dyna offers the following material models in their standard release: MAT_54 and MAT_55 which are progressive failure models and employ the Chang/Chang and Tsai-Wu failure criterion respectively [6] and Abaqus offers the Hashin model as presented above.

## 2.3 INTERLAMINAR DAMAGE SIMULATION

One of the most common failure modes in composites is interlaminar de-bonding, also known as delamination, where fracture occurs between adjacent plies. This is due to the inter-ply region being a resin rich zone with significantly lower mechanical properties than the adjacent plies [14], which leads to a significantly lower allowable stress than the lamina on either side of the region; a graphical representation of a laminate with interplay regions highlighted is presented in Figure 2-2.

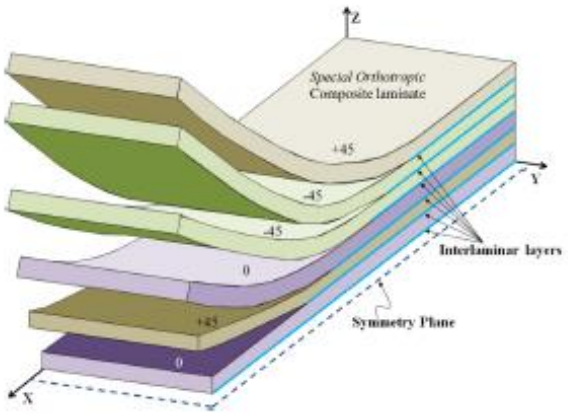


*Figure 2-3: Schematic for a laminate with the interplay region highlighted with solid lines [14]*

Being able to capture this failure mechanism is important as the force that holds that laminate together during bending are transverse shear forces, which can be illustrated in the bending of a simply supported beam, is displayed .

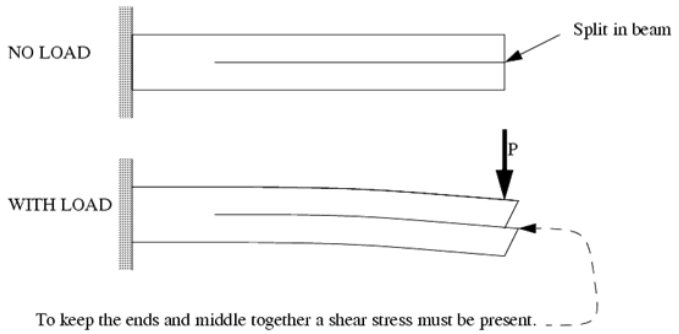


*Figure 2-4: Graphical representation of transverse shear forces*

During an impact event, the large deformations that occur create large interlaminar shear forces that lead to mode II fracture, as displayed in Figure 2-1. While other forms of damage can occur in an impact event, the ability to predict delamination in aircraft panels that carry shear and/or compression becomes of the utmost importance for the panel to remain damage tolerant [7, 30]. Panels that have impact induced delaminations can be up to 50% weaker in compression as the delamination effectively turns the panel into two thinner panels [11]. Examples of damage and delamination are displayed in Figure 2-5.

.

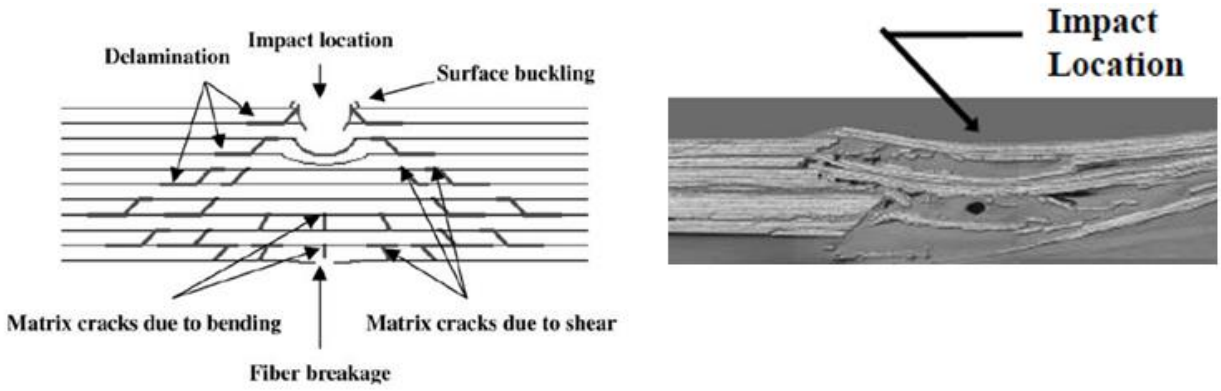


*Figure 2-5: Graphical representation of impact damage (left)[8] and a cross section of a plate that was subjected to localized impact damage (right)[7]*

There has been significant research in the field of predicting interlaminar damage, particularly simulating it, as the means of simulating interlaminar bonds has many parallels in other industries, particularly the private ship building industries which extensively use composite materials.

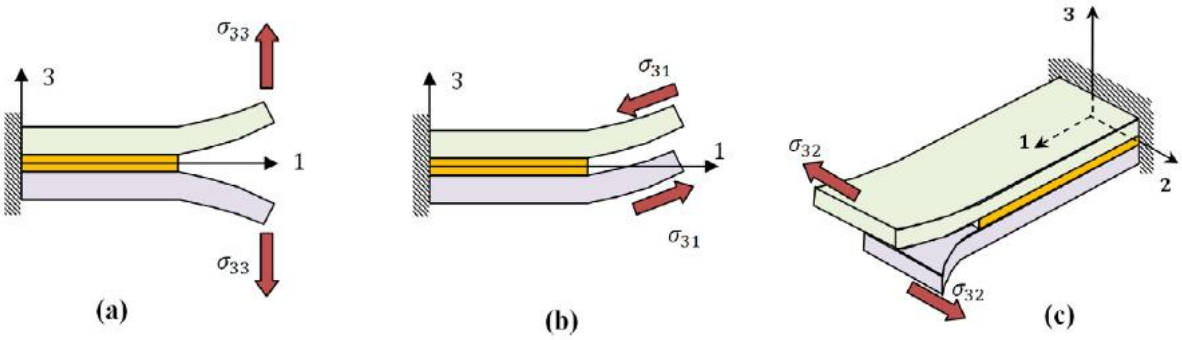


*Figure 2-6: a.) Mode I fracture, b.) mode II fracture, c.) mode III fracture*[14]

Delamination is commonly simulated using FEA via the following methods:

- **Virtual Crack Closure Technique (VCCT)**

  VCCT which is based on the Linear Elastic Fracture Mechanics (LEFM) assumption that when a crack grows by an infinitesimal amount, the energy released is equivalent to the energy required to close the crack [14, 31] for mode I, II and III cracks as well as mixed mode fracture, which are graphically displayed in Figure 2.6

- **Cohesive Zone Models (CZM)**

  Cohesive Zone Models treat the fracture that grows as a more gradual phenomena than the VCCT method does, as the crack tip can be considered to be the relative displacements using an extending crack tip (i.e., Cohesive Zone) [32].

- **Continuum Damage Mechanics (CDM)**

  CDM methods do not require special interfacial elements like VCCT and CZM, meaning standard 3D continuum solid elements can be employed. CDM can also be coupled with plasticity models to simulate ductility in the resin as well as the hardening that can occur in the crack tip at higher strain rates [4, 14].

The implementation of the VCCT method in Abaqus requires the presence of an initial flaw [5] making its application unviable, as in impact simulation the objective is to predict the onset of damage as well as propagation. Figure 2-7 shows a single 2D example of the initial flaw required in the Abaqus VCCT function.

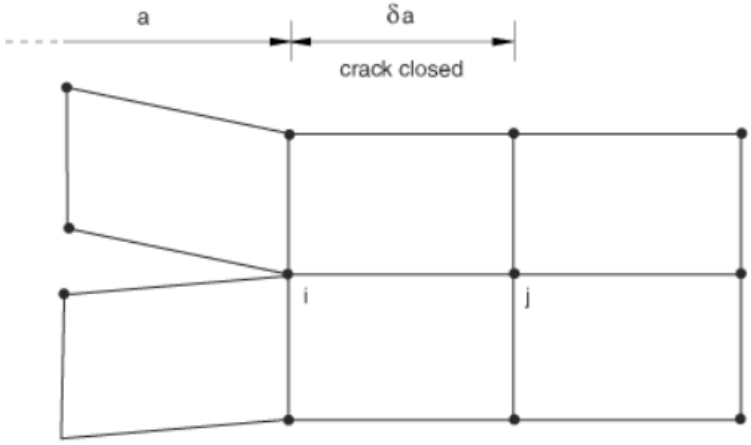


*Figure 2-7: Simple display of the required initial flaw for VCCT [5]*

For the prediction of damage using commercial codes, the means of predicting interlaminar damage can be broken down by solver (all of the methods presented for Abaqus and LS-Dyna are CZM approaches)

- **Abaqus:**
  - Use zero thickness solid cohesive elements, with no element deletion to prevent inter penetration between lamina layers [15, 33]
  - Cohesive contact will be investigated in this research
- **LS-Dyna**
  - Use the contact *CONTACT_[*SURFACE FIELD VARIABLE*]_TIEBREAK algorithm [6], which will be referred to as Tiebreak, henceforth.

The application of Tiebreak has been favored by the LS-Dyna community due to not only its favorable results [14] but the ease of use. When defining a model with cohesive elements representing the interlaminar bond, a matched meshing technique must be employed, where the

nodes on the lamina must be shared with the nodes of the cohesive layer; an example of a matched mesh can be seen in Figure 2-8.

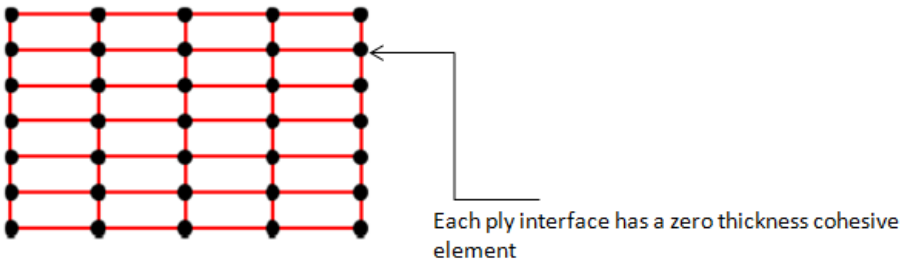


*Figure 2-8: Idealization of the mesh with the location cohesive interfaces identified*

Using *TIEBREAK only requires the definition of the interfacing nodes (or solid element facets), rather than the laborious task of defining the matched meshes, which often require an automated process to minimize mistakes and expedite the process.

While the papers researched using Abaqus used cohesive elements as described above, Abaqus does offer a "Cohesive Contact" that can be use used in the same fashion as *TIEBREAK in LS-Dyna [5, 6]. Cohesive Contact offers the ease of *TIEBREAK, but allows for the definition of the stiffness matrix for the cohesive interface, which allows the user to iteratively tune the transverse shear stiffness of the laminate to match test results without having to alter the definition of the material or element in the lamina plies when using solid or continuum shell elements.

The traction terms at the cohesive interface are defined as follows:

$$t = \begin{Bmatrix} t_n \\ t_s \\ t_t \end{Bmatrix} = \begin{bmatrix} K_{nn} & K_{ns} & K_{nt} \\ K_{ns} & K_{ss} & K_{st} \\ K_{nt} & K_{st} & K_{tt} \end{bmatrix} \begin{Bmatrix} \delta_n \\ \delta_s \\ \delta_t \end{Bmatrix} = K\delta \qquad \textit{Eqn. 9}$$

The most general form of cohesive contact is a decoupled stiffness matrix, where the normal and shear traction terms have no influence on one another. For this definition, the non $K_{ii}$ terms are set to zero which gives the following.

$$t = \begin{Bmatrix} t_n \\ t_s \\ t_t \end{Bmatrix} = \begin{bmatrix} K_{nn} & 0 & 0 \\ 0 & K_{ss} & 0 \\ 0 & 0 & K_{tt} \end{bmatrix} \begin{Bmatrix} \delta_n \\ \delta_s \\ \delta_t \end{Bmatrix} = K\delta \qquad [10]$$

The damage in the cohesive interface is defined using "traction-separation" curves, which require a damage initiation term and stiffness degradation term, as do all continuum damage failure laws [34]. When using cohesive contact, the difficulty comes from determining and subsequently setting the damage initiation criteria. For the model presented in the following sections, the maximum stress criterion is employed, which has the form [5]:

$$max\left\{\frac{\langle t_n \rangle}{t_n^o}, \frac{t_s}{t_s^o}, \frac{t_t}{t_t^o}\right\} = 1 \qquad [11]$$

As the damage initiation stress is something that really only exits in the context of cohesive elements, the effort required determine the initiation stress that represents the coupon being tested is not something that can be experimentally determined, but rather numerically derived [16], as is done in §4 of the paper.

Applications of cohesive elements as presented by Diehl [33] and Muflahi [16] display good correlation to experimental and closed from solutions for Double Cantilever Beam (DCB) and Edge Notch Failure (ENF) tests, but are noted to be difficult in application, as mentioned above. However the downfall of cohesive elements is the innate mesh dependency for both damage initiation and damage propagation [14, 16, 31], which requires the user to always evaluate the mesh dependency to ensure valid results are produced.

## 2.4 DAMAGE PREDICTION

Low impact velocity impact tests are typically carried out dropping an object of known mass from a known height, as was performed by Briggs [4], as well as in References [14, 15, 16]. These tests will behave either with the Tupper, or impacting object, returning to a height less than the initial due to the return of elastic strain energy, or will completely puncture the coupon and not return. Typical force-displacement curves for low velocity impact tests are displayed in Figure 2-9.

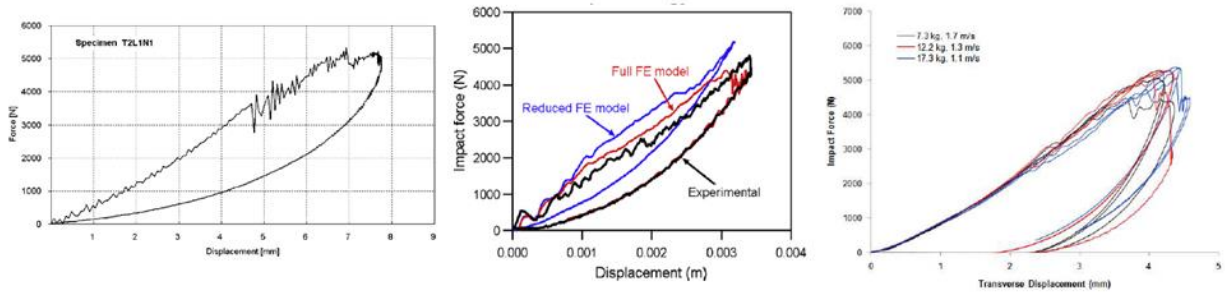


*Figure 2-9: Force displacement curves from references [35], [15] and [4], moving left to right*

The authors that performed similar work to what is presented in this thesis were able to predict the force-displacement response of the impacting object fairly accurately as well as the area of damage, comparing the FEM data to CT-Scans or X-Ray images of the damaged laminate. Feng and Aymerich [15] used a VUMAT material model and solid cohesive elements to predict the damage in quasi-isotropic laminates and consistently over predicted the impact force and under predicted the overall displacement of the Tupper, indicating a stiffer response, as seen in Figure 2-10.

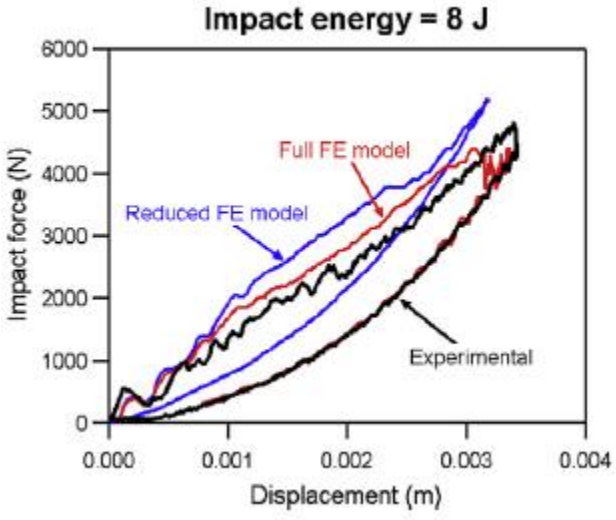


*Figure 2-10: Force displacement curve from Feng [15] displaying a typical load stroke curve, but with severe oscillations at the beginning of the experimental impact*

The force-displacement curves also do not display a clear indication of damage, as the curves from Reference [15] display an oscillation during the elastic response of the coupons; however

the energy levels tested are all lower than the energies tested for this research [4] and conclusions cannot be readily drawn.

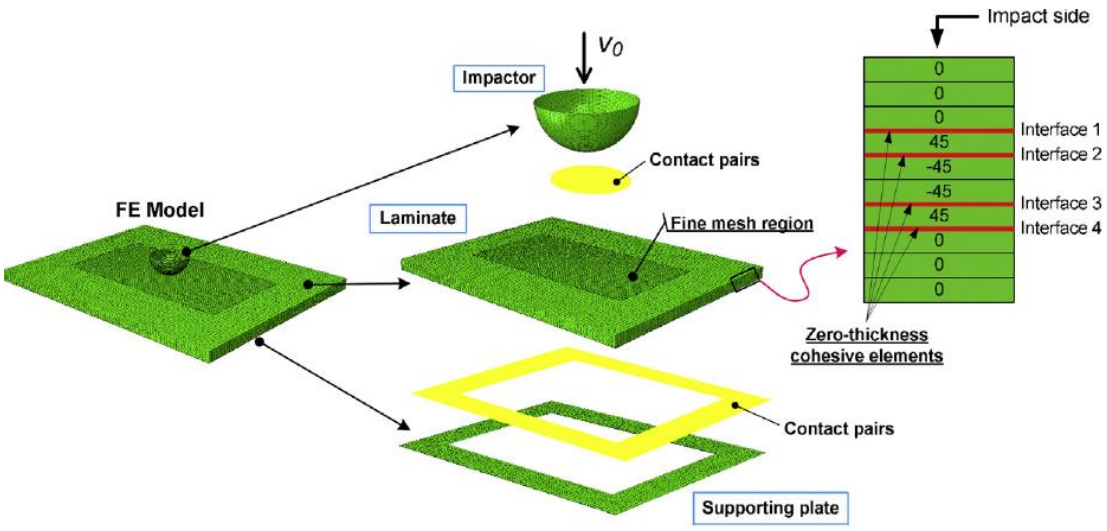


*Figure 2-11: Detailed Impact model from [15]*

Figure 2-11 shows the configuration of the detailed model used in Reference [15], which displays the solid ply-by-ply representation of the laminate and the location of the cohesive interlaminar elements, located between the plies with dissimilar orientations. The damage predicted in [15] is correlated to experimental findings by taking the length and width of the extreme points of the damage pattern and repeating the same with the FEM, looking for correlation across the impact energies tested. Overall, while this measure of damage may omit some of the unique features of a damage pattern, the authors were able to obtain a good correlation between test and experiment. The correlation conclusion from Reference [15] is presented in Figure 2-11.

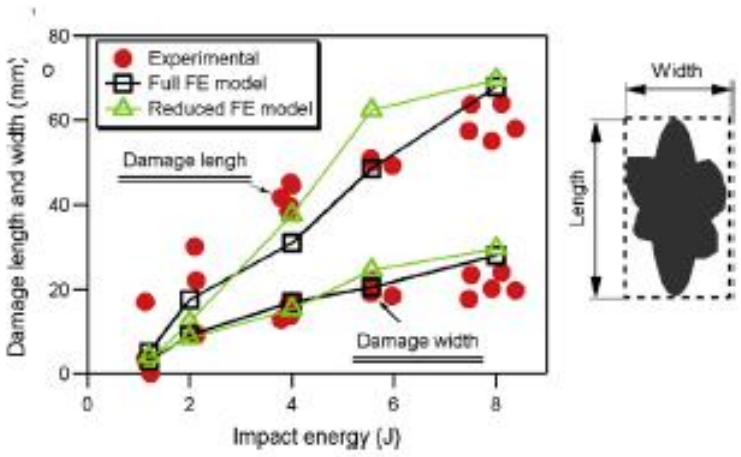


*Figure 2-12: Damage pattern correlation in terms of the extremum of the patterns in the local X and Y directions* [15]

The research by Muflahi, et. al., [16] clearly represents the validation of their constitutive model development for the lamina and the interlaminar properties, but do not adequately present response of their static indentation model. Rather than perform a dynamic test and simulation, a quasi-static indentation is performed, similar to what is done in §8 of [4]. The only offer of post indentation damage is a graphic of the delamination pattern from a simple shell model, which matches the shape of the damage pattern presented, but no other information is provided. While the intent of the research is different than what is performed in this thesis, the work performed by Becz, et. al. [11] does perform an impact simulation to subsequently load the impacted plate in compression to evaluate the residual strength of the component. This has been noted to be of the utmost importance, as there can be up to a 50% strength reduction in compression has been noted in delaminated panels [11, 30]; the correlation performed for the response was in the form of the damage pattern at panel failure and the matrix damage variable in Abaqus at the moment of failure, which is displayed in Figure 1-5.

What is evidenced in the literature available is that the commercial codes, with some modifications in the form of user defined material models, have been able to predict the general response of a laminate during an impact event and the subsequent damage pattern, but have not displayed a clear trend to display a force, or transverse displacement threshold that may serve as means of aiding in the design of composite panels subjected to transverse impact loading.

# Chapter 3. EXPERIMENTAL DATA

Tests were carried at the UW Solheim manufacturing laboratory evaluating the elastic properties of the material as well as failure properties. The coupon tests are what is used as the building block of this analysis as the material models for the laminate are determined from this test data. The purpose of the research in [4] is to evaluate the strain rate sensitivity of the CFRP material evaluated. As the material model in Abaqus does not allow for strain rate sensitivity [5], the data from the test will be used that most closely matches the theoretical strain rate for the impact simulation.

The material used in Briggs' experimental work was graciously donated to the UW by the Boeing Company; this material was a Toray Pre-Preg Uni-Tape known as T800SC/3900-2B. This material is used for primary structural applications within the Boeing Company and can be laid up via NC controlled tape laying machines or via the more traditional (albeit laborious) hand layup. The carbon yarn in the Toray T800 fiber system are woven from 24,000 filament yard, which has an average tensile strain of 1.80%, an average modulus of 279 GPa, which gives a tensile strength of 5,488 MPa. The lamina has a nominal area weight of 190 grams per square meter. A roll of CFRP tape freshly removed from cold storage can be seen in Figure 3-1.

| **BMS 8-276H Type 35 Class 3 Grade 190 Form 3 Comp 1** | |
|---|---|
| **Material Designation** | P2352W-19 T8000SC/3900-2B, 19 |
| **Fiber ID** | BMS 9-17 Class 3 Grade 24, Type II Designation T8000SC-24000-10E |

*Table 2: Material specification for the uni-directional tape used in the experimental study*

*Figure 3-1: Uni-Directional tape freshly removed from cold storage[4]*

## 3.1 TENSILE CHARACTERIZATION

All tensile testing was performed using an Instron 558H Universal Testing Machine. This is screw driven via an electric motor; the load cell is capable of 250kN. The crosshead is able to move at various feed rates ranging from 0.001 to 500 mm/min. A coupon in the clamping jaws, with axial and transverse extensometers can be seen in Figure 3-3.


*Figure 3-2: Example of tensile characterization [4]*

### 3.1.1 *Longitudinal Tensile Characterization*

The testing was performed at various loading rates and displayed sensitivity to the loading rates, particularly at lower load rates. For the higher strain rates, the material displayed a consistent response.

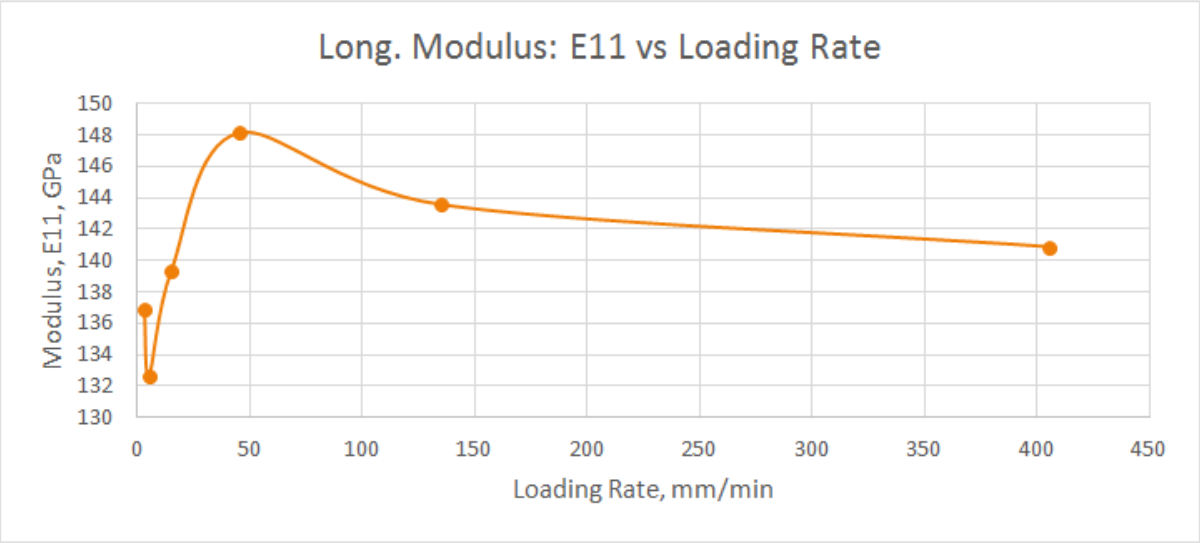


*Figure 3-3: Longitudinal extensional modulus of material versus loading rate*

From the experimental data, the average moduli collected for each loading rate are presented below in table 3-2.

| Loading Rate (mm/min) | Avg E11 (Gpa) | E11_STD (Gpa) | Avg v | v_STD |
|---|---|---|---|---|
| 3 | 136.9 | 7.1 | 0.13 | 0.04 |
| 5 | 132.7 | 3.1 | 0.08 | 0.01 |
| 15 | 139.4 | 5.5 | 0.13 | 0.05 |
| 45 | 148.2 | 21.4 | 0.25 | 0.18 |
| 135 | 143.6 | 7.3 | 0.1 | 0.05 |
| 405 | **140.9** | 8 | 0.11 | 0.04 |

*Table 3: Average extensional modulus*

For the material model, the major Young's Modulus used will be 140.9 GPa. Due to the uncertainty in the Poisson ratio, a value of .3 will be used in the 1-2 plane to match data from uni-tape presented by Tuttle [24].

For this analysis, this data is extremely important, but can be hard to obtain. When loading a material to extensional failure, the extensometers will often be removed well before the load is observed, if the failure load is reached at all. Often times the test will be stopped as the sudden failure in the composite specimen will create a shock load in the testing machine which can be detrimental to the longevity of the machine. That being said, some data was collected for failure loads at lower strain rates and will be used to determine the damage initiation stress for the longitudinal direction.

| Specimen Label | Loading Rate (mm/min) | Failure Stress (Mpa) |
|---|---|---|
| T0_01 | 3 | 1990.6 |
| T0_02 | 3 | 2061.4 |
| T0_03 | 3 | 1994.4 |
| T0_04 | 3 | 2065.2 |
| T0_05 | 5 | 2259.2 |
| T0_06 | 5 | 1624.9 |
| T0_07 | 5 | 2054 |

| | | |
|---|---|---|
| Average | **2007.1** | Mpa |
| Standard Deviation | 190.9 | Mpa |

*Table 4: Longitudinal tensile failure strength*

Taking the average of the data obtained for the 3-5 mm/min loading rates, the failure stress for the material used for the analysis will be taken to be $X^T$= 2,007 MPa.

### 3.1.2 *Transverse Tensile Characterization*

The data was collected in a similar manner to the longitudinal modulus, with the exception that this time, a $[90]_{10}$ laminate was used. This data will be used to determine $E_{22}$.

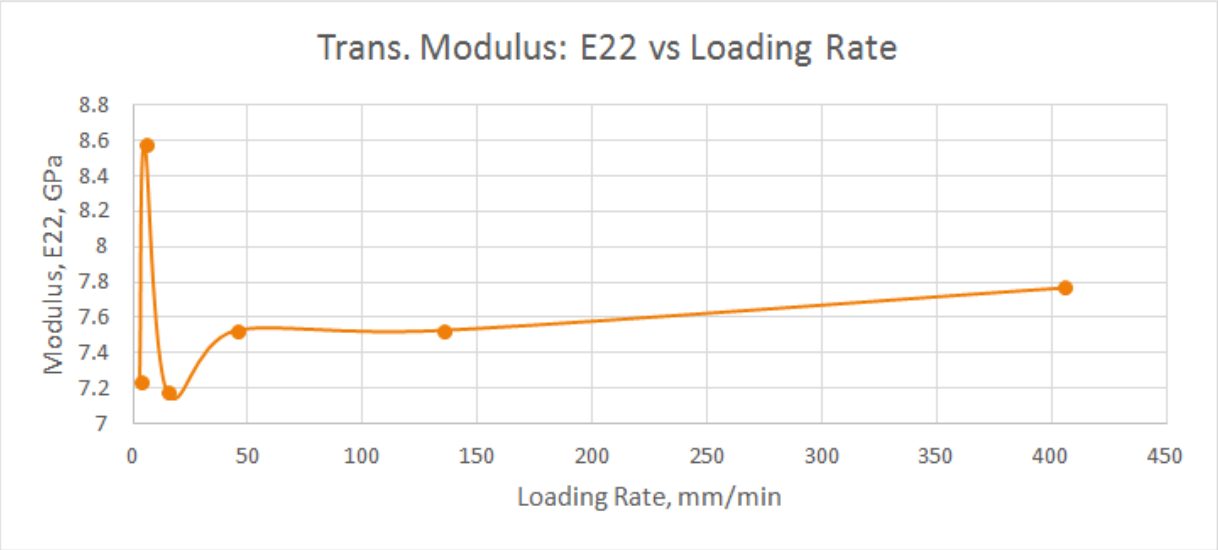


*Figure 3-4: Transverse extensional modulus of material versus loading rate* [4]

From the experimental data, the average moduli collected for each loading rate are presented below.

| Loading Rate (mm/min) | Avg E22 (Gpa) | E22_STD (Gpa) | Avg v | v_STD |
|---|---|---|---|---|
| 3 | 7.24 | 0.51 | 0.1 | 0.02 |
| 5 | 8.58 | 0.5 | 0.15 | 0.02 |
| 15 | 7.18 | 1.63 | 0.1 | 0.03 |
| 45 | 7.53 | 0.34 | 0.11 | 0.02 |
| 135 | 7.53 | 0.24 | 0.07 | 0.02 |
| 405 | **7.77** | 0.97 | 0.09 | 0.01 |

*Table 5: Average Transverse extensional modulus*

For the material model, the minor Young's Modulus used will be 140.9 GPa.

Due to the significantly lower load obtained during testing the $[90]_{10}$ specimens, there was more data obtained for the failure stress of the material as the risk to damaging the testing machine is greatly reduced.

| Loading Rate (mm/min) | Failure Stress (Mpa) | Fstress_STD (Mpa) | F_strain | F_strain_STD |
|---|---|---|---|---|
| 3 | 38.8 | 1.9 | 0.62 | 0.02 |
| 5 | 38.3 | 6.5 | 0.54 | 0.15 |
| 15 | 40.9 | 6.9 | 0.55 | 0.09 |
| 45 | 43.1 | 5.2 | 0.59 | 0.04 |
| 135 | 35.8 | 4.9 | 0.53 | 0.06 |
| 405 | 33.2 | 4.9 | 0.45 | 0.09 |

*Table 6: Average failure strength in the transverse direction*

While data has been obtained for all loading rates, to remain consistent with the longitudinal failure stress, the data from the 3 mm/min loading will be used, which gives a failure stress of $Y^T$=38.8 MPa.

## 3.2 COMPRESSIVE CHARACTERIZATION

There were no purely compressive tests performed like what were performed by Wade [36], but there were three point bending tests performed which can be used to determine the compressive failure strength. In the bending of a rectangular beam, the stress is equal in magnitude, but opposite in sign on the extreme fibers.

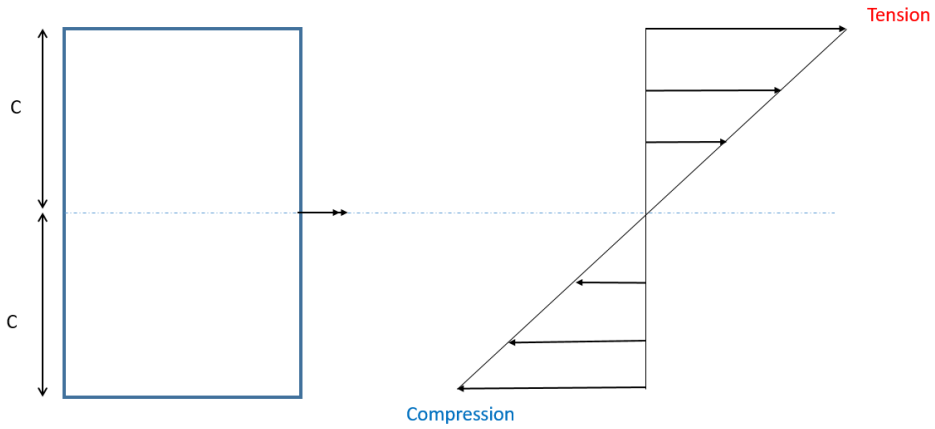


*Figure 3-5: Tensile stress distribution through the section of a rectangular beam*

To obtain the compressive failure strength from the three point bend specimens, the following assumption is made: Compressive Strength is less than the tensile strength ($X^T$>$X^C$).


*Figure 3-6: Tensile stress distribution through the section of a rectangular beam*

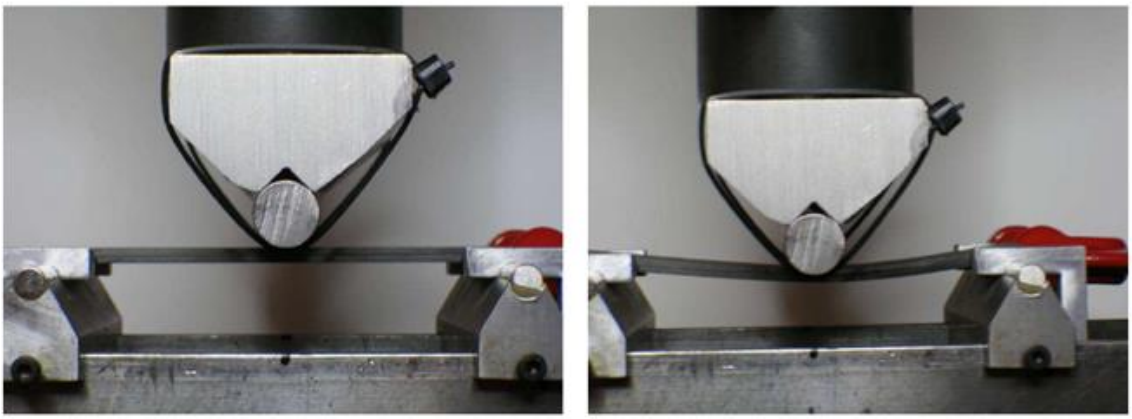

*Figure 3-7: Three point bend specimen before and during loading*

### 3.2.1 *Longitudinal Flexural Data*

The bending tests were performed at various loading rates and displayed sensitivity to the loading rates, particularly at lower load rates.

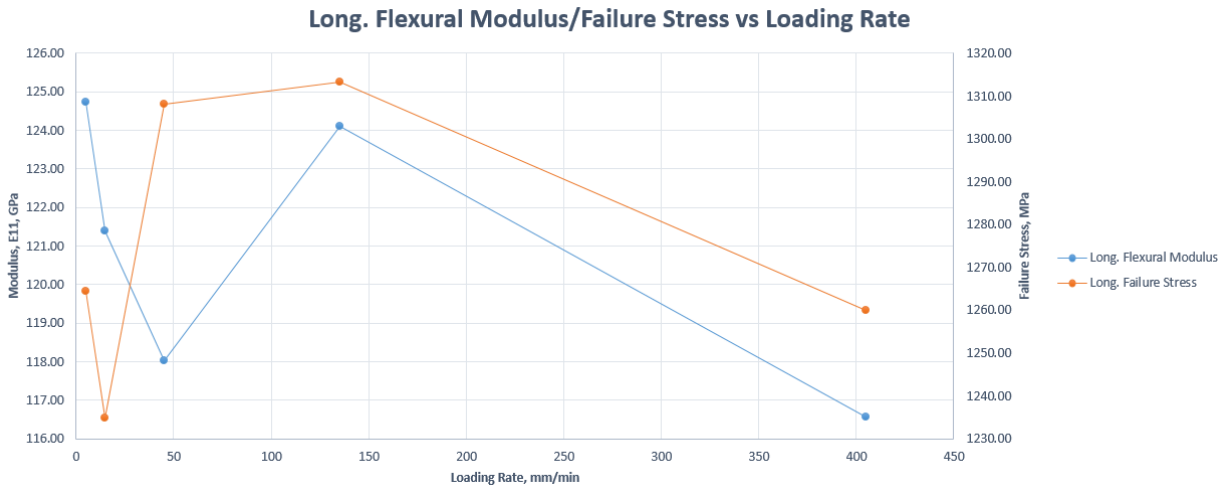


*Figure 3-8: Longitudinal extensional modulus and failure stress of material versus loading rate* [4]

From the experimental data, the average moduli and failure stress are collected for each loading rate and are presented below.

| Loading Rate (mm/min) | Avg E11 | E11_STD | Avg Fail | Fail STD |
|---|---|---|---|---|
| 3 | 124.7 | 1.72 | 1264.4 | 22.32 |
| 5 | 121.4 | 3.34 | 1234.8 | 41.89 |
| 15 | 118 | 3.83 | 1308.2 | 69.72 |
| 135 | 124.1 | 0.2 | 1313.3 | 66.93 |
| 405 | 116.6 | 13.5 | **1260.1** | 131.26 |

*Table 7: Average failure strength in the transverse direction*

The failure stress for the longitudunal direction used for the material models is 1260.1 MPa.

### 3.2.2 *Transverse Flexural Data*

The data was collected in a similar manner to the longitudinal flexural failure stress, with the exception that this time, a $[90]_{10}$ laminate was used.

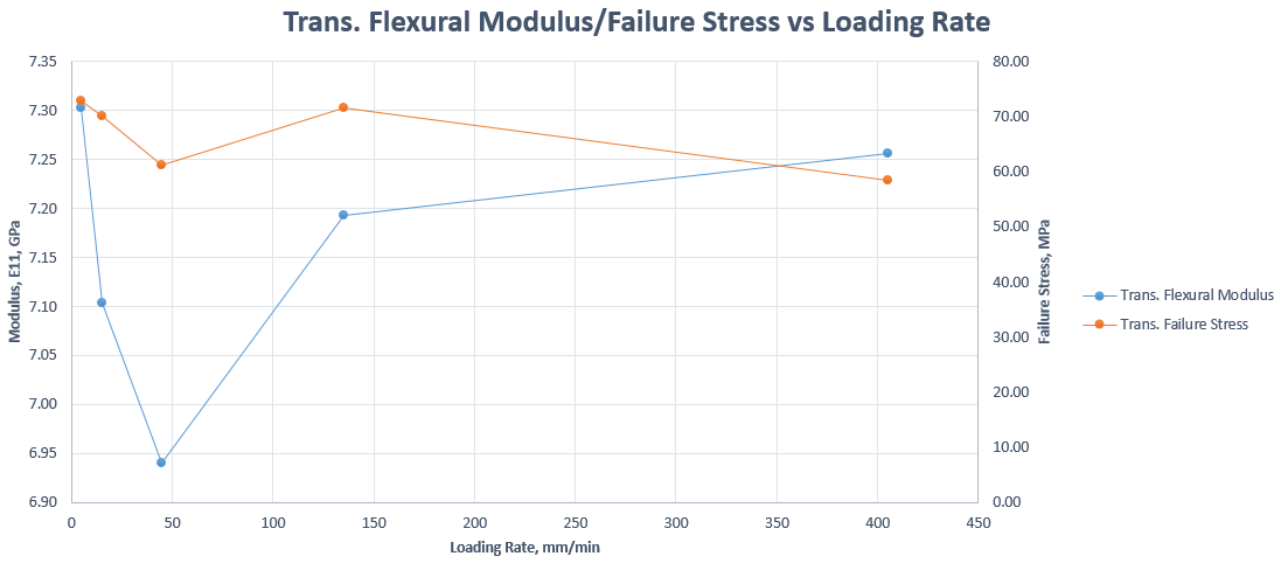


*Figure 3-9: Longitudinal extensional modulus and failure stress of material versus loading rate* [4]

From the experimental data, the average moduli and failure stress are collected for each loading rate and are presented below.

| Loading Rate (mm/min) | Avg E22 (Gpa) | Avg_E22 (Gpa) | Avg Fail (Mpa) | Fail STD (Mpa) |
|---|---|---|---|---|
| 5 | 7.30 | 0.04 | 72.90 | 10.65 |
| 15 | 7.10 | 2.36 | 70.20 | 2.36 |
| 45 | 6.94 | 4.89 | 61.30 | 4.89 |
| 135 | 7.19 | 0.38 | 71.70 | 4.35 |
| 405 | 7.26 | 0.28 | **58.37** | 1.17 |

*Table 8: Average failure strength in the transverse direction*

The failure stress for the transverse direction used for the material models is 58.37 MPa.

### 3.2.3 *Mode II Fracture Data*

Mode II fracture data was collected by performing Edge Notch Failure tests (ENF), in a similar fashion to the three point flexural tests, with the exception that coupons were manufactured with a flaw at the mid-plane. The coupons had layups of [$0_9$/5/Teflon Strip/-5/$0_9$] at the edge that acted as the starter crack and the same, sans the Teflon for the remainder of the beam; a representation of the ENF coupon is displayed in Figure 3-10.

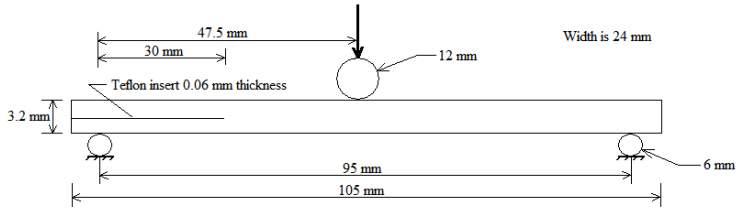


*Figure 3-10: Dimensions of the Edge Notch Failure Specimen that were used in [4]*

The measuring $G_{IIc}$ values versus loading rate are presented in Figure 3-11.

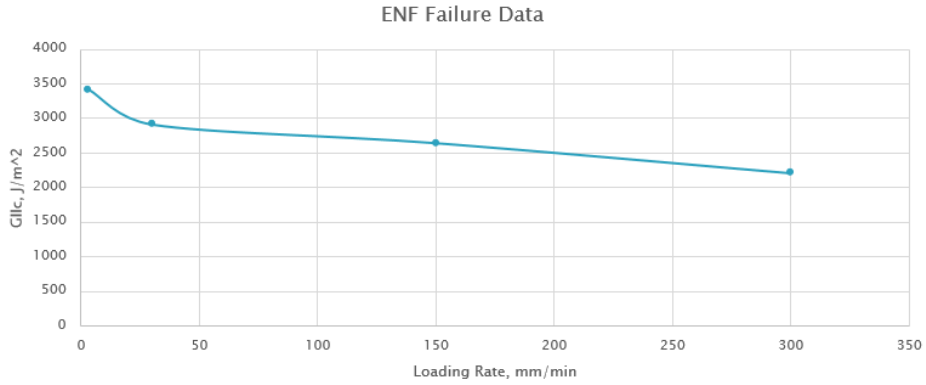


*Figure 3-11: Measured $G_{IIc}$ versus loading rate*

The average values collected for the ENF tests are presented in Figure 3-12.

| Loading Rate (mm/min) | Avg area (mm^2) | area_std (mm^2) | avg energy (mJ) | energy std (mJ) | avg Gii (J/m^2) |
|---|---|---|---|---|---|
| 3 | 202.3 | 49.9 | 678.8 | 95.3 | 3422.3 |
| 30 | 299.2 | 31.9 | 866.3 | 60.5 | 2914.9 |
| 150 | 501.8 | 247.8 | 1294.8 | 518.9 | 2647.3 |
| 300 | 395.1 | 101.9 | 864.5 | 173.9 | **2213.8** |

*Table 9: Average $G_{IIc}$*

The average $G_{IIc}$ value for the highest loading rate is 2213.8 J/m$^2$; this value will be used for the Low Velocity Impact Simulations.

# Chapter 4. MODEL CHARACTERIZATION

Abaqus uses the Hashin failure criterion for the damage initiation of laminated composites. In continuum damage mechanics the damage initiation point is the point in which the stiffness of the material begins to degrade at a material point in the element [5]. The Hashin initiation theory has four unique damage initiation terms [5, 25], which are defined in Equation 4.

## 4.1 CHARACTERIZATION OF LAMINA

### 4.1.1 *Longitudinal Tension*

Under tension, eliminating any strain rate effects, a lamina loaded in tension in the fiber dominated direction will behave linear elastically until the initiation stress is reached. When the initiation stress is reached, the energy released under failure will be equal to the strain energy accumulated at the point of damage initiation, which is indicative of brittle fracture, i.e., no degradation in stiffness to the point of failure, as displayed in Figure 4-1.

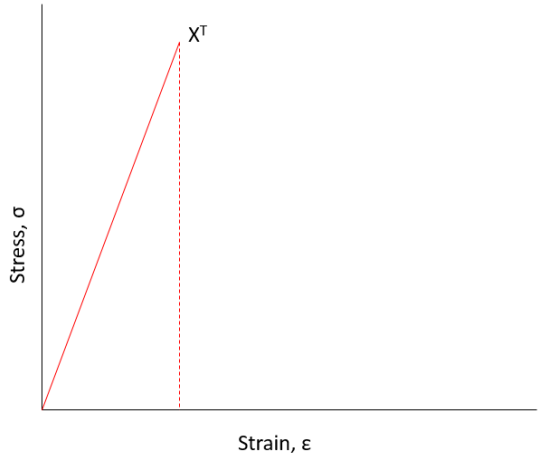


*Figure 4-1: Assumed stress strain curve of a uni-directional laminate loaded longitudinally*

From the experimental data obtained [4] the initiation stress in fiber tension is determined from the highest strain rate failure stress recorded, which is 2,154 MPa which is obtained from a coupon that was loaded at a rate of 15 mm/min.

For the continuum damage mechanics model in Abaqus, a means of softening the material is required, either in the form of energy or an equivalent displacement until the material deletes. As stated above, the assumption for the fiber direction is that the failure is brittle, meaning an instantaneous degradation in stiffness and the damage energy monitored in the model will be equivalent to the strain energy in the material until the point of failure.

The elastic strain energy is defined as:

$$SE = V\int_{\delta 0}^{\delta f}\sigma_{ij}d\varepsilon = \frac{V}{2E_{ij}}\sigma_0^2 \qquad [12]$$

Based on the modulus and failure strength determined from the test data in §3.1.2, the strain energy to failure in a lamina can be calculated:

$$SE = \frac{V}{2E_{ij}}\sigma_0^2 = \frac{(0.01m * 0.01m * 0.0000175m)}{2 * 140.9e^9 Pa} * (2007e^6)^2 Pa = 0.250J$$

The Damage energy is calculated as:

$$TE = (G_c * A) = SE + DE \qquad [13]$$

Where TE is the total energy dissipated during the loading and failure of the material and DE is the damage energy, which is zero since the material is assumed to fail in a brittle manner. Solving for $G_{fT1}$ gives:

$$G_{fT1} = \frac{SE}{A} = \frac{0.250J}{(0.01m * 0.000175m)} = 142954.25\ \frac{J}{m^2}$$

Verifying this behavior in Abaqus, a single element model is run, with dimensions of 0.01m by 0.01m and with a thickness of 0.000175m (1 ply). The material properties are entered and the model is loaded with an enforced displacement that is linear in time. A S4R, reduced integration shell element is used, meaning the element has one integration point located at its centroid [5]; a single element test for the tensile characterization of the longitudinal properties is presented in Figure 4-2. The strain energy and damage energy in the single element is displayed Figure 4-3.

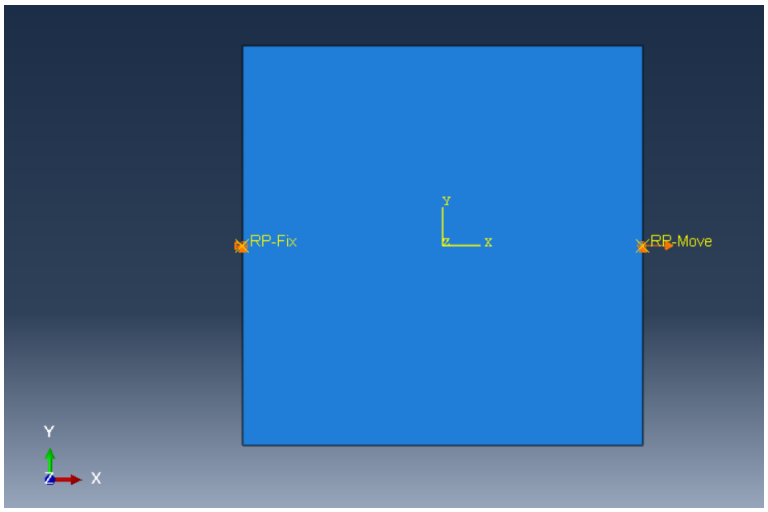


*Figure 4-2: Example of a single element test performed in Abaqus/Explicit to test material model*

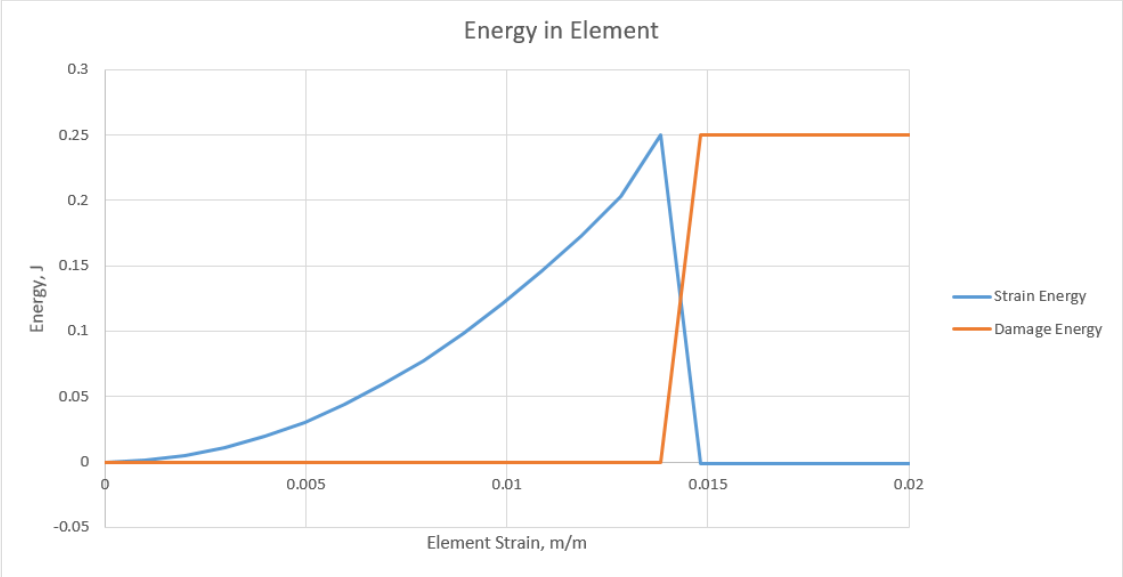


*Figure 4-3: Strain Energy and Damage Energy in a single element versus strain for longitudinal tension*

### 4.1.2 *Longitudinal Tension*

For longitudinal compression, the material will be assumed to behave in a brittle fashion in the absence of data that would lead to another conclusion. Based on what has been presented in the previous section, a single element test will be performed to verify that in compression (in the 1-2 plane) the material fails as expected (in a similar fashion to Figure 4-1). Using a longitudinal

failure stress [4] of 1,264.4 MPa and the nominal modulus of 140.9 GPa the total strain energy is calculated as:

$$SE = \frac{V}{2E_{ij}}\sigma_0^2 = \frac{(0.01m * 0.01m * 0.0000175m)}{2 * 140.9e^6 Pa} * (1264.4e^6)^2 Pa = 0.099J$$

The energy strain energy release rate, based on the calculated strain energy is:

$$G_{fT1} = \frac{SE}{A} = \frac{0.099J}{(0.01m * 0.000175m)} = 56{,}731\ \frac{J}{m^2}$$

The material model is verified using a single S4R element in Abaqus; the element energies presented in Figure 4-4.

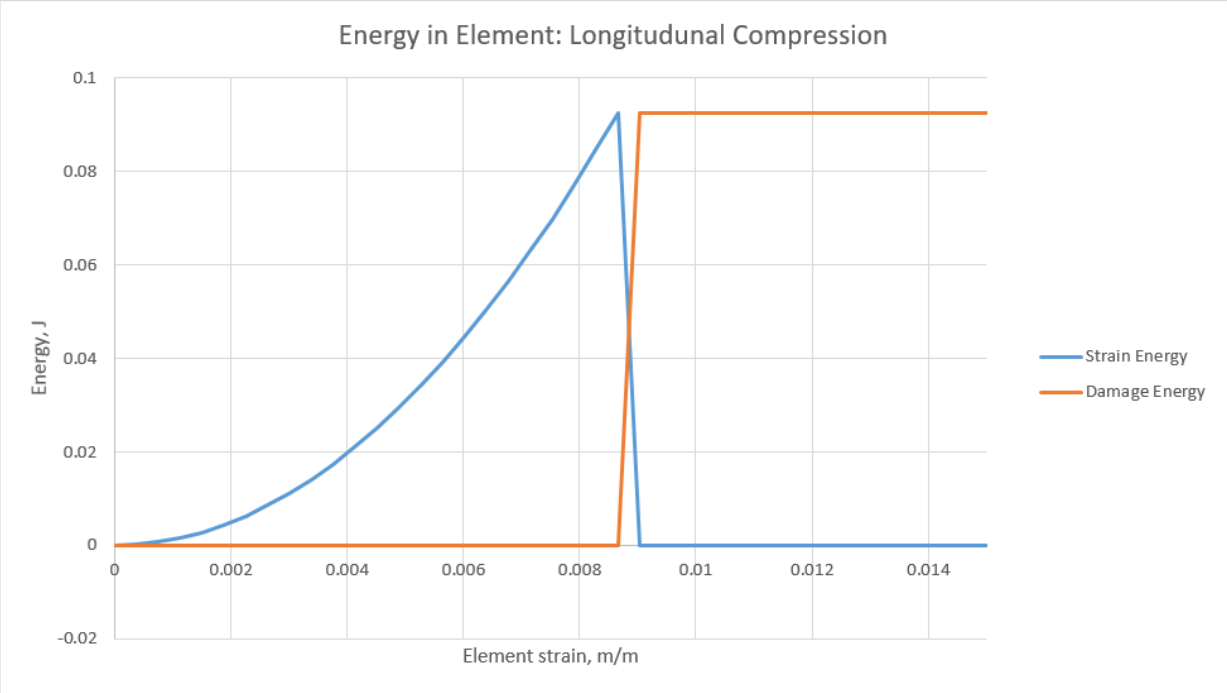


*Figure 4-4: Strain Energy and Damage Energy in a single element versus strain for longitudinal compression*

### 4.1.3 *Transverse Tension*

Unlike the longitudinal tension post damage response, the transverse direction is matrix dominated, which in theory will not behave in the same brittle fashion as the fiber dominated direction. To investigate this, the load/stroke curves for the axial characterization of the material are investigated to find evidence of this.

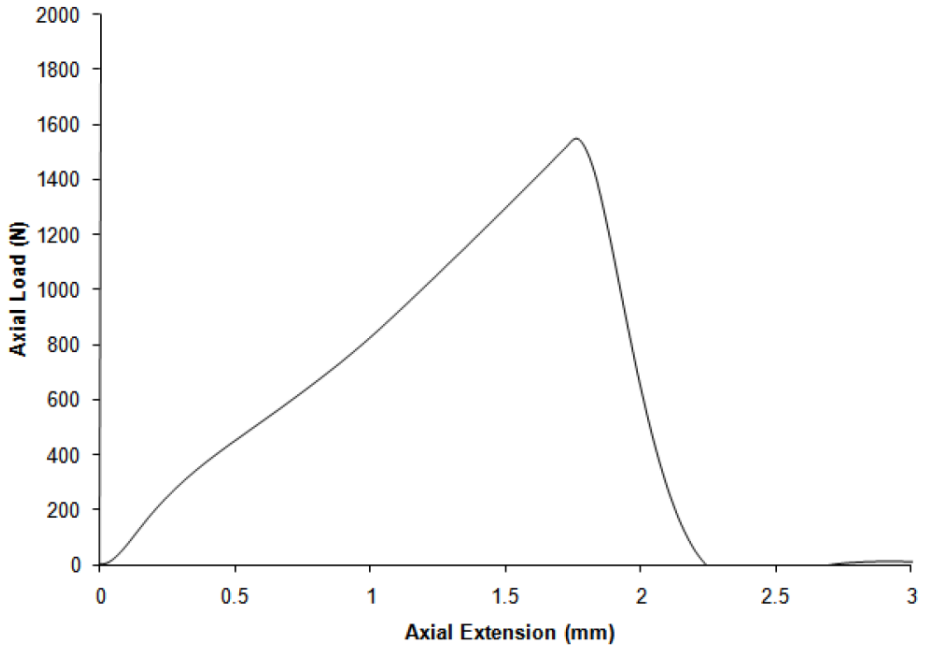


*Figure 4-5: Figure B-55 from [4] showing the load vs displacement of a uni-directional tape loaded in the transverse direction*

Figure 4-5 from [4] gives the full response of the $[90]_{10}$ coupon that was loaded to failure which displays linear decrease in the stiffness of the coupon until the load reaches zero, which works with the assumption presented at the beginning of this section. To determine the fracture energy released during the failure of the coupon the following information is needed to make this a stress strain curve.

- Extensometer gage length = 0.0255m
- $E_{22}$ = 7.77GPa
- Failure stress = 38.8MPa
- Thickness of coupon, t= 0.00175m

From the load/stroke curve the true-stress/true-strain curve is developed, and integrated from the highest stress to the point where stress becomes zero to obtain to total damage energy released during the failure of the coupon.

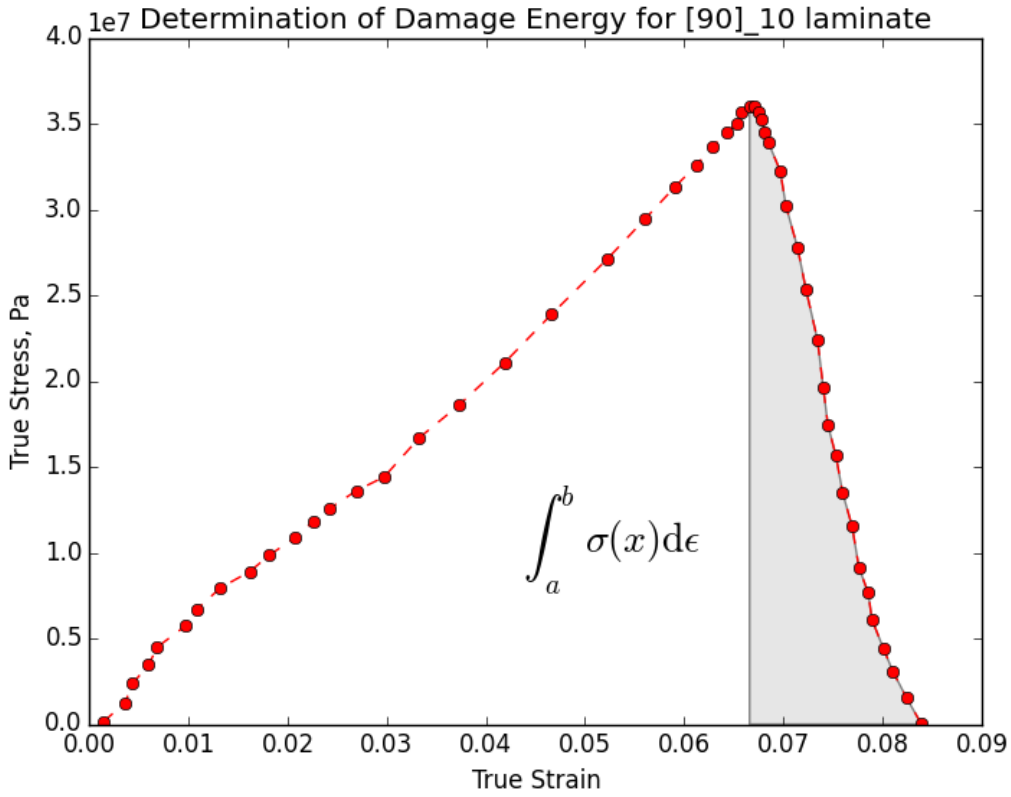


*Figure 4-6: Stress vs. Strain for the load vs. displacement curve from figure B-55 of reference [4]*

Applying equation 13 and assuming the material behaves linearly from the onset of loading until the point at which the stiffness begins to degrade, the strain energy in the coupon is:

$$SE = \frac{V}{2E_{ij}}\sigma_0^2 = \frac{(0.01m * 0.01m * 0.000175m)}{2 * 7.77e^9 Pa} * (38.8e^6)^2 Pa = 0.0017J$$

The energy released during fracture is:

$$TE = V\int_{\delta 0}^{\delta f} m\delta + \sigma_0\, d\delta = V\left[\frac{m}{2}\delta_f^2 + \sigma_0\delta_f\right] \qquad [14]$$

In all simulations, SE is always released when an element is damaged and DE is released through "ductility" of the material (implying non-brittle failure).

To determine the slope of the degradation curve in Figure 4-6, the integral from the peak stress to the point where there is zero stress is calculated numerically and is assumed to linear in nature to work with Abaqus Continuum Damage Mechanics framework. To determine this value, the relative failure displacement is determined:

$$DE = TE - SE = V\left[\frac{1}{2}\sigma_0\Delta\right] \text{ ; Where } \Delta=\delta_f - \delta_0 \text{ and } \delta_0=\sigma_0/E_{11} \quad [15]$$

The slope of the damage curve, if assumed linear, can be solved for using:

$$k = \frac{-\sigma_0}{\Delta} \quad [16]$$

Solving for k:

$$k = \frac{-1*\sigma_o}{(\varepsilon_{fail}-\varepsilon_{dam})} = \text{-5.19e}^9 \text{ Pa}$$

Using equation 16, the equivalent displacement is solved for:

$$\Delta = \frac{-\sigma_0}{k} = 0.0173m$$

Integrating the damage portion of the curve with the linear approximation, gives the damage energy released in J/m$^{2:}$

$$DE = \int_{\varepsilon_{dam}}^{\varepsilon_{fail}} \sigma_{22} d\varepsilon = \frac{1}{2}\sigma_0\Delta = \frac{1}{2} * 9e^7 Pa * 0.0173m = 13.3J$$

The total fracture energy is calculated as the total energy released per unit area:

$$G_{fT1} = \frac{SE}{A} + DE = \frac{0.017J}{(0.01m * 0.000175m)} + 13.3\frac{J}{m^2} = 982.06\ \frac{J}{m^2}$$

The material model is verified using a single S4R element in Abaqus; the element energies are presented in Figure 4-7.

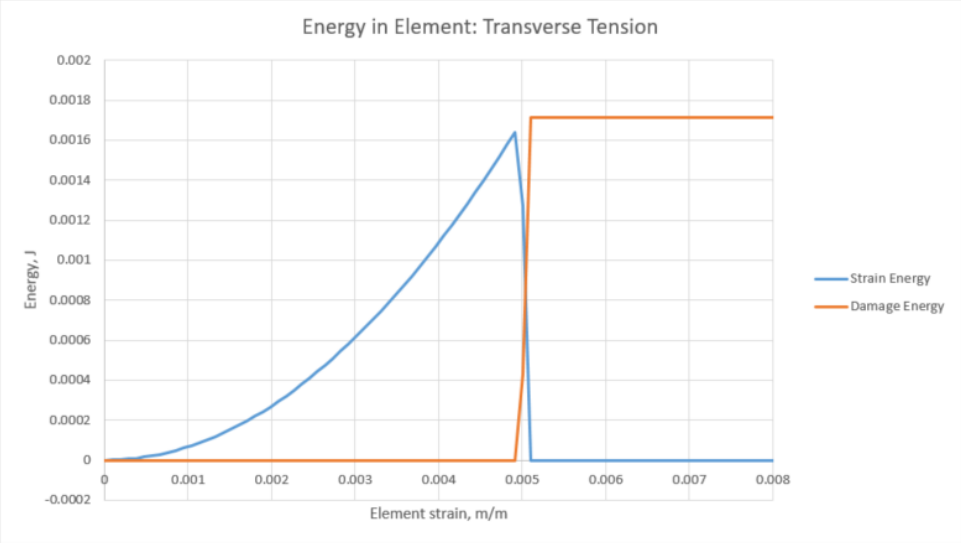


*Figure 4-7: Strain Energy and Damage Energy in a single element versus strain for transverse tension*

Figure 4-7 displays that damage energy released in the model is greater than the elastic strain energy, verifying the application of the damage energy assumptions made in this section.

### 4.1.4 *Transverse Compression*

For longitudinal compression, the material will be assumed to behave in a brittle fashion in the absence of data that would lead to another conclusion. Based on what has been presented in the previous section, a single element test will be performed to verify that in compression (in the 1-2 plane) the material fails as expected (in a similar fashion to figure 5-1). Using a longitudinal failure stress [4] of 67.5 MPa and the nominal modulus of 7.77 GPa the total strain energy is calculated as:

$$SE = \frac{V}{2E_{ij}}\sigma_0^2 = \frac{(0.01m * 0.01m * 0.0000175m)}{2 * 7.77Pa} * (7.77e^6)^2 Pa = 0.005J$$

The energy strain energy release rate, based on the calculated strain energy is:

$$G_{fT1} = \frac{SE}{A} = \frac{0.005J}{(0.01m * 0.000175m)} = 2{,}931\ \frac{J}{m^2}$$

The material model is verified using a single S4R element in Abaqus; the element energies are presented below.

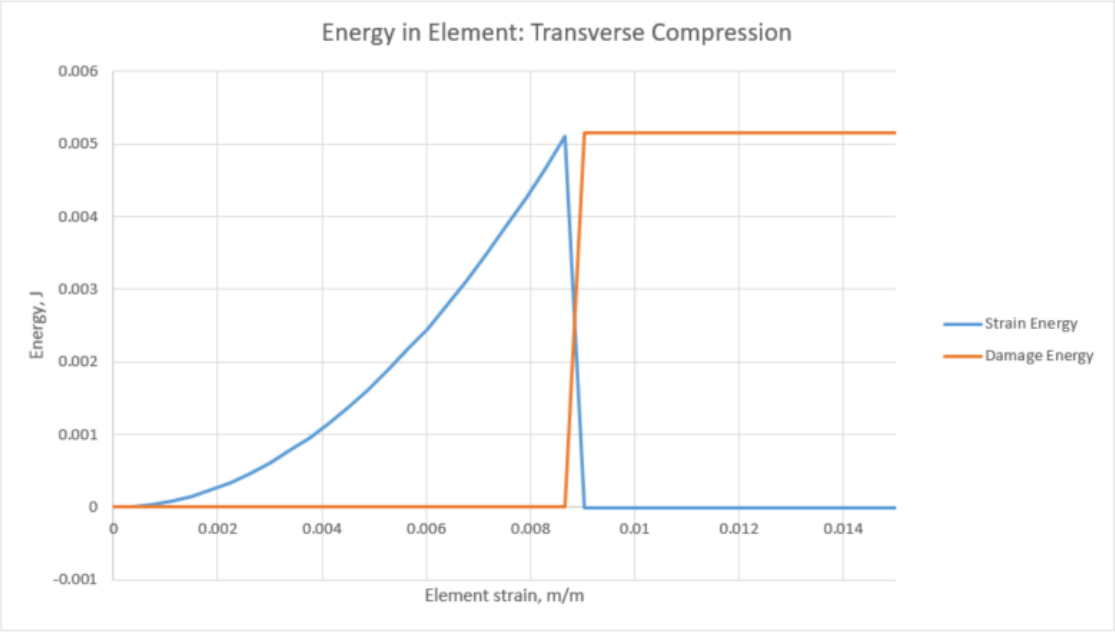


*Figure 4-8: Strain Energy and Damage Energy in a single element versus strain for transverse compression*

## 4.2 CHARACTERIZATION OF INTERLAMINAR PROPERTIES

The fracture energies are obtained during testing at various loading rates. The impact simulation will employ the use of interlaminar cohesive contact to allow for the delamination of the plate under impact; to model the cohesive interface, the cohesive stiffness terms will need to be calculated as the fracture will be based on the interlaminar stiffness. The first step for the construction of the interlaminar model is the verification of the mode II fracture energies collected; the second step is to set the cohesive stiffness to match the stiffness from a solid beam and then set the initiation stress to match the load at initiation form the test, which has been verified with the VCCT model.

The VCCT model is constructed in Abaqus CAE to match the sec described in §7 of reference [4]; the ENF failure model as constructed in Abaqus can be seen in Figure 4-10.

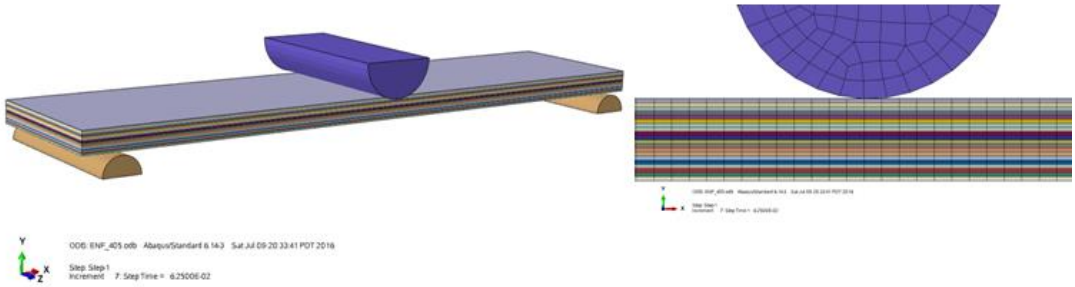

*Figure 4-9: Ply-by-ply definition of the ENF FEM using VCCT and Cohesive elements*

For the simulation, the material properties are used to define the laminate and the fracture energy presented in table 4-1 from the 405 mm/min impact rate are used rather than the fracture energies from lower strain rates to account the reduction in fracture toughness that comes from dynamic fracture.

| Loading Rate (mm/min) | Avg GII (J/m^2) | Std. Dev Crack Energy (mJ) | Avg. Onset Load (N) | Std. Dev Onset Load (N) |
|---|---|---|---|---|
| 3 | 3422.3 | 428.2 | 868.8 | 83.2 |
| 30 | 2914.9 | 301.5 | 948 | 47.3 |
| 150 | 2647.3 | 273.1 | 845 | 35.4 |
| 330 | 2213.8 | 270.8 | 880.7 | 174.2 |

*Table 10: Average mode II fracture energies*

The Edge Notch failure model is modeled with continuum shell elements using a VCCT interface between the top and bottom plies. The VCCT method, which is based on Linear Elastic Fracture Mechanics (LEFM), was developed over 35 years ago and implemented in Abaqus as an interface element in 2008 based on the work of Mabsen, Deobald and Dopker [31]. To simulate interlaminar failure, traditional cohesive elements had been implemented that relied on the cohesive zone model, where the length of the cohesive zone more mode II fracture is defined as [32]:

$$l_{cz} = ME_2 \frac{G_{IIC}}{S^2} \qquad [17]$$

Where:
M = Cohesive Zone Parameter, defined by Hillerborg as 1.0
$E_2$ = Transverse Modulus
$G_{IIC}$ = Mode II fracture energy
$S_2$ = Transverse Shear Strength

The number of elements suggested is three, which for this laminate gives a maximum element length in front of the crack 1.01mm, which makes the cohesive element model computationally expensive. If the length of the cohesive zone is considered to be much smaller than the length of initial crack, LEFM and VCCT can be applied for a much less computationally expensive analysis to be performed as the length of the cohesive zone can be omitted [26].

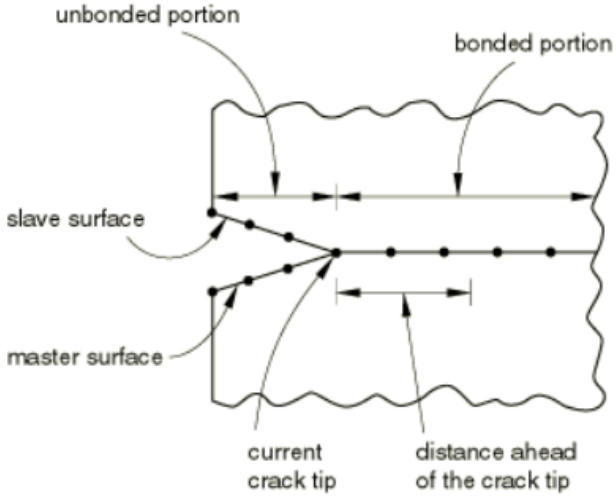


*Figure 4-10: Cross section of a crack defining VCCT terms [5]*

The means of application of VCCT in Abaqus is described in Figure 4-11, and Figure 4-12 using Mode I fracture for the demonstration of crack closing.

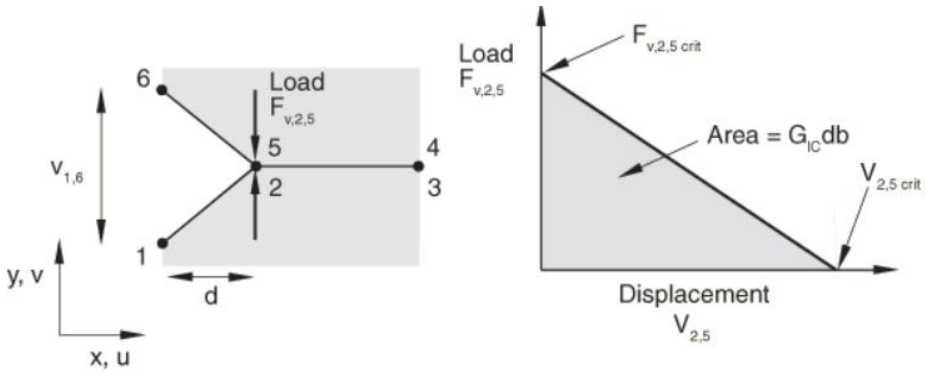


*Figure 4-11: Example of VCCT for mode I cracks [5]*

To verify the onset load from the test, the VCCT model is run until slightly after the onset delamination, which is montored with a check for a steady decrease in the reaction load from the indenter.

From the fringe plots of S11, the effects of the stress concentration at the crack front can easily be seen, at 68% simulation time and even more so at 80% simulation time, at the onset of crack growth.

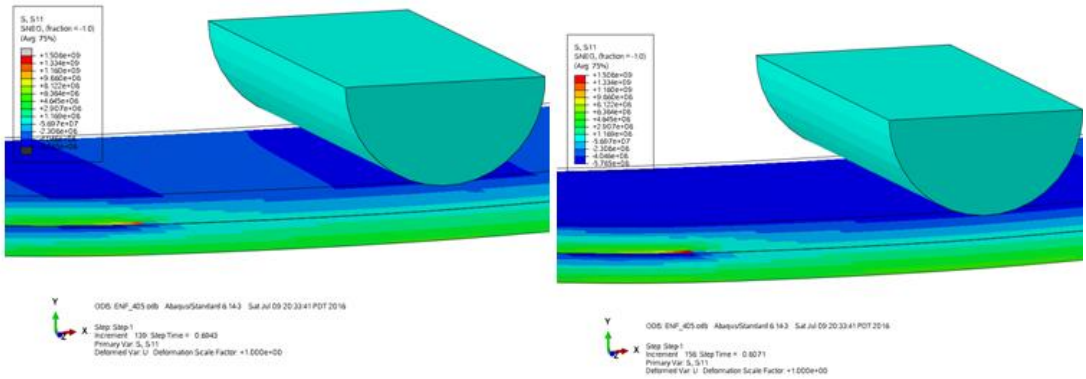

*Figure 4-12: Crack tip in ENF simulation before and after $G_{IIC}$ is exceeded*

The force-displacement curve for the simulation is presented in Figure 4-13.

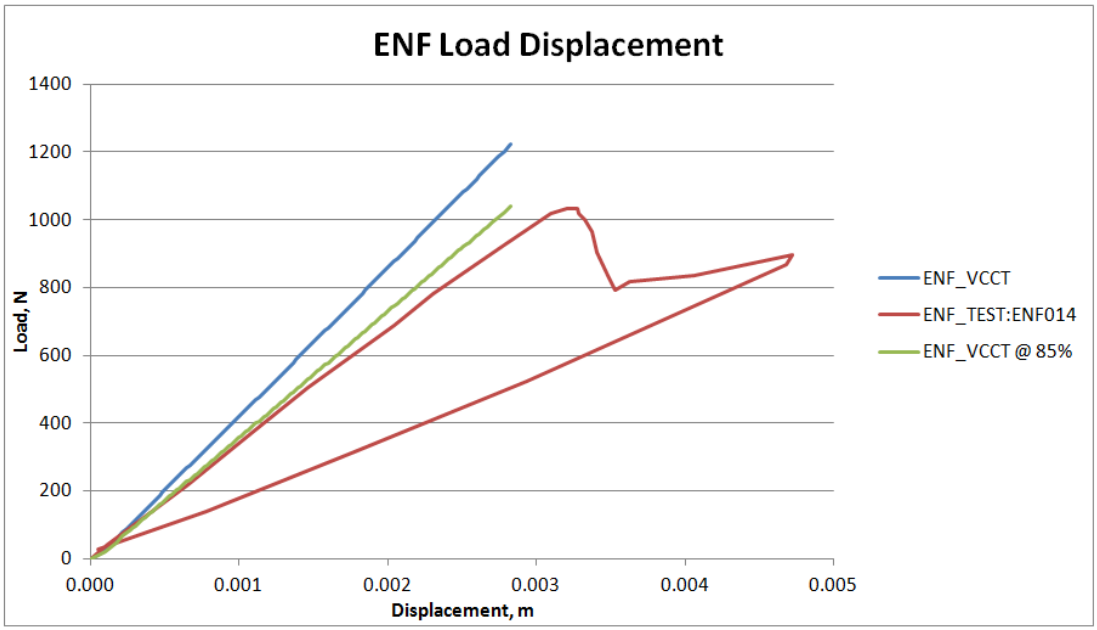


*Figure 4-13: Edge Notch Failure simulation showing differences in bending between experiment and simulation*

The Briggs [4] noted a 15% difference between CLT predictions and the experiemental results for threepoint bending tests. Given the level of confidence in the measured thickness and collected physical properties of the lamina, the explanation for the difference in bending stiffness comes the lack of an incorporation of transverse shear stiffness in CLT whereas the test clearly displays this effect. Scaling the FEM results down by noted differnce, the force-deflection looks nearly identical to the test curve up to 0.001m of deflection. To determine the transverese shear stiffness. The cohesive stiffness needed to match the stiffness of the test is determined iterively be comparing the flexural modulus desplayed in the simulation to what is observed in the experimental results.

To determine the stiffness used for the cohesive contact model, the oiterative solutiuon will adjust the stiffness terms of the cohesive elements until the flexural modulus of the simulation matched the flexural modulus of the experimental data within 2%. The algorithm of the predictive loop is displayed in Figure 4-15.

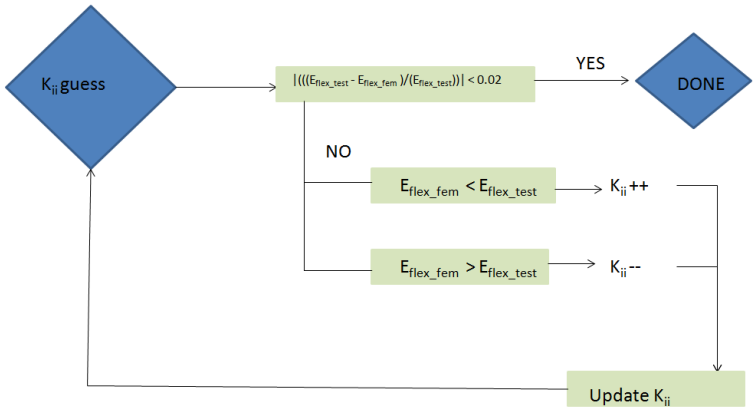


*Figure 4-14: Algorithm to determine the interlaminar stiffness terms for the cohesive contact.*

The model is set with a cohesive contact at all initially bonded plies, and a "hard" frictionless contect at the interface where the teflon ply is inserted as a crack starter. The cohesive contact will be tuned to match the transverse shear stiffnesses of the ENF failure laminate used [4]. The stiffness will be solved for using an iterative method, setting bounds at the lower and higher ends and iterating until the slope of the load deflection curve is within 2% of the load deflection curve of the ENF14 curve [4]; three of the solutions where the stiffness was solved for is presented in Figure 4-15.

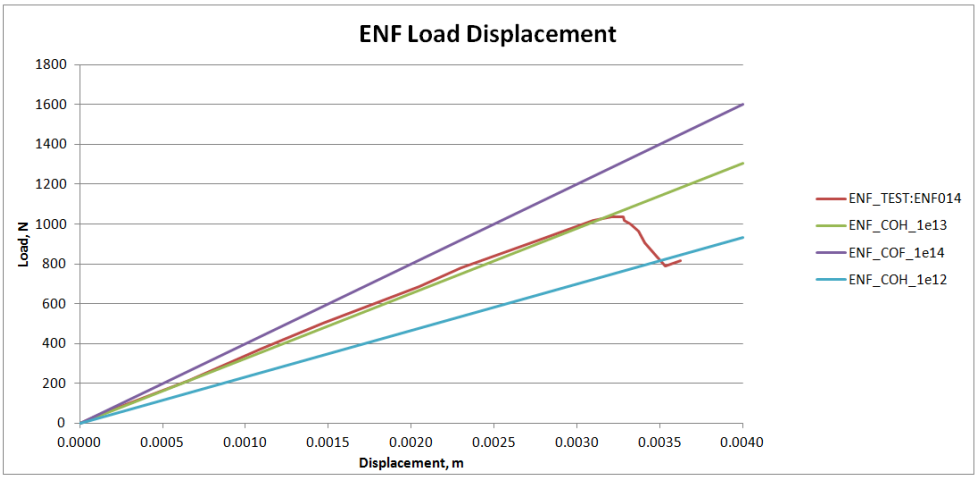


*Figure 4-15: Force Displacement curve for different $K_{ss}$ values*

Since there is no mode I fracture data, or more importantly, it doesn't not play a significant role in this simulation[18], the shear terms are focused on when evaluating the decoupled cohesive

stiffness matrix presented in §2.3. A $K_{ss}=K_{tt}$ value of $1e^{13}$ Pa matches the linear response of the ENF014 test coupon nearly perfectly. The next step for the development of the cohesive material model is set the damage initiation stress to match onset load of the ENF014 test. Following is the evaluation of initation stresses, assuming that the in-plane and anti-plane shear initition stresses are the same.

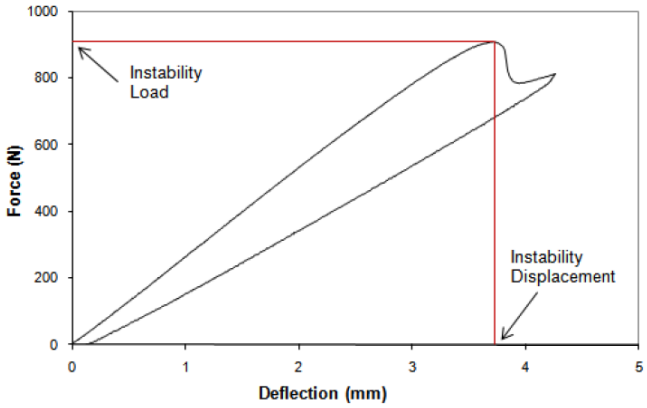


*Figure 4-16: Experimental load vs. stroke curve for ENF failure*

To match the onset of failure form the ENF014 test, the initiation stresses are determined to be: $K_{ss}=K_{tt} = 1.40e^{08}$ Pa, as displayed in 5-12.

## 4.3 MATERIAL PROPERTIES

### 4.3.1 *Lamina Properties*

| Material Props | Variable | Units | Value |
|---|---|---|---|
| Longitudinal Modulus | E11 | GPa | 140.9 |
| Transverse Modulus | E22=E33 | GPa | 7.77 |
| Poisson Ratio | v | | 0.3 |
| Shear Moduli | G12=G23=G31 | GPa | 2.42 |
| | | | |
| Longitudinal Tensile Strength | XT | Mpa | 2007.1 |
| Longitudinal Compressive Strength | XC | Mpa | 1264.4 |
| Transverse Tensile Strength | YT | Mpa | 38.8 |
| Transverse Compressive Strength | YC | Mpa | 67.5 |
| In-Plane Shear Strength | S | Mpa | 75.05 |
| | | | |
| Tensile Fracture along Fibre dir. 1 | Gf1T | J/m^2 | 142954.24 |
| Comp. Fracture along Fibre dir. 1 | GF1C | J/m^2 | 56731.99 |
| Tensile Fracture along Fibre dir. 2 | GF2T | J/m^2 | 982.06 |
| Comp. Fracture along Fibre dir. 2 | GF2- | J/m^2 | 2931.95 |

*Table 11: Final Material Properties for the material models*

### 4.3.2 *Interlaminar Properties*

| Material Properties | Variable | Units | Value |
|---|---|---|---|
| Mode II critical fracture energy | GIIc | J/m^2 | 2213.8 |
| Normal Cohesive Stiffness | Knn | Pa | 1.00E+13 |
| First Tangential Cohesive Stiffness | Kss | Pa | 1.00E+13 |
| Second Tangential Cohesive Stiffness | Ktt | Pa | 1.00E+13 |
| Normal Initiation Stress | tn | Pa | 1.00E+30 |
| First Tangential Initiation Stress | ts | Pa | 1.40E+08 |
| Second Tangential Initiation Stress | tt | Pa | 1.40E+08 |

*Table 12: Final Cohesive Properties*

The normal damage initiation stress is set to a value approaching infinity as the there is no test data for Mode I fracture and the assessment by Razi [18] that Mode II dominates in an impact event. Therefore the model is only allowed to delaminate in the shear based modes, as the normal initiation stress is unreachable.

## 4.4 FEM DEFINITION

### 4.4.1 *Overview*

For the simulation of the impact event, two types of coupons will be used: reduced coupons with idealized boundary conditions that operate on assumptions that idealize the test fixture and a full model of the test fixture which will provide more accurate boundary conditions, particularly at the edges of the coupon that are assumed to be clamped, as well as being significantly more refined than the reduced coupons.

### 4.4.2 *Modeling of Laminate*

To be able to accurately capture the damage dissipation during the impact of the laminate as well as capture the first delamination, the laminate needs to be modeled using a “ply-by-ply” method with properties between each lamina that represents the interlaminar interface. While a shell

element model may be able to predict the response up to the point of damage initiation, a more detailed model is required to fully evaluate the post damaged response of the coupon. The failure of the composite has several features that cannot be accounted for with a single shell element model:

- Through Thickness stresses (matrix crushing)
- Interlaminar interface (stiffness and delamination prediction)
- Post face ply failure contacts

For the Hashin material model in Abaqus a plane stress element is required, meaning solid elements are not currently supported using this damage model. To get the required 3D discretization to model the interlaminar interfaces as well as providing the through thickness stress distribution needed for a continuum damage mechanics model, the Abaqus continuum shell model will be employed.

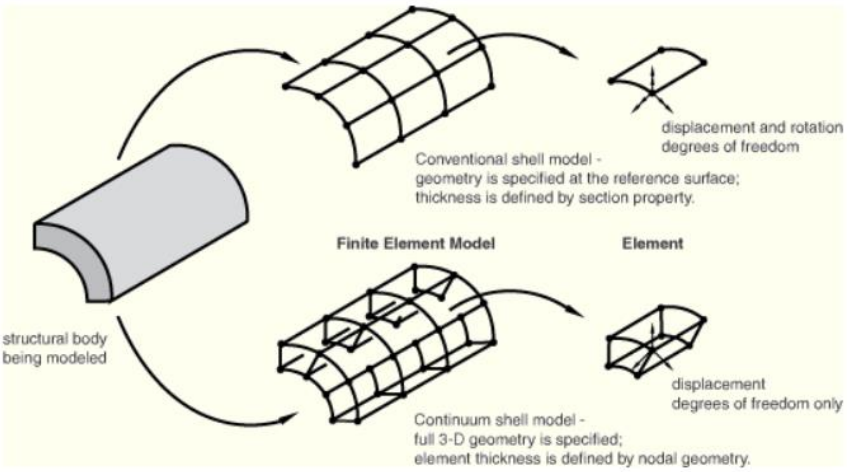


*Figure 4-17: Graphical definition of a continuum (or thick) shell* [5]

The continuum shell element is topologically a solid element and like a solid element only have translational degrees of freedom at the nodes [5]. The continuum shell elements are suitable for geometric nonlinear analysis as the element allows for finite membrane deformations as well as large rotations. The elements are able to include the effect of transverse shear deformation and when stacked, similar to what is being done in this analysis, allow for a more accurate transverse shear deformation prediction. The Abaqus graphical definition of a Continuum Shell element is presented in Figure 4-17.

To evaluate the difference in different element formulations a three point bending test was simulated to path the $[0]_{10}$ specimens used to develop the compressive failure stresses presented in §3. From the testing performed, the flexural modulus was measured for several strain rates [4] using a three-point bend test.

To test the mesh sensitivity, as well as element formulation sensitivity of the flexural rigidity of the virtual coupon, a FEM was built in Abaqus/Standard and was loaded with an enforced boundary condition, and the load/displacement response was used to calculate the flexural modulus for the mesh configuration. The coupons were tested with various element formulations (shell and continuum shell) with global mesh densities ranging from 1mm to 7mm. The reaction forces from the simple supports were extracted, and the flexural modulus for the simulation was calculated as follows [4]:

$$E_{flex} = \frac{L^3}{4wt^3}\left(\frac{P}{v}\right) \qquad [18]$$

From [4], the coupon sample the flexural coupon is displayed in Figure 4-18, with continuum shell and conventional shell representations in Figure 4-19.

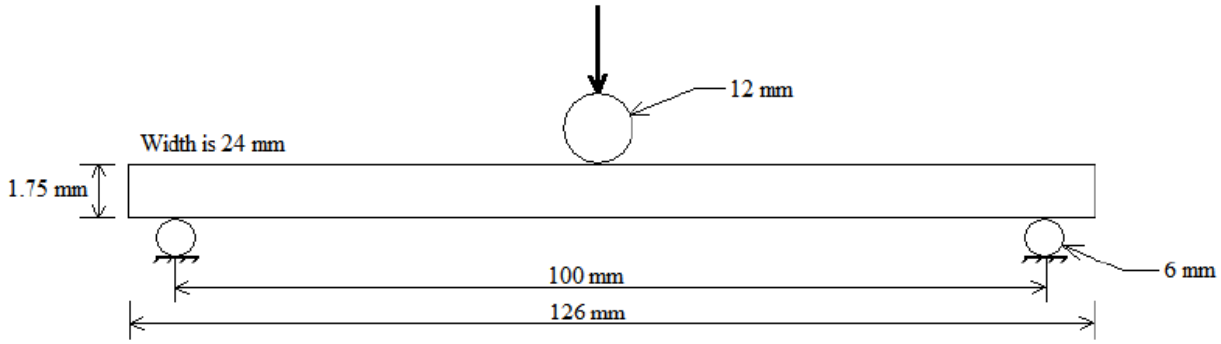


*Figure 4-18: Three Point Bend coupon dimensions*

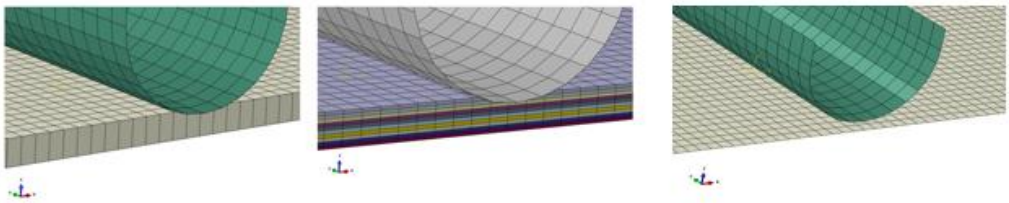

*Figure 4-19: TPB specimens with continuum shell elements, with 1 layer and 10 layers, respectively, as well as shell version*

The calculated flexural modulus from the FEM is compared to the Flexural Modulus from the test and the analytical Flexural Modulus, both using data from tests performed at 405 mm/min.

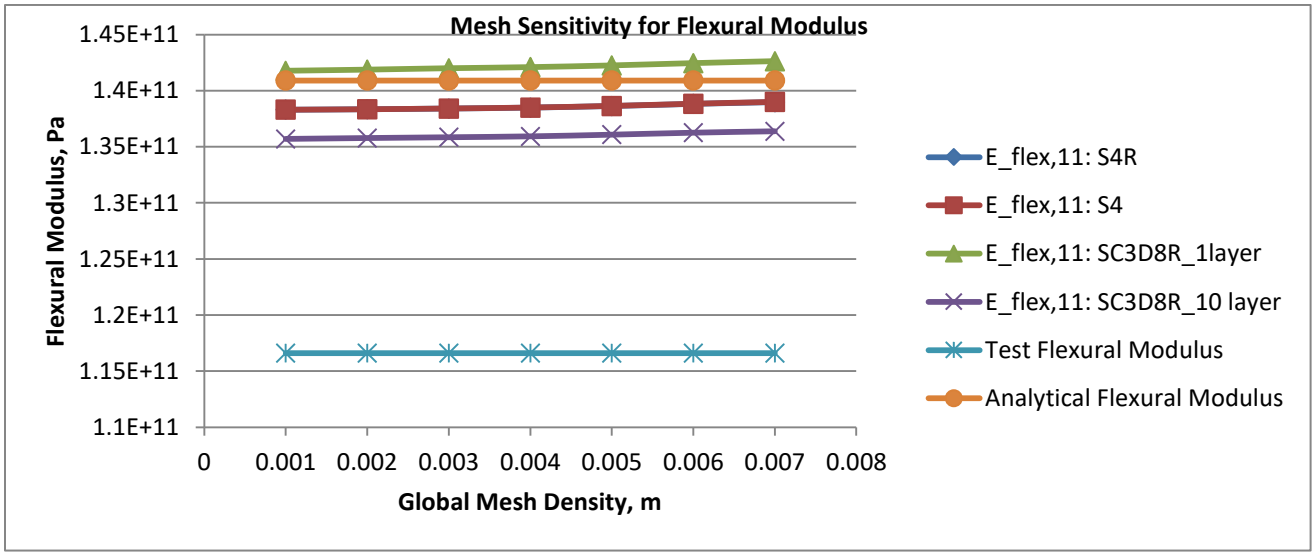


*Figure 4-20: Flexural Modulus from FEM, Test and Analytical determination*

The flexural modulus from collected from the tests is significantly than the CLT and/or FEM results, as noted by the author of reference [4] (Figure 4-20). As the results from the moduli collected in the axial coupon data are well established, as is the thickness of the lamina and laminates (i.e., a consistent thickness across all coupon thicknesses), the evidence indicates that the difference in results between CLT and test is due to the lack of transverse stiffness considerations in CLT and subsequently the FEA predictions. The 15% difference noted by the author is presented in the following figure (Figure 4-21).

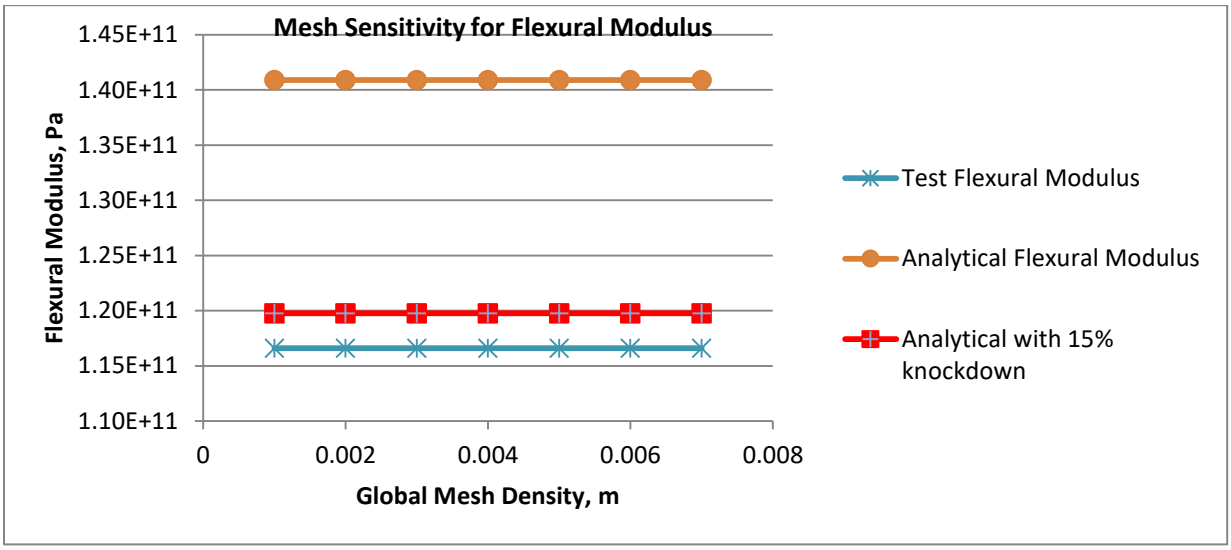


*Figure 4-21: Flexural Moduli for the test specimens, experimentally and analytically*

Based on the test data, the average difference between the analytical result and the experimental result is -20.8%. The difference in transverse shear stiffness needs to be considered in the subsequent analysis, further enforcing the need to accurately tune the transverse shear stiffness. While the single layer continuum shell element matches the analytical solution more closely; the 10 layer model matches the solution better than the shell elements, which display a much lower stiffness than the continuum shells in bending. This further emphasizes the need of a single layer of elements per ply to match the stiffness in bending more accurately [14]. The ability to have a more accurate transverse shear prediction is imperative for the determination of mode II delamination and the interlaminar shear stress is driven the accuracy of the transverse shear.

While the solid elements would theoretically be ideal for this application the lack of a damage model for solid elements forces the application of continuum shell elements [5]. The Hashin material model is a plane stress assumption, meaning that the stresses evaluated for the damage of the mode are:

$$\begin{bmatrix}\sigma_1\\ \sigma_2\\ \tau_{12}\end{bmatrix} = \begin{bmatrix}Q_{11} & Q_{12} & 0\\ Q_{12} & Q_{66} & 0\\ 0 & 0 & Q_{66}\end{bmatrix}\begin{bmatrix}\varepsilon_{11}\\ \varepsilon_{22}\\ \gamma_{12}\end{bmatrix} \qquad [19]$$

Where:

$$Q_{11} = \frac{E_{11}}{1-v_{12}^2} \qquad Q_{22} = \frac{E_{22}}{1-v_{12}^2} \qquad Q_{12} = \frac{E_{22}*v_{12}}{1-v_{12}^2} \qquad Q_{66} = G_{12}$$

For all impact coupons each lamina is modeled as a single layer of continuum shell elements with a *COHESIVE CONTACT interface specified between each layer. The cohesive contact is needed to model the delamination that occur during the impact event, as a traction separation law is employed to model the growth of the delamination and stress based initiation criterion is used to begin the crack. An example of the what *CONTACT is setup for the models is displayed in Figure 4-22.

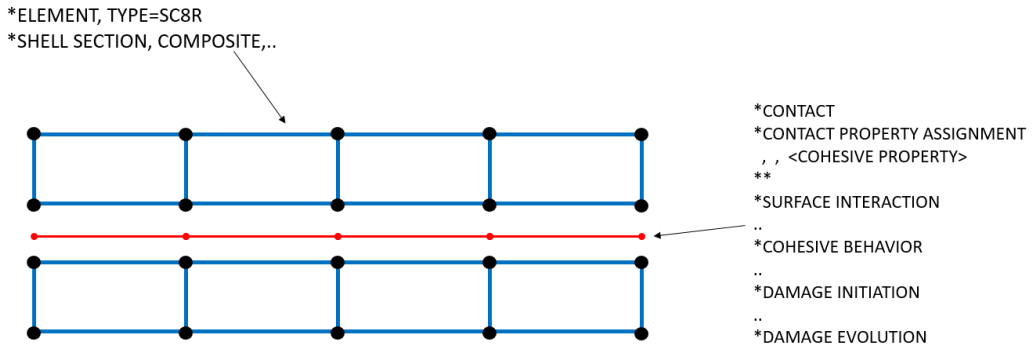


*Figure 4-22: Abaqus definition of lamina/inter laminar interface/lamina*

With the cohesive behavior, the stress based damage initiation is a function of the stiffness of the cohesive interaction. The traction stress tensor is defined as:

$$t = \begin{Bmatrix} t_n \\ t_s \\ t_t \end{Bmatrix} = \begin{bmatrix} K_{nn} & K_{ns} & K_{nt} \\ K_{ns} & K_{ss} & K_{st} \\ K_{nt} & K_{st} & K_{tt} \end{bmatrix} \begin{Bmatrix} \delta_n \\ \delta_s \\ \delta_t \end{Bmatrix} \qquad [20]$$

Where:
$t_{n,s,t}$=normal and shear tractions
$K_{ij}$ = Stiffness for cohesive interaction
$\delta_j$= separation between coincident nodes that are joined via cohesive contact

### 4.4.3 *Loads and Boundary Conditions*

#### 4.4.3.1 Reduced Model

The reduced model consists of a laminate and a rigid Tupper. The Tupper has a *ELEMENT, TYPE=MASS as well as one for inertia, but the inertia element can omitted if there is no friction between the Tupper and laminate during impact, as there will be no forces except normal in the contact pair. In the case of this simulation, friction is present as frictional energy dissipation needs to be considered for the energy balance of the system which required the use of a *ELEMENT, TYPE=ROTARY; isotropic inertia is added to counter any frictional forces on the Tupper to coupon interface that may result in our of balance forces that cause a rotation of the Tupper about its centerline. The reduced model models are run with one continuum shell element layer for each ply; with three integration points through the thickness of the ply (the same applies for the full model). For an example, please see Figure 4-23.

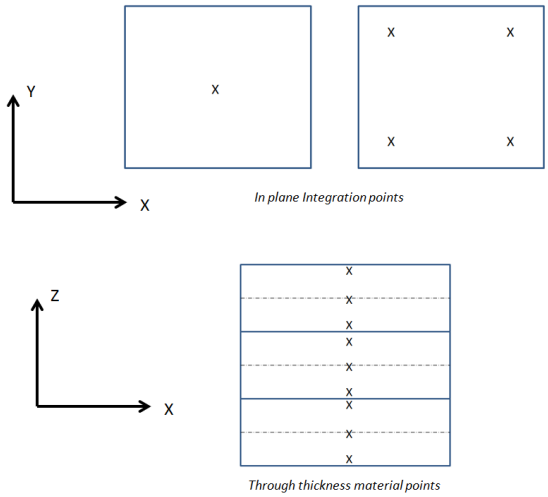


*Figure 4-23: Definition of integration points and material points through thickness in four node shell elements*

The plates were meshed in using the four corners approach in Abaqus/CAE; Abaqus supports both the four corner approach, as well as the centre triangle method with limited partitioning. While the five block approach can be meshed in Abaqus/CAE, it requires more partitioning, whereas it is the standard type of mesh produced by meshing tools like True Grid and LS-Pre/Post (Figure 4-24).

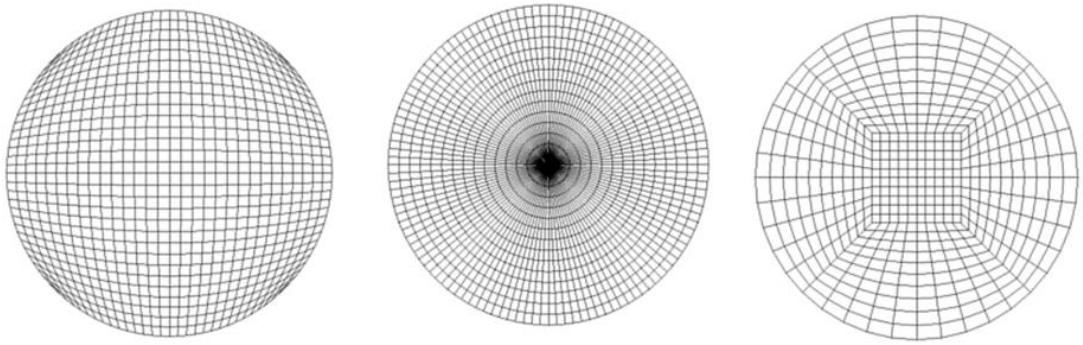

*Figure 4-24: Four Corners, Centre Triangle, 5-Block meshing algorithms for circles; True Grid, XYZ Corp.*

To mimic the boundary conditions from the B450R testing fixture, the plate was partitioned with a circle, equal to the diameter of the hole in the upper fixture of 38.1mm. All nodes within this partition are not constrained and are allowed to move. Elements outside of this partition have some form of boundary condition. The two boundary conditions are described below and are graphically displayed in Figure 4-25.

- Intermediate region: The plate is constrained in the Z-direction only, acting a rigid boundary condition preventing out of plane displacement, much like the B450R. For this assumption to work, it is assumed that the friction between the part and fixture (i.e., there is no tangential traction acting on the surface of the coupon.

- Exterior region: All surface nodes are constrained in all three translational degrees of freedom. These boundary conditions take all tangential or frictional forces, allowing for a more relaxed condition at the edge of the upper clamping plate to the upper fixture and preventing spurious damage at the edge of the coupon.

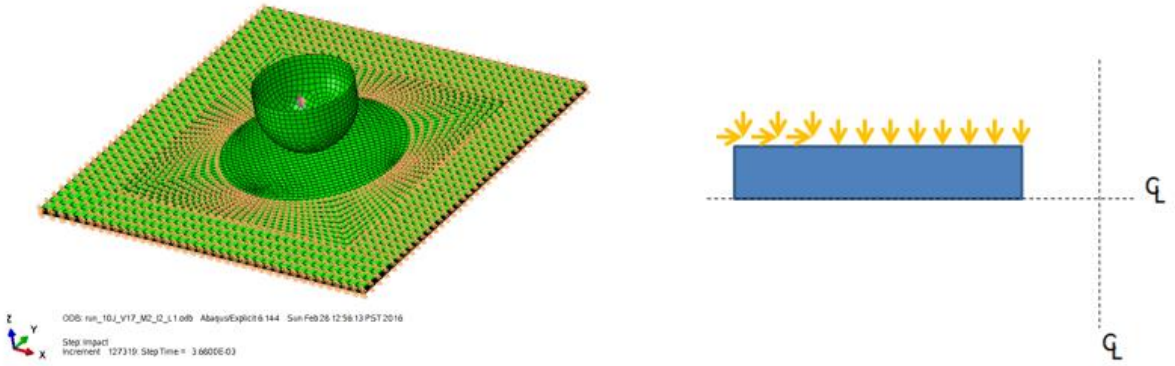

*Figure 4-25: Boundary conditions on reduced coupon in Abaqus/CAE as well a quarter symmetry definition of the boundary conditions*

#### 4.4.3.2 Full Fixture Simulation

To gain a more complete understanding of the behavior of the impact coupons, the B450R impact fixture was modeled in detail to provide the most accurate boundary conditions possible. The B450R clamping fixture is made from milled Aluminum and the top is fastened to the bottom with six steel bolts. The B450R test fixture is displayed in Figure 4-26.

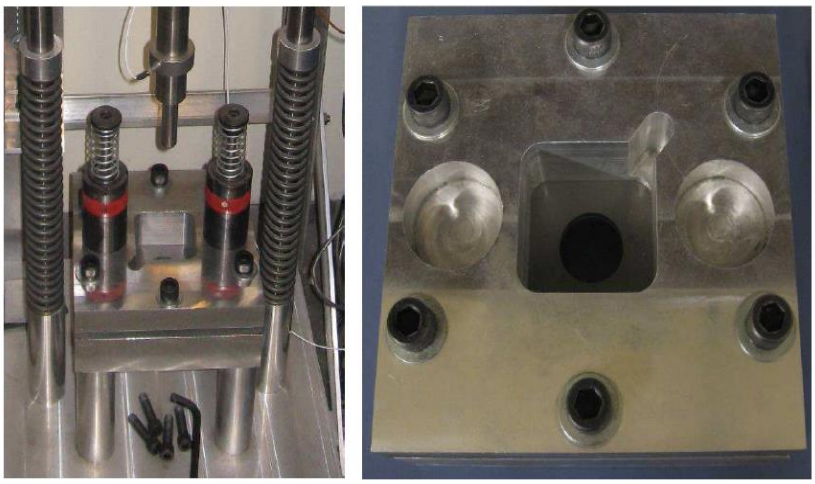

*Figure 4-26:* B450R test fixture [4]

The FEM representation of the clamping fixture was generated in CATIA V5 and meshed in Abaqus/CAE. The entire fixture is modeled using 3D solid elements; the mesh is displayed in Figure 4-27, and the element totals in Table

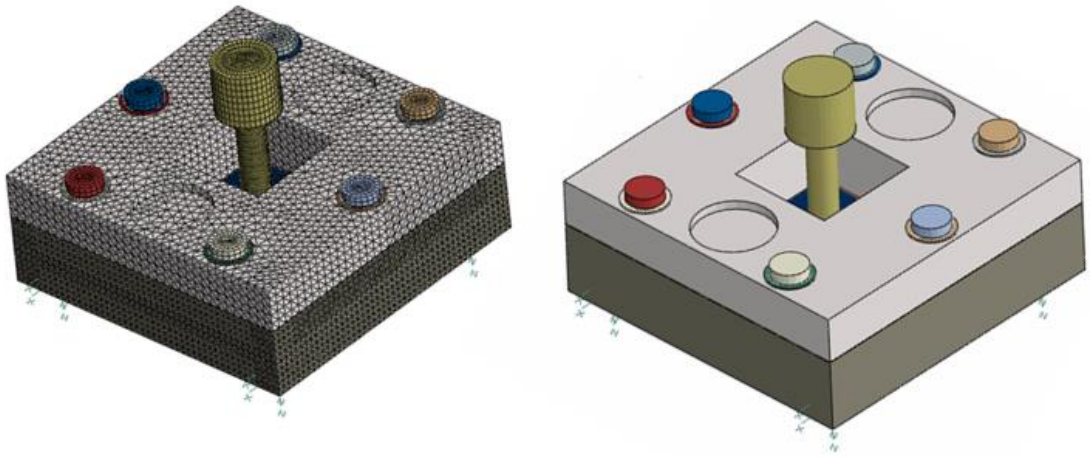

*Figure 4-27: Full fixture definition in Abaqus CAE*

| Part | Num Elements | Element Type |
|---|---|---|
| Tupper | 4,842 | C3D8R, C3D6R |
| Washers | 1,320 | C3D8R |
| Bolts | 6,720 | C3D8R, C3D6R |
| Upper Fixture | 42,446 | C3D10M |
| Lower Fixture | 130,771 | C3D10M |
| Top Plate | 1,053 | C3D8R |
| Bottom Plate | 1,053 | C3D8R |
| Elements per Ply | 4,823 | SC8R, SC6R |

| | | |
|---|---|---|
| **Total Elements** | 8 Ply | 226,789 |
| | 12 Ply | 246,081 |

*Table 13: Element distribution in full fixture FEM*

The upper and lower pieces of the fixture are meshed with C3D10M elements which are reduced integration 10 node tetrahedral elements with hourglass control and an improved formulation for contact pressure distribution. In modern analysis, due to increases in the computing power, the use of tetrahedral elements has become common place as the 10-noded elements give results

nearly equivalent to 4 node brick elements, but with an increase in cost for the time of simulation.

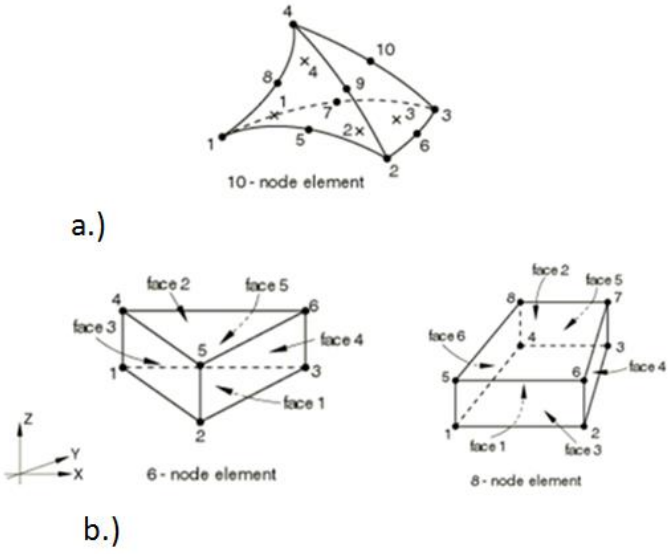


*Figure 4-28: a.) Nodal and integration point layout in Abaqus C3D10M element, b.) Nodal definitions of SC3D6 and SC3D8 elements in Abaqus* [5]

The bolts, washers, coupon restraining plates and Tupper are meshed with reduced integration solid six and eight node elements with hourglass control. These elements are computationally inexpensive compared to the C3D10M, but require heavily partitioned geometry to be able to create the meshes. Examples of the elements used in the full analysis are presented in Figure 4-28.

# Chapter 5. RESULTS AND DISCUSSION

The simulations to replicate the experiments performed by Briggs [4] for both the reduced coupon and the full fixture overall represent the general response of the coupons from the initial response to the point of delamination. For energy levels of 10J, particularly for cross-ply laminates, the Force vs. Displacement curves for the FEM match the curves from experimental data fairly well. The major differences become evident near the peak stroke of the Tupper: the test curves tend to have a more rounded response and the return portion of the curve never makes it back to zero. Generally, the reduced coupons as well as the full fixture do not predict the post damaged response of the material, but accurately predict the onset of damage accurately. The prediction of the onset of damage, or "first material damage" is employed based on the work of Belingardi [35] that identified the "first material damage" as the first major disturbance in the Force-Displacement curve; an example of Belingardi's work is the left-most Force-Displacement curve in Figure 2-9, which clearly displays a severe oscillation at the onset of damage.

## 5.1 REDUCED COUPON

For the reduced coupon models the Force vs. Displacement, Velocity vs. Displacement curves are presented, as is the ability for the reduced model to predict the damage the onset of damage in the coupon. The predicted state of damage is also presented.

### 5.1.1 *Results for $[(0/90)_2]_s$ laminate at 10J*

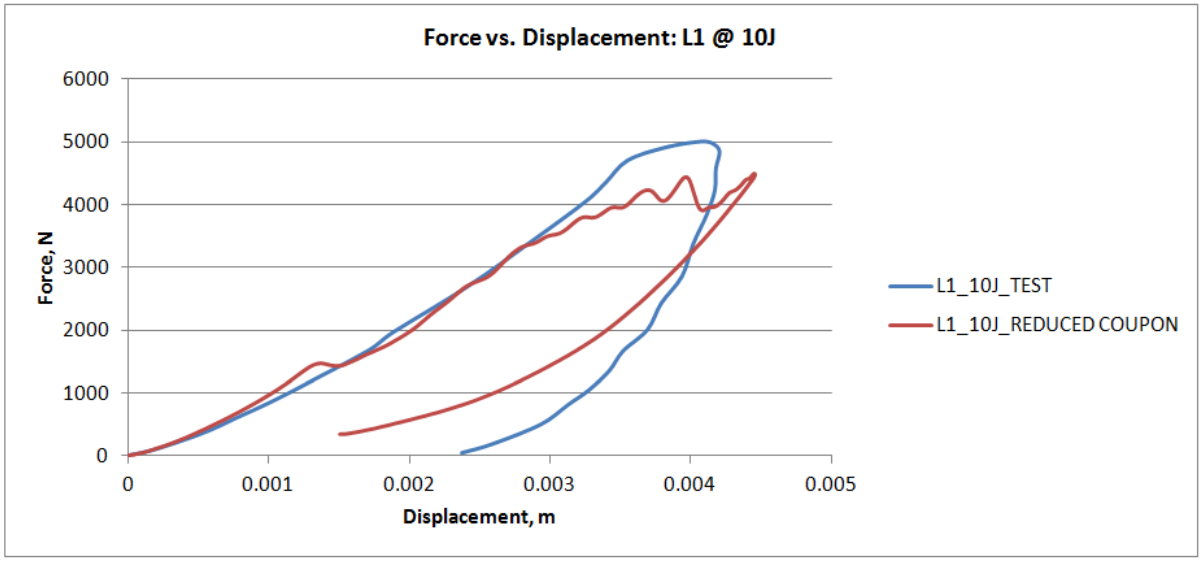


*Figure 5-1: Force-Displacement curve for $[(0/90)_2]$s 10J impact*

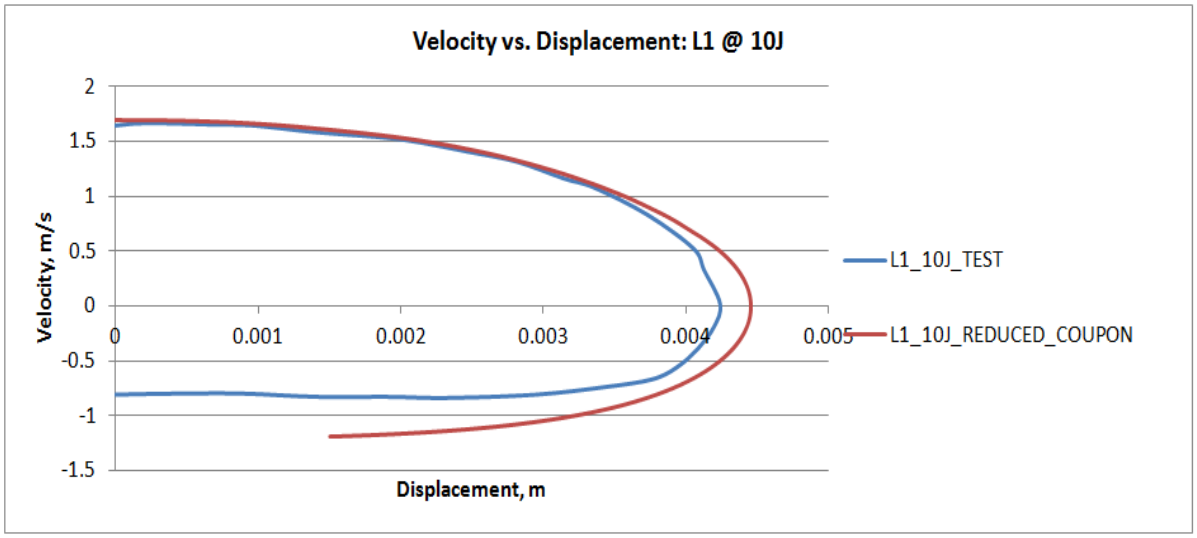


*Figure 5-2: -Displacement curve for $[(0/90)_2]$s 10J impact*

The Force-Displacement curve for this condition displays correlation well past the onset of damage, to nearly 3mm of displacement (Figure 5-1). The simulation also reveals limited damage in the coupon; at the center of the coupon the delamination state variable only reaches 1.0 at a few nodes and the delamination does not propagate. The primary damage in the coupon

is localized matrix damage, monitored using the DMGSHR state variable (Shear based damage in the lamina) as well as the Hashin Failure criterion variables.

The primary damage in the coupon is matrix damage per the Hashin Criterion, with the face plies experiencing significant matrix damage in tension and compression but very limited fiber damage, localized to the area where peak contact stresses are experienced.

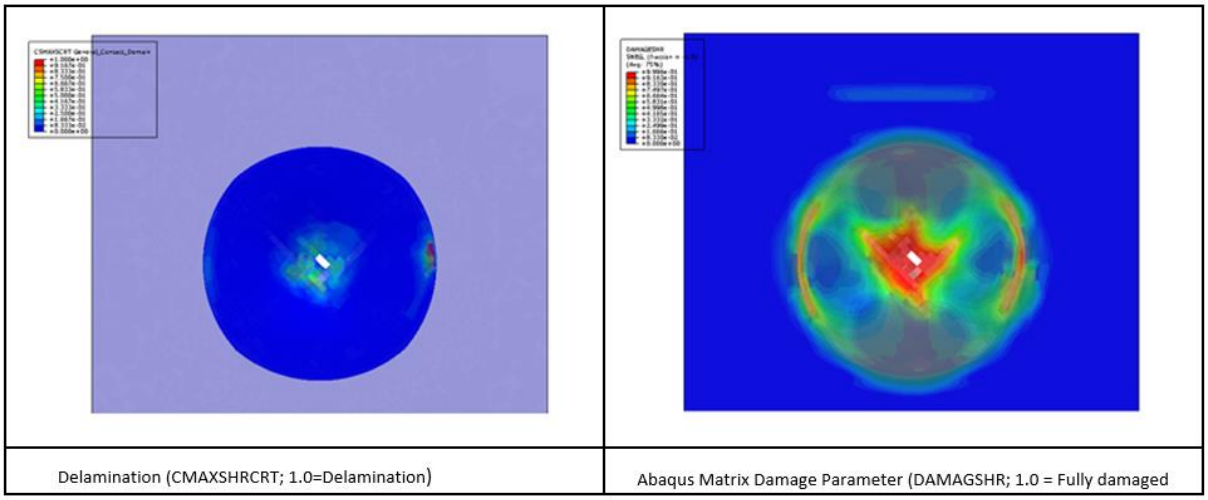


*Figure 5-3: Delamination State (left) and Matrix Damage (right) at peak cross head deflection for $[(0/90)_2]s$ 10J impact*

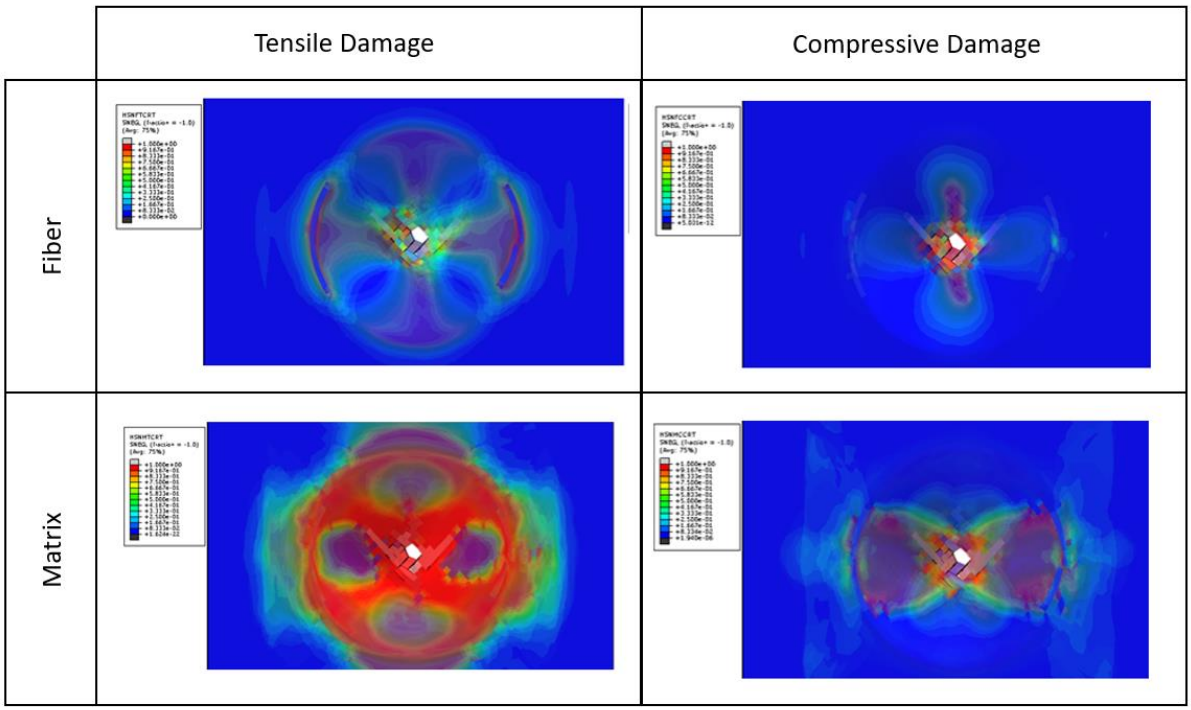


*Figure 5-4: Moving clockwise from the top left: Fibre Tension, Fibre Compression, Matrix Compression and Matrix Tension for the $[(0/90)_2]s$ 10J impact*

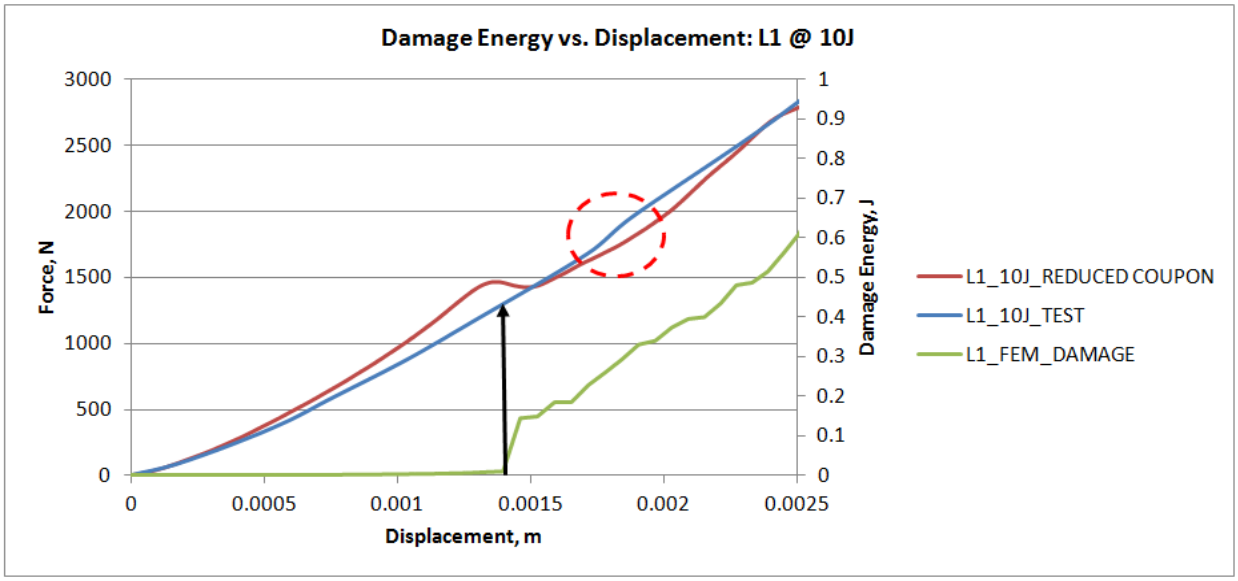


*Figure 5-5: Force vs. Displacement as well as Damage vs. Displacement for the $[(0/90)_2]_s$ 10J case*

The prediction of the onset of damage for this condition under predicts the onset of damage by nearly half a millimeter of displacement, but does predict the onset of damage before the test indicates its first change in stiffness.

### 5.1.2 *Results for $[(0/90)_2]_s$ laminate at 25J*

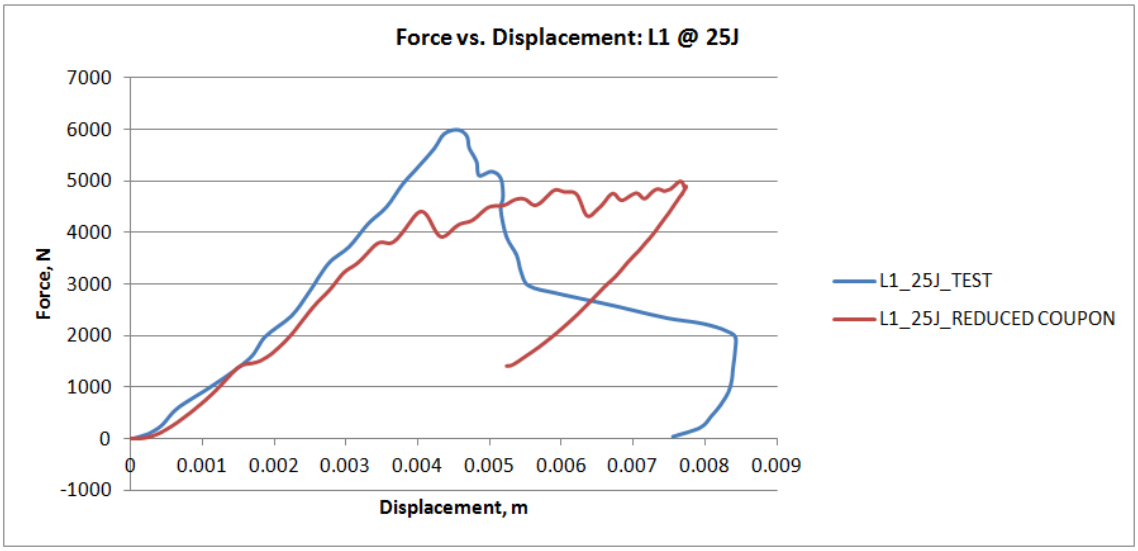


*Figure 5-6: Force-Displacement curve for $[(0/90)_2]s$ 25J impact*

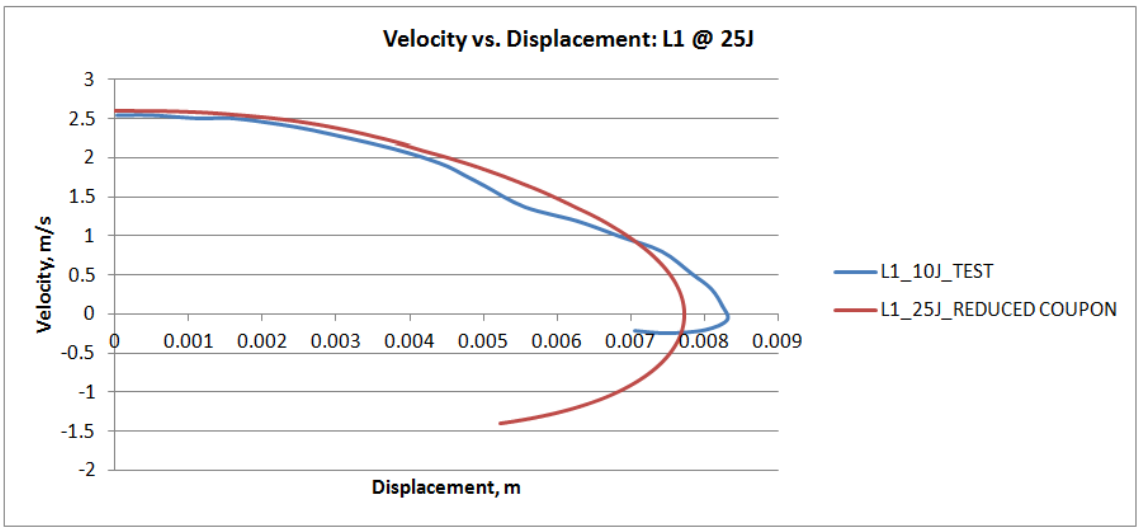


*Figure 5-7: Velocity-Displacement curve for $[(0/90)_2]s$ 25J impact*

Figure 5-6 and Figure 5-7 display the Force-Displacement and Velocity-Displacement curves, respectively, which display reasonable correlation to nearly 4.00mm of displacement. While there is a deviation that begins at 1.60mm of displacement, the curves track well into the post damaged regime of the coupon.

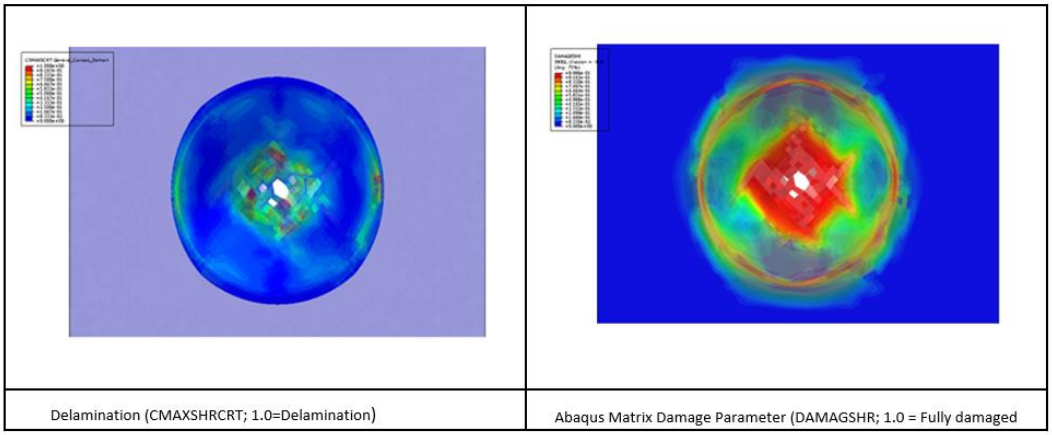


*Figure 5-8: Delamination State (left) and Matrix Damage (right) at peak cross head deflection for $[(0/90)_2]s$ 25J impact*

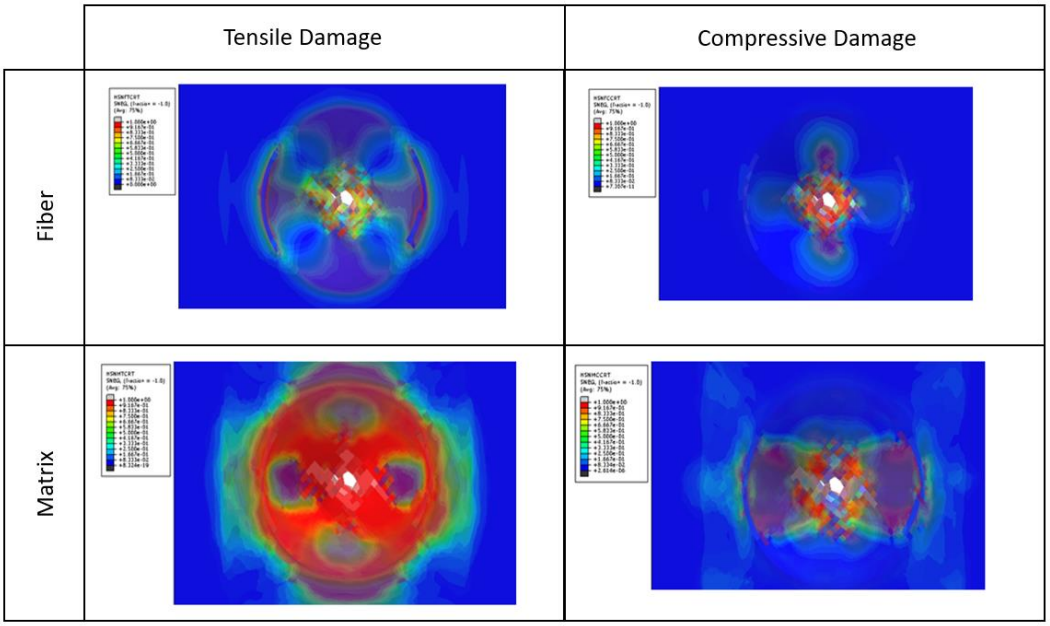


*Figure 5-9: Moving clockwise from the top left: Fibre Tension, Fibre Compression, Matrix Compression and Matrix Tension for the $[(0/90)_2]s$ 25J impact*

The delamination of the coupon is significantly more than the 10J coupon (Figure 5-8) but the majority of the damage in the system comes from the presence of matrix damage as well as fiber damage, which is more prevalent in the 25J case (Figure 5-9). This can be seen at the removal of elements from internal plies; Figure 5-10 shows the element deletion in internal plies, two and seven to display internal material damage, which is representative of the nature of BVID.

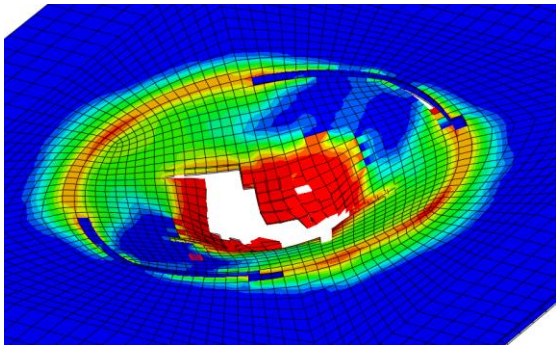

*Figure 5-10: Removal of elements from plies 2 and 7 for the $[(0/90)_2]_s$ 25J case*

While the Force-Displacement curve does not provide much value after 4mm of displacement, the reduced coupon model does accurately predict the onset of damage as seen in Figure 5-11, where the Force-Displacement curves for the FEM and the experiment are plotted along with the damage in the FEM.

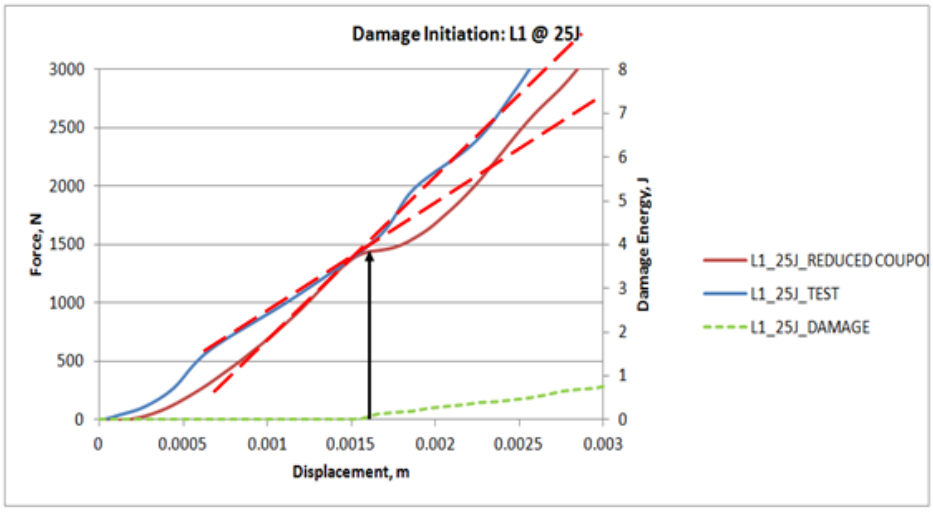


*Figure 5-11: Force vs. Displacement as well as Damage vs. Displacement for the $[(0/90)_2]_s$ 25J case*

At a displacement of 1.6mm the FEM and test Force vs. Displacement curves both experience a change in slope, as the damage in the system begins to increase from zero. The reduced coupon for this condition nearly perfectly predicts the onset of damage in the 25J condition, as the test coupon displays a more pronounced chance in stiffness than the 10J condition did.

### 5.1.3 *Results for $[(45/0/-45/90)]_s$ laminates at 10J*

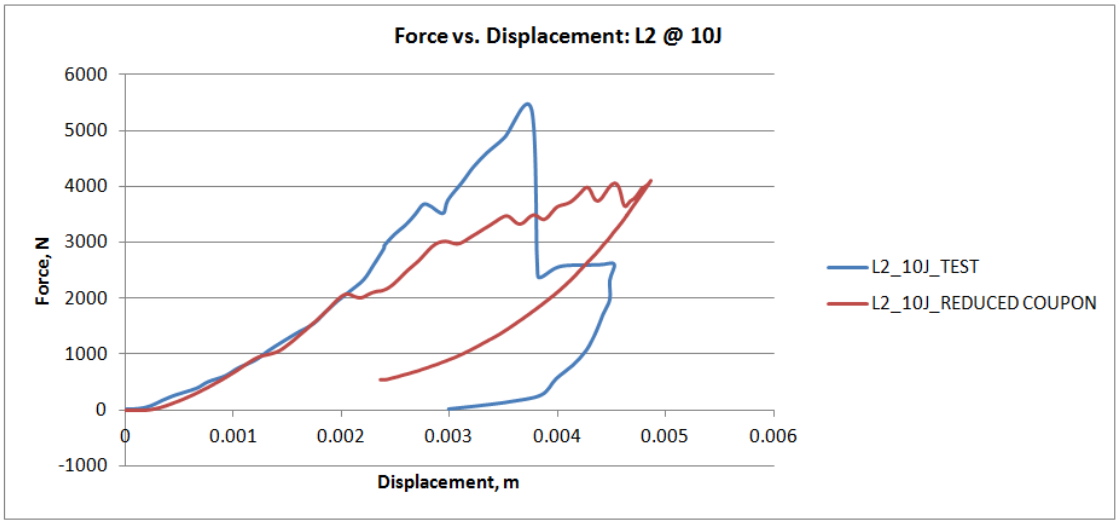


*Figure 5-12: Force vs. Displacement for $[(45/0/-45/90)_2]_s$ 10J impact*

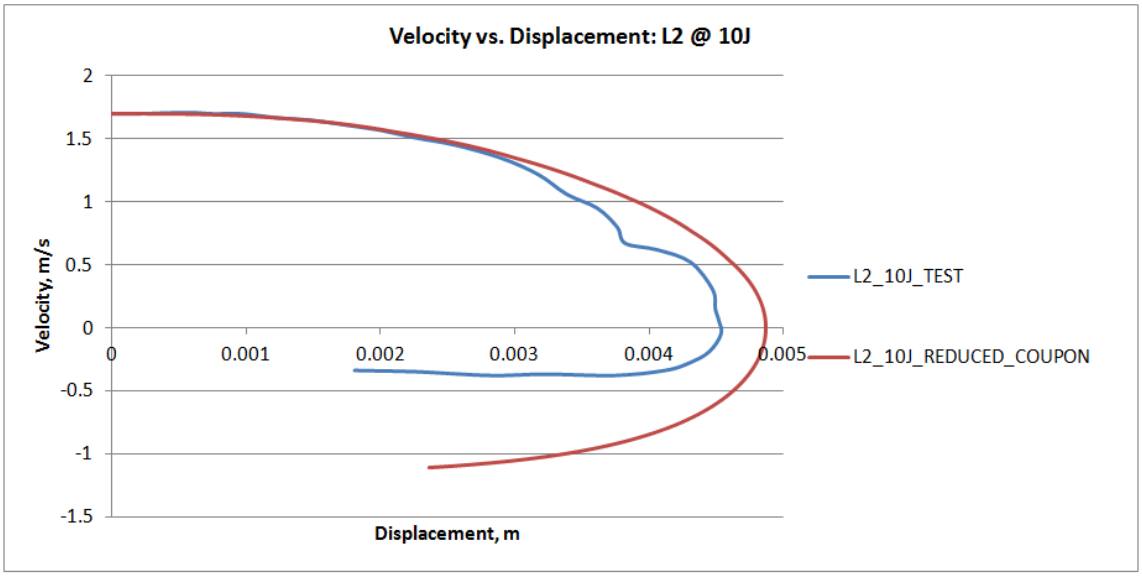


*Figure 5-13: Velocity vs. Displacement for $[(45/0/-45/90)_2]_s$ 10J impact*

Figure 5-12 and Figure 5-13 display the Force-Displacement and Velocity-Displacement curves, respectively, which display reasonable correlation to nearly 2.00mm of displacement. The curves behave in a similar fashion until 3.00mm of deflection, but severely deviate at that point, with the experimental data reaching a much higher peak load than the FEM did.

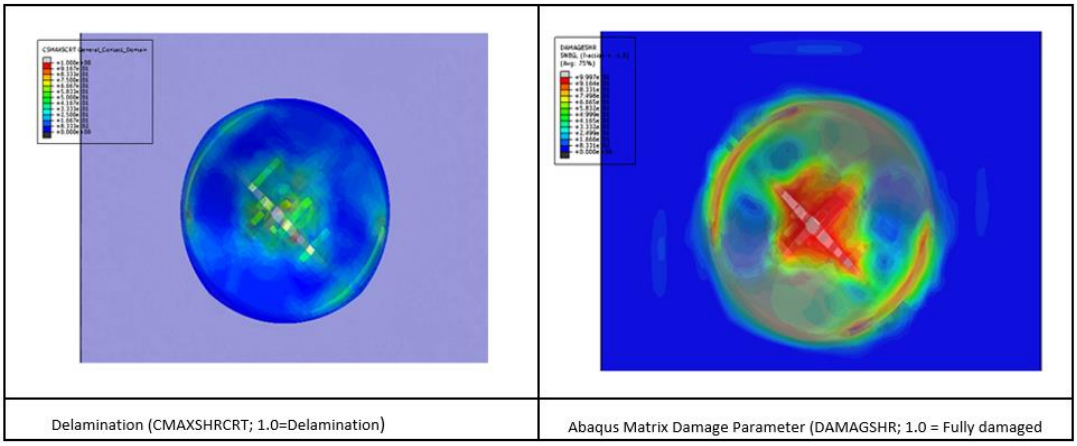


*Figure 5-14: Delamination State (left) and Matrix Damage (right) at peak cross head deflection for $[(45/0/-45/90)_2]s$ 10J impact*

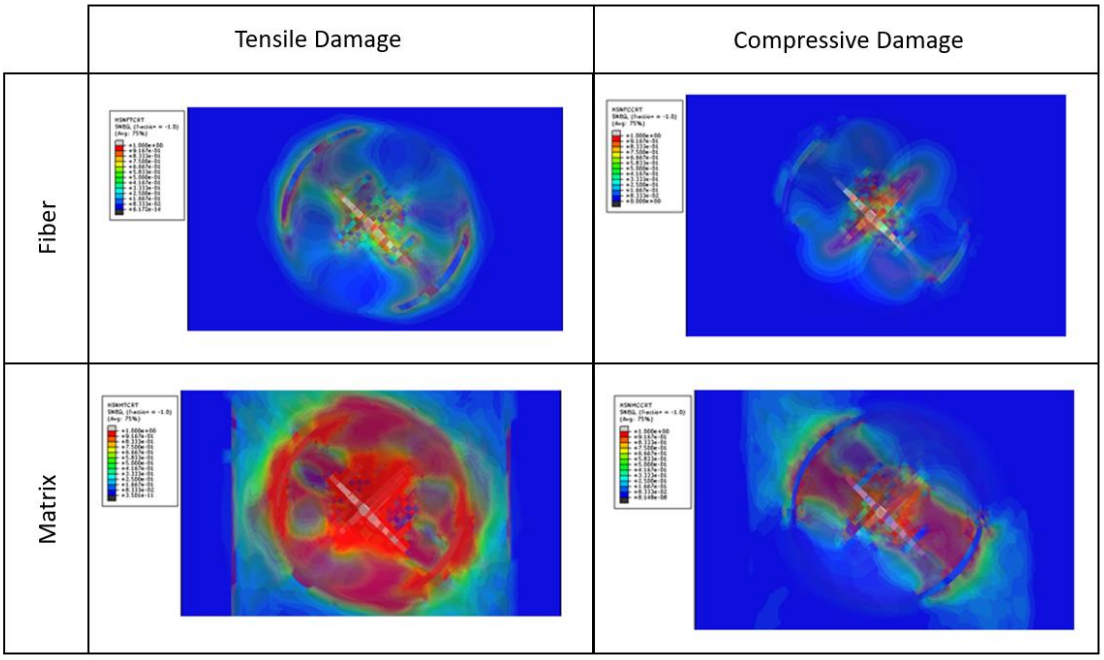


*Figure 5-15: Moving clockwise from the top left: Fibre Tension, Fibre Compression, Matrix Compression and Matrix Tension for the $[(45/0/-45/90)_2]s$ 25J impact*

The damage patterns for this case are significantly different than those for the cross ply laminates, as one would expect due to the presence of off-axis lamina in the quasi-isotropic laminate. However, as with the cross-ply laminate, the delamination in the laminate is limited to a few locations (Figure 5-14) and has significant matrix damage (Figure 5-15). This lay-up also experiences more fiber damage than the $[(0/90)_2]_s$ laminate.

The from Figure 5-16 the damage in the system begins at 2mm of Tupper displacement; after the initiation of damage the reduced model is not able to capture the response of the damaged coupon.

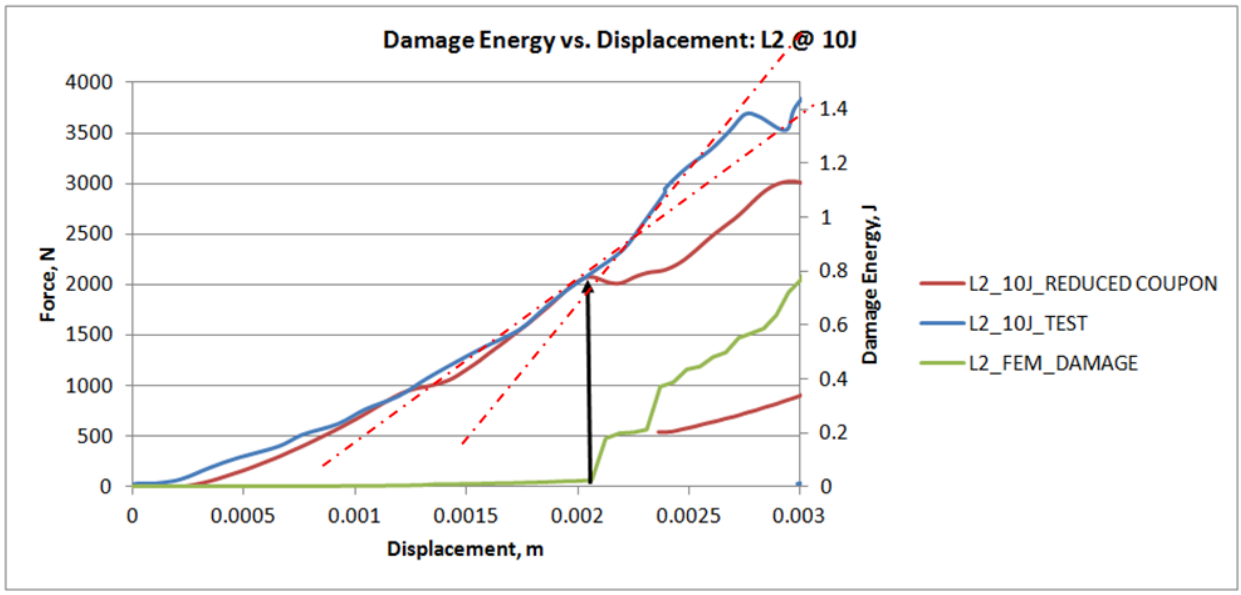


*Figure 5-16: Force vs. Displacement as well as Damage vs. Displacement for the $[(45/0/-45/90)_2]s$ 10J case*

Unlike the cross-ply laminate where the reduced model was able to predict the onset of damage, for the quasi-isotropic laminate the onset of delamination was 0.8mm before the test showed a change in stiffness. While this is not ideal, the reduced coupon does offer a conservative prediction of the onset of damage.

### 5.1.4 *Results for $[(0/90)_3]_s$ laminates at 10J*

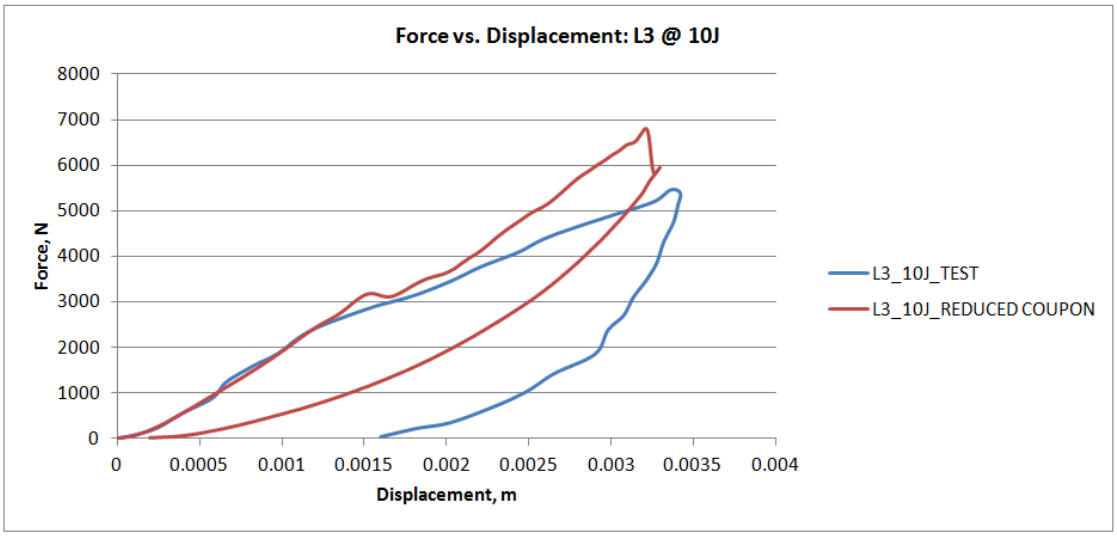


*Figure 5-17: Force vs. Displacement for $[(0/90)_3]_s$ 10J impact*

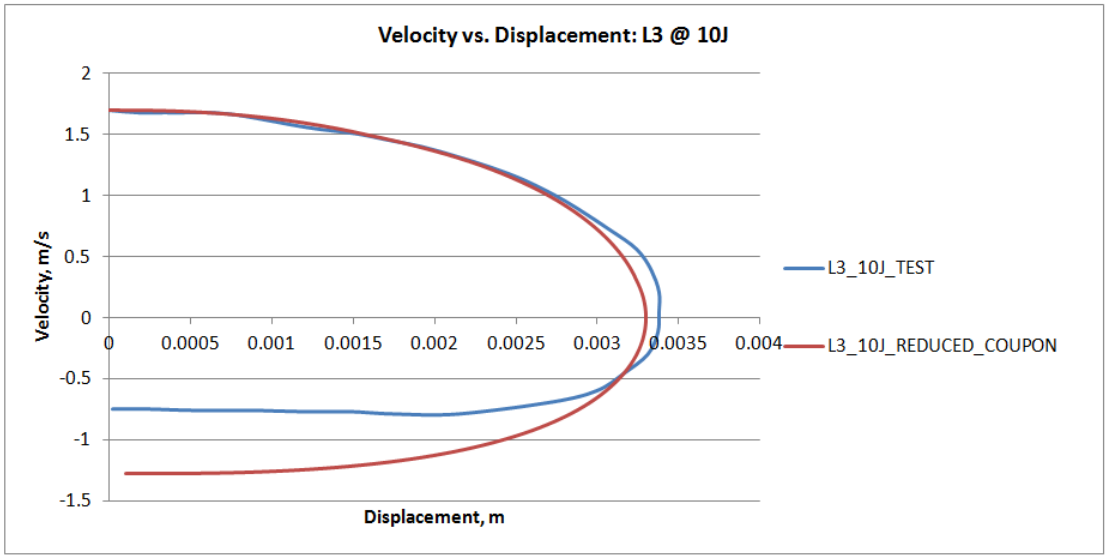


*Figure 5-18: Velocity vs. Displacement for $[(0/90)_3]$s 10J impact*

Figure 5-17 and Figure 5-18 display the Force-Displacement and Velocity-Displacement curves, respectively, which display reasonable correlation to nearly 2.00mm of displacement. The curves behave in a similar fashion until 3.00mm of deflection, but severely deviate at that point, with the experimental data reaching a much higher peak load than the FEM did.

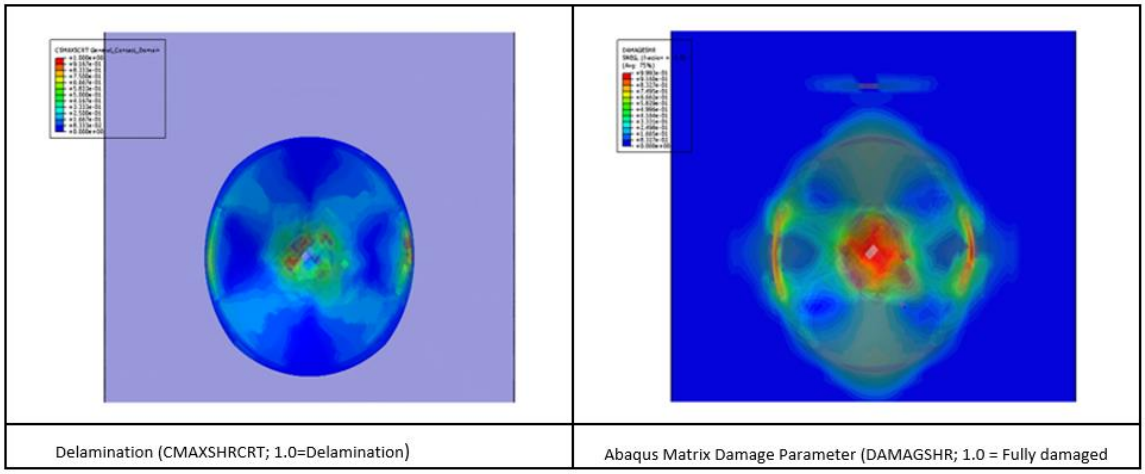


*Figure 5-19: Delamination State (left) and Matrix Damage (right) at peak cross head deflection for $[(0/90)_3]s$ 10J impact*

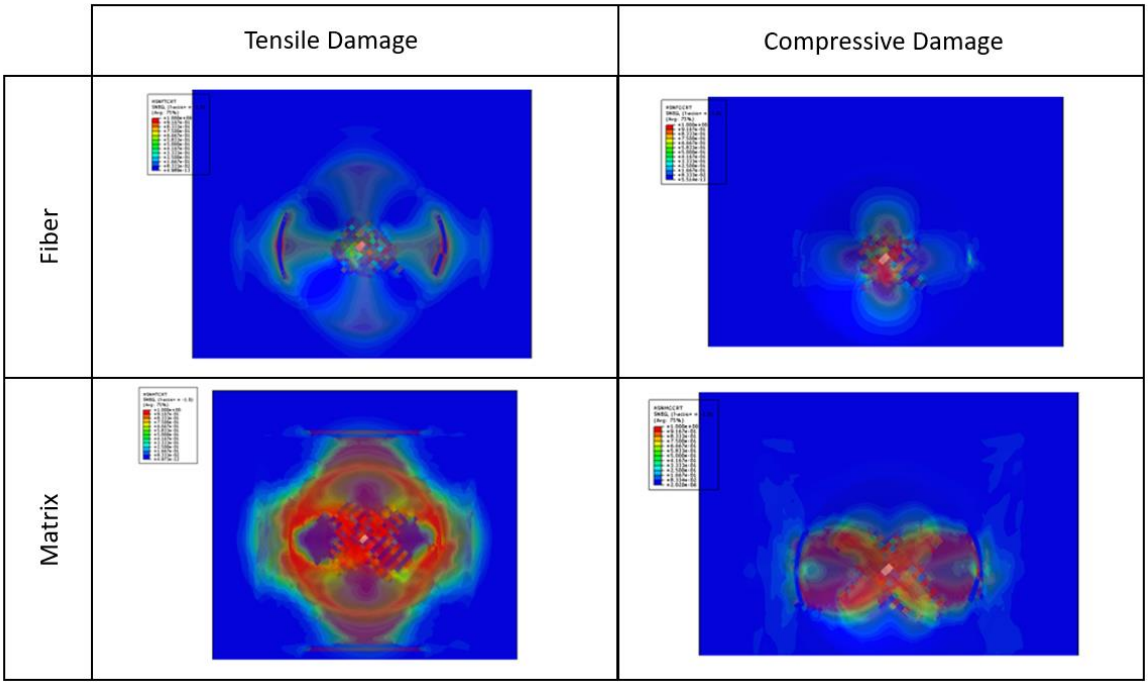


*Figure 5-20: Moving clockwise from the top left: Fibre Tension, Fibre Compression, Matrix Compression and Matrix Tension for the $[(0/90)_3]s$ 10J impact*

Figures 5-13 and 5-14 show reasonable correlation up to 2.5mm of displacement, with the Velocity vs. Displacement curve showing arguable better correlation to nearly 3.0mm of transverse displacement; however the most telling result of this simulation is that the damage energy in the FEM shows a near perfect match to predict the onset of damage in the L3 laminate for 10J energy levels. The following figure shows the change in stiffness of the plate at a displacement of 1.3mm, where is where the FEM begins to predict the onset of damage

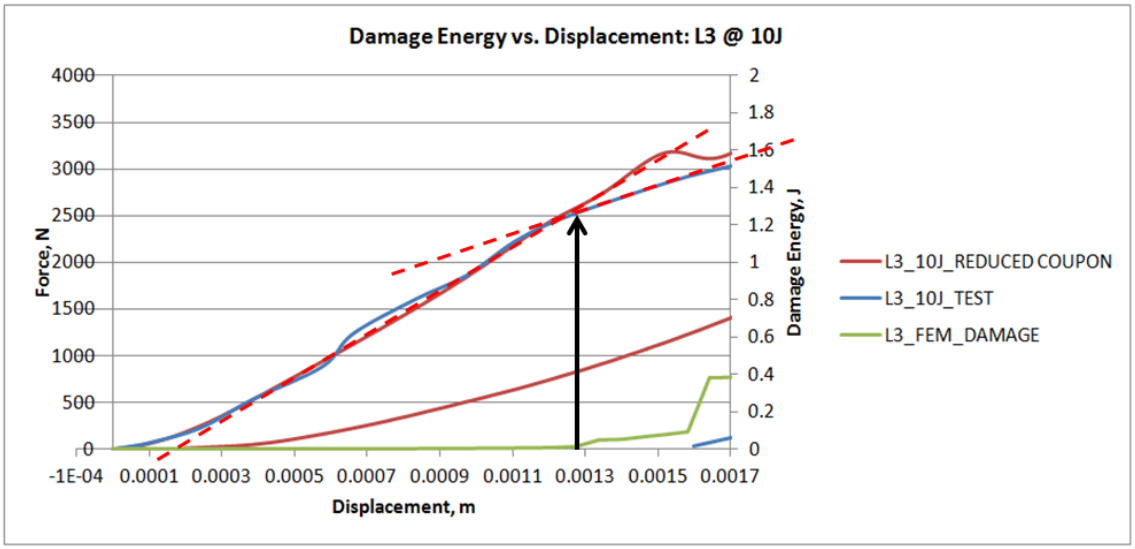


*Figure 5-21: Energy vs. Displacement for $[(0/90)_3]_s$ 10J; shows a clear change in stiffness of the coupon at the point the FEM predicts onset of damage*

In the graphic above, it is clear that there is a change in stiffness of the coupon at 1.3mm of Tupper displacement. This nearly matches the FEM perfectly, as the Damage Energy in the model begins to accumulate at 1.29mm of Tupper displacement. While the post damage response is not exactly the same, the general trend is represented in the Reduced Coupon and the onset of damage is nearly perfectly predicted.

### 5.1.5 *Results for $[(0/90)_3]_s$ at 25J*

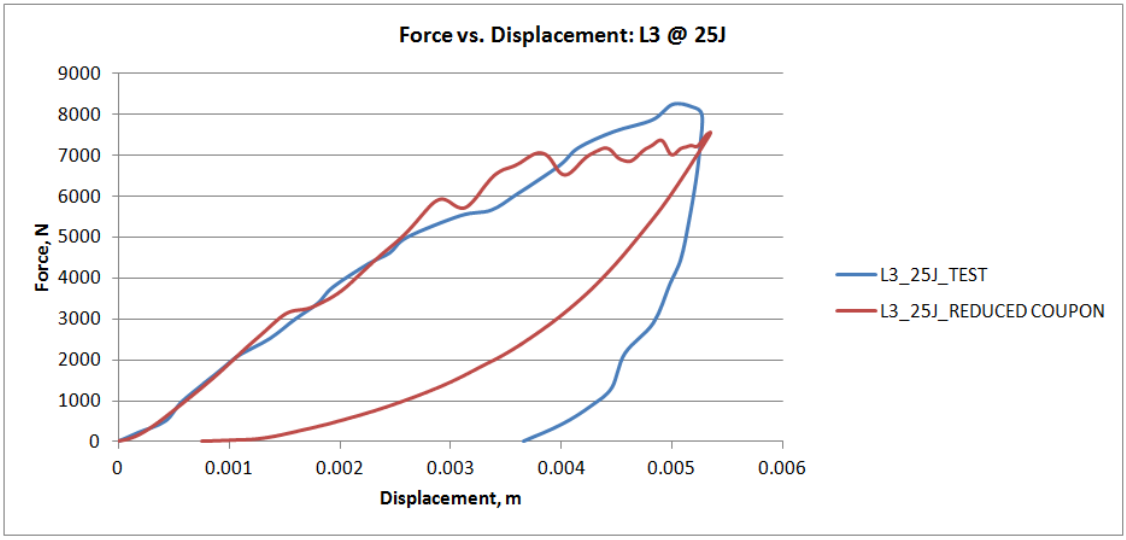


*Figure 5-22:* Force vs. Displacement for $[(0/90)_3]$s 25J impact

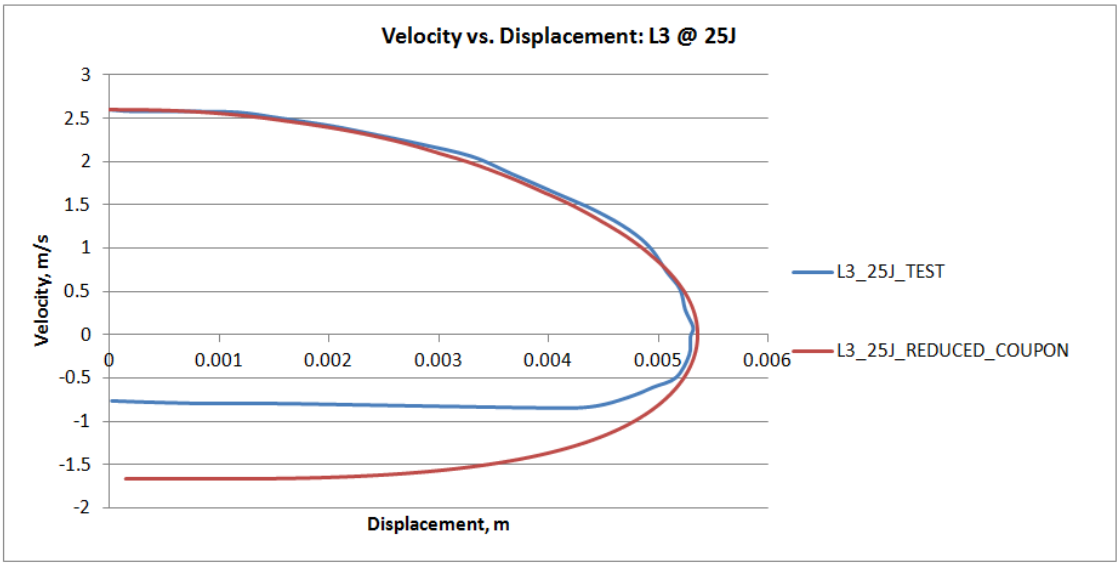


*Figure 5-23: Velocity vs. Displacement for $[(0/90)_3]$s 25J impact*

Figure 5-22 and Figure 5-23 display the Force-Displacement and Velocity-Displacement curves, respectively, which display reasonable correlation to nearly 2.60mm of displacement. The curves behave in a similar fashion throughout the application of load on the plate; once the Tupper

reverses in direction at 5.4mm of displacement, the behavior of the curves deviate, as they have for all simulations.

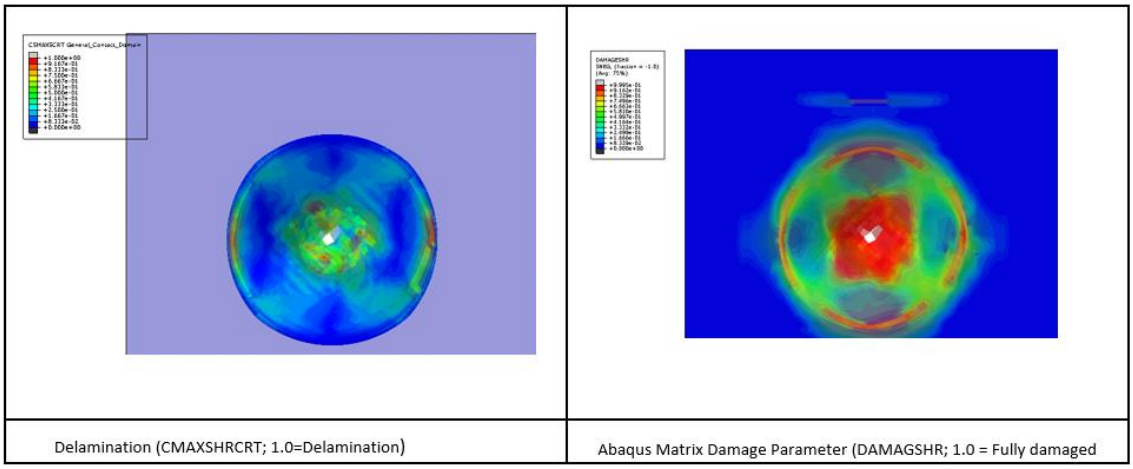


*Figure 5-24: Delamination State (left) and Matrix Damage (right) at peak cross head deflection for [(0/90)$_3$]s 25J impact*

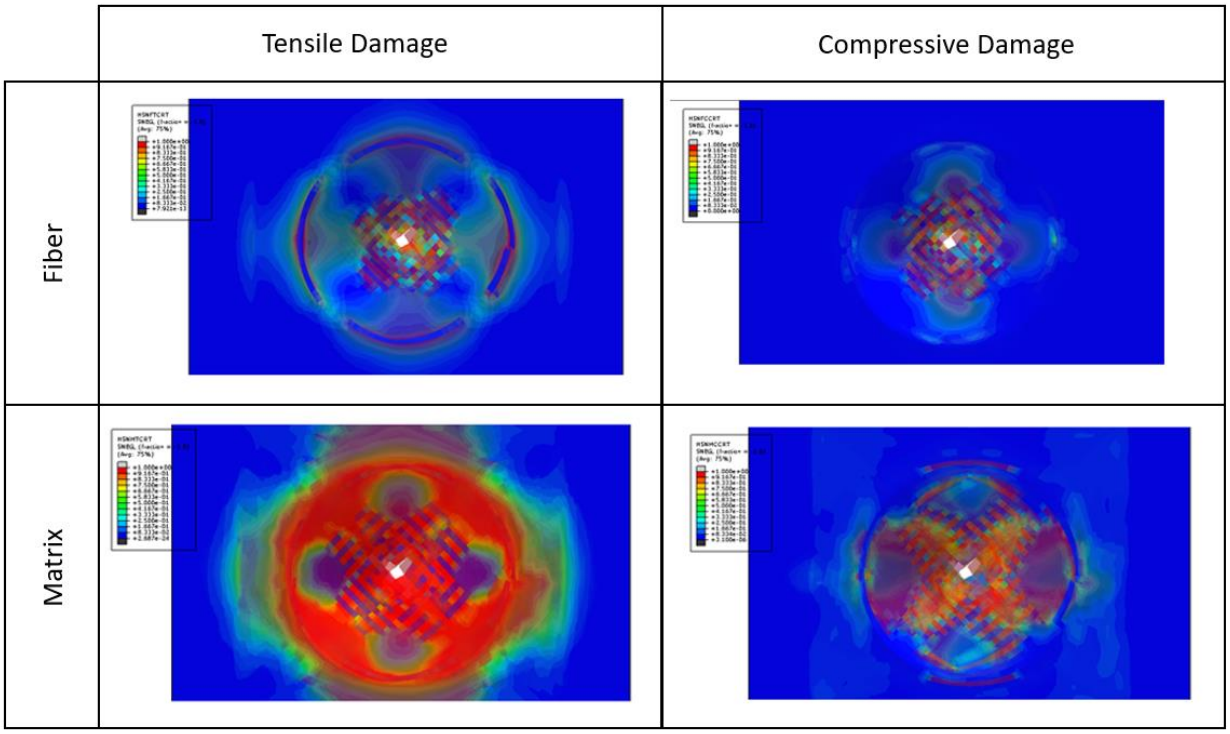


*Figure 5-25: Moving clockwise from the top left: Fibre Tension, Fibre Compression, Matrix Compression and Matrix Tension for the [(0/90)3]s 25J impact*

The damage plots indicate severe matrix damage, as well as significant matrix damage, as displayed in Figure 5-24. The 10J coupon displayed in Figure 5-20 displays a similar damage profile as the 25J coupon, but to a much lesser extent.

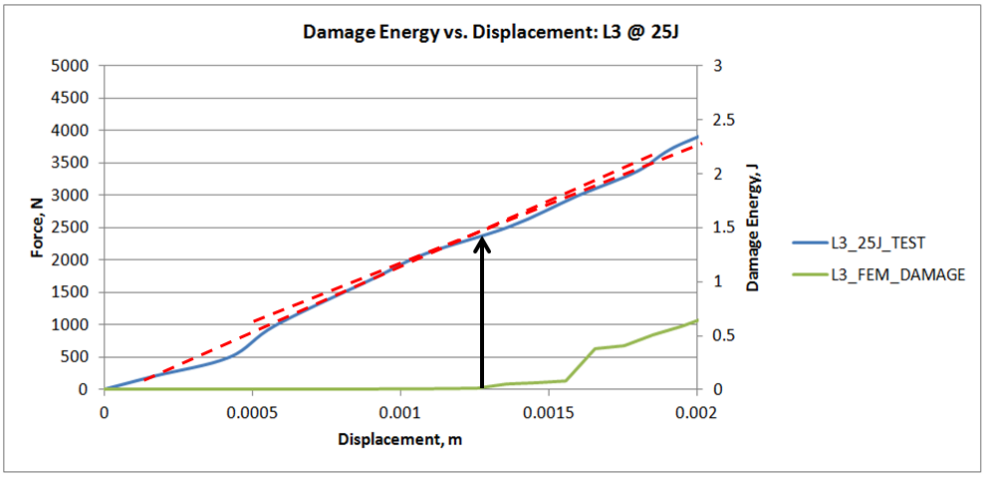


*Figure 5-26: Energy vs. Displacement for [(0/90)3]s 25J; not as clear of a change of stiffness as in the 10J case*

In terms of the damage prediction the coupon does show a small change in stiffness, the change is not nearly as pronounced. The FEM predicts the onset of damage to occur at 1.3mm, as it did with the 10J coupon. While the prediction of the onset of damage is not nearly as clear as it was for the 10J coupon, the reduced coupon does provide a reasonable prediction of the onset of damage, if not a conservative one.

### 5.1.6 *Results for $[(60_2/0_2/-60)_2]_s$ 10J Impact*

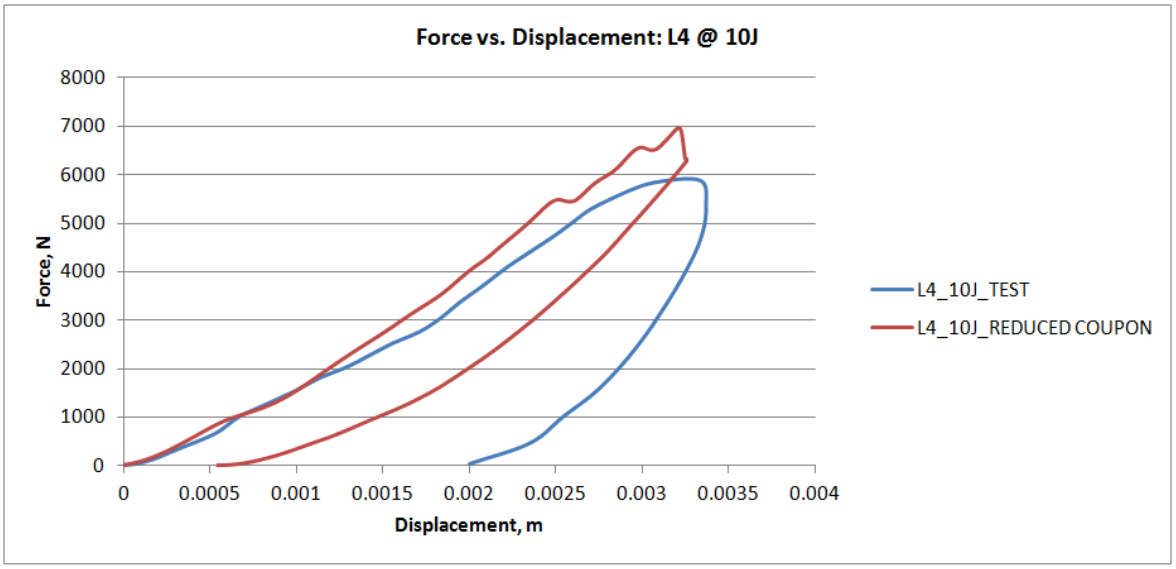


*Figure 5-27: Force vs. Displacement for $[(60_2/0_2/-60)_2]_s$ 10J impact*

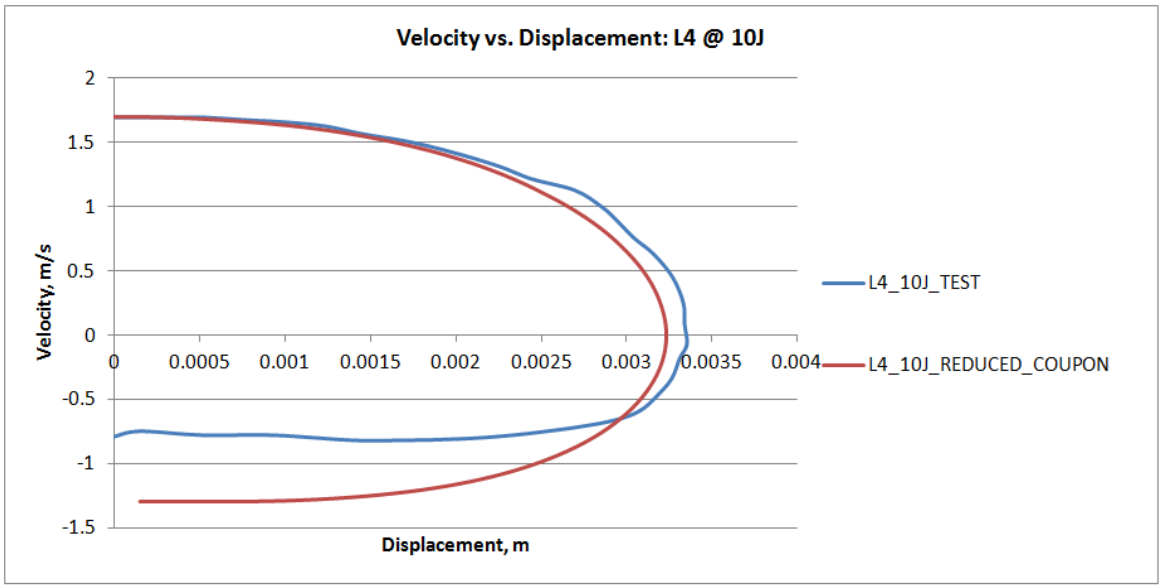


*Figure 5-28: Velocity vs. Displacement for $[(60_2/0_2/-60)_2]_s$ 10J impact*

Figure 5-26 and Figure 5-27 display the Force-Displacement and Velocity-Displacement curves, respectively, which display reasonable correlation to nearly 3.00 mm, which is significant, as this layup does not deflect as much as the others (nearly 25% less than the other conditions).

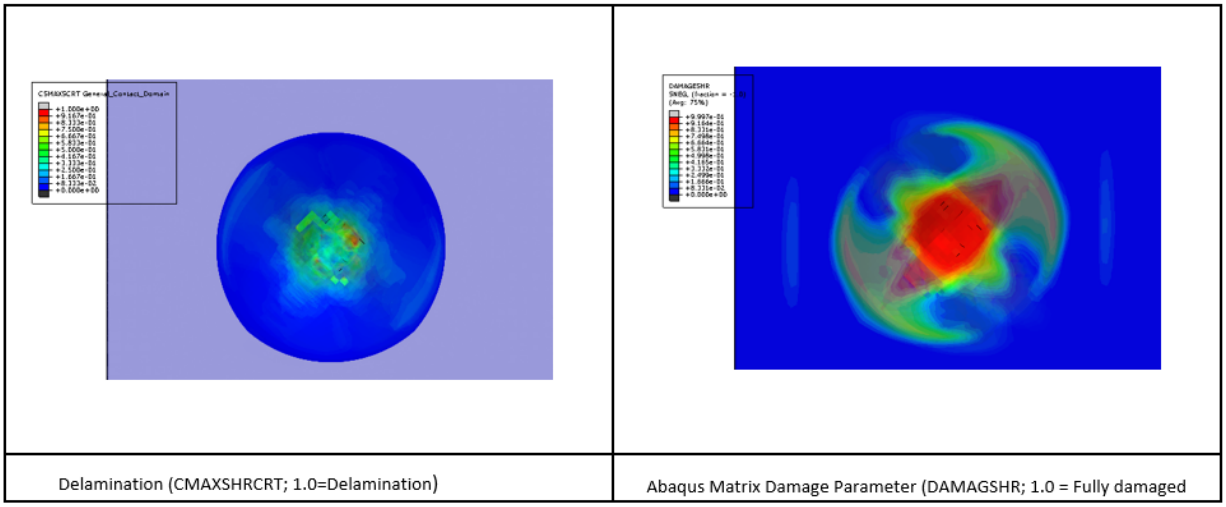


*Figure 5-29: Delamination State (left) and Matrix Damage (right) at peak cross head deflection for $[(60_2/0_2/-60)_2]_s$ 25J impact*

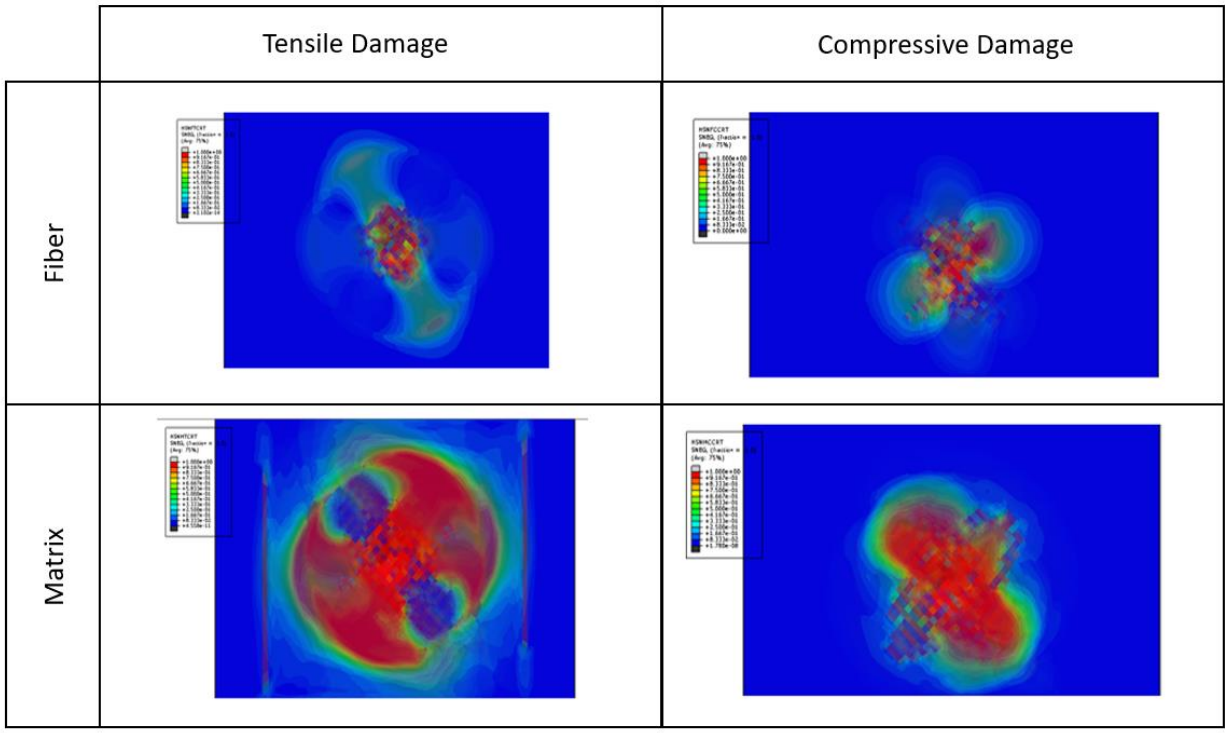


*Figure 5-30: Moving clockwise from the top left: Fibre Tension, Fibre Compression, Matrix Compression and Matrix Tension for the $[(60_2/0_2/-60)_2]_s$ 10J impact*

The Force vs. Displacement curve in Figure 5-22 shows good correlation to nearly 2.25 mm of displacement; the Velocity vs. Displacement in Figure 5-23 also shows good correlation until

2.25mm of displacement. The damage energy in the FEM begins accumulating at 1mm of displacement but is negligible until 1.77mm of Tupper displacement. At this displacement, the test Force-Displacement shows a clear change in stiffness at 1.77mm of displacement matching the where the first appreciable change in damage energy is observed in the FEM.

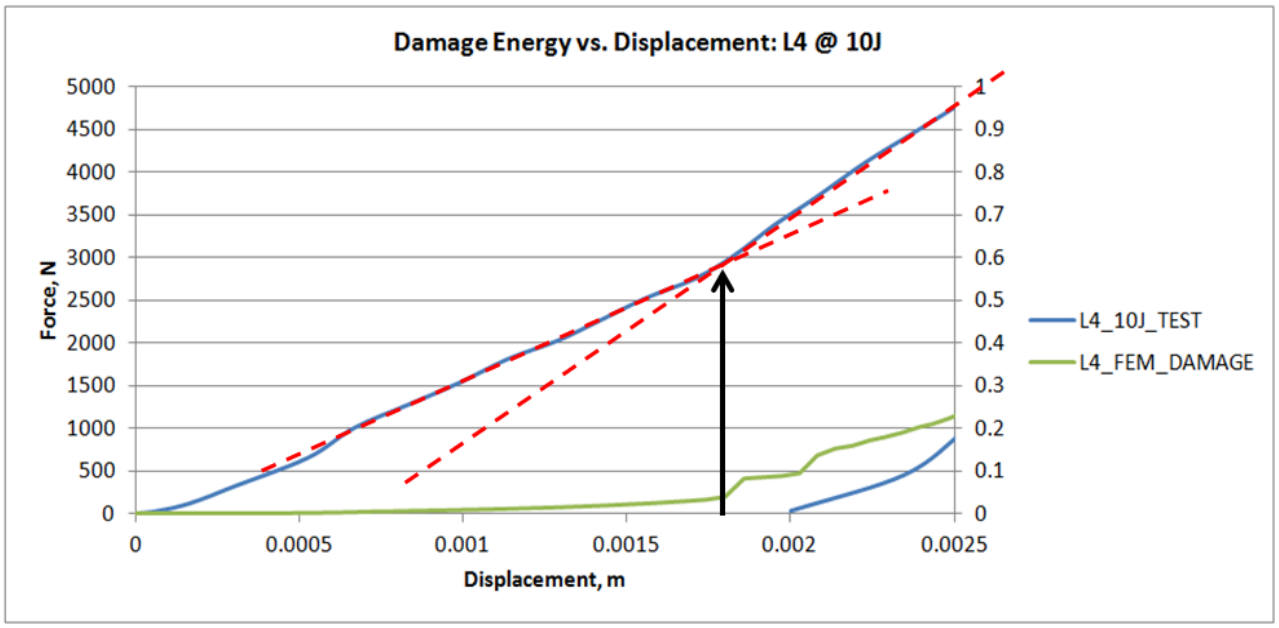


*Figure 5-31: Energy vs. Displacement for $[(60_2/0_2/\text{-}60)_2]_s$ 10J; shows a clear change in stiffness of the coupon at the point the FEM predicts onset of damage*

The FEM provides a good prediction for the onset of damage in the coupon and generally speaking, the FEM also matches the response of the test, but the peak load of 6,955 N is 17.7% higher than the peak load of the coupon.

### 5.1.7 *Result of $[(60_2/0_2/-60)_2]_s$ for 25J Impact*

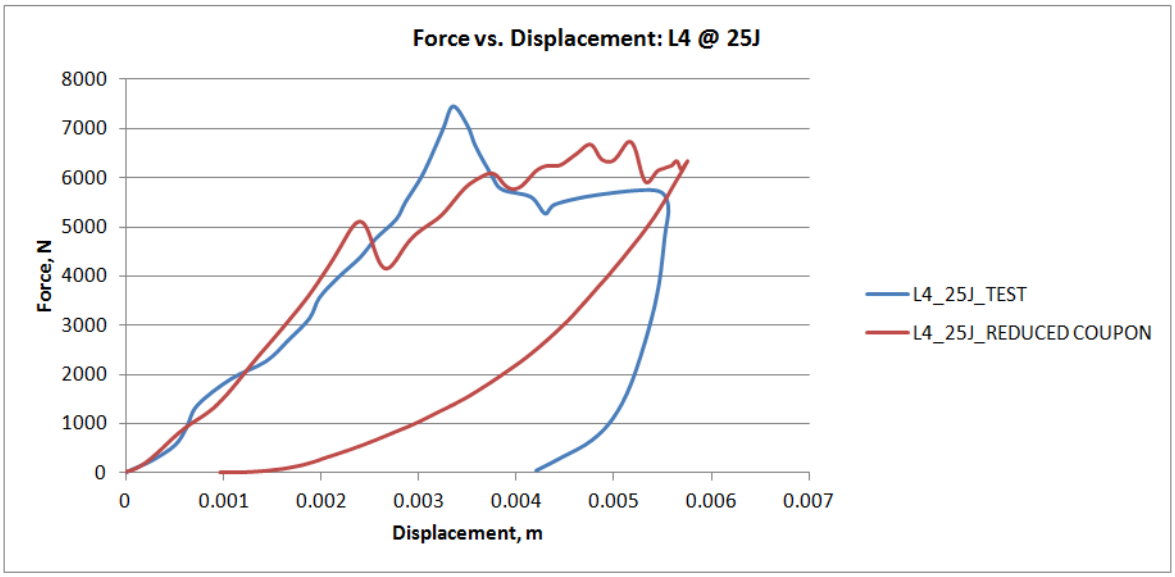


*Figure 5-32: Force vs. Displacement for $[(60_2/0_2/-60_2)_2]s$ 25J impact*

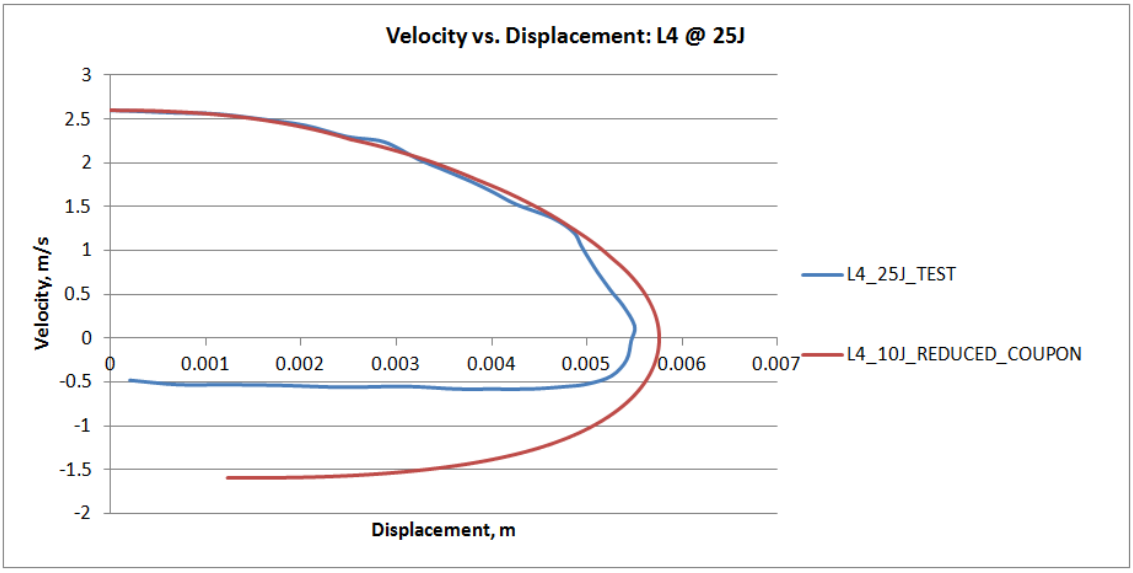


*Figure 5-33: Velocity vs. Displacement for $[(60_2/0_2/-60_2)_2]s$ 25J impact*

Figure 5-30 and Figure 5-31 display the Force-Displacement and Velocity-Displacement curves, respectively, which display reasonable correlation to nearly 2.20 mm, and continues to behave similar to the experimental data until the return of the Tupper.

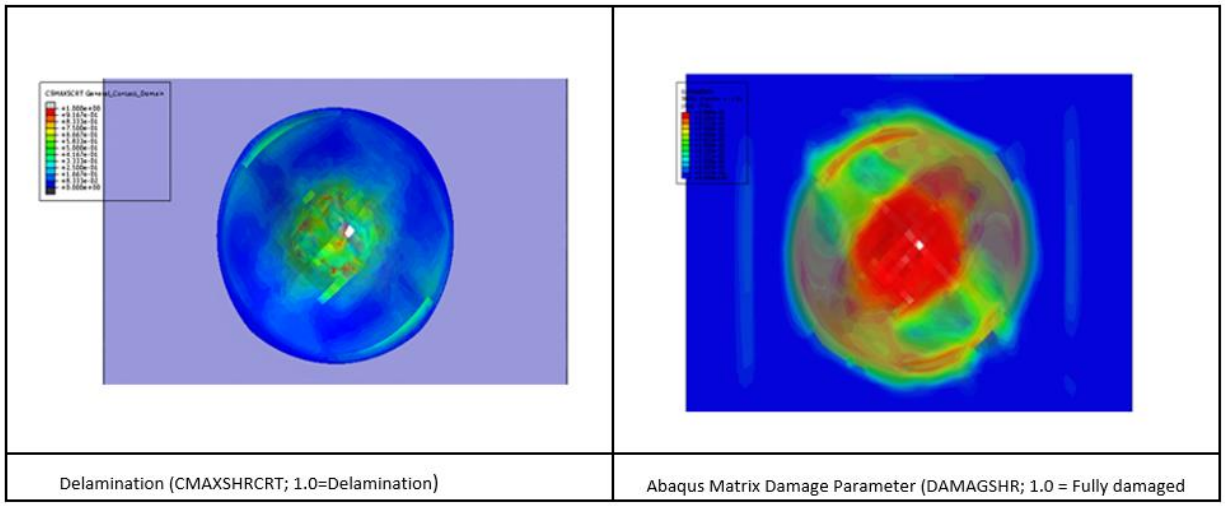


*Figure 5-34: Interlaminar Damage (left and Matrix Damage state variable (right) for the for $[(60_2/0_2/-60)_2]_s$ 25J condition*

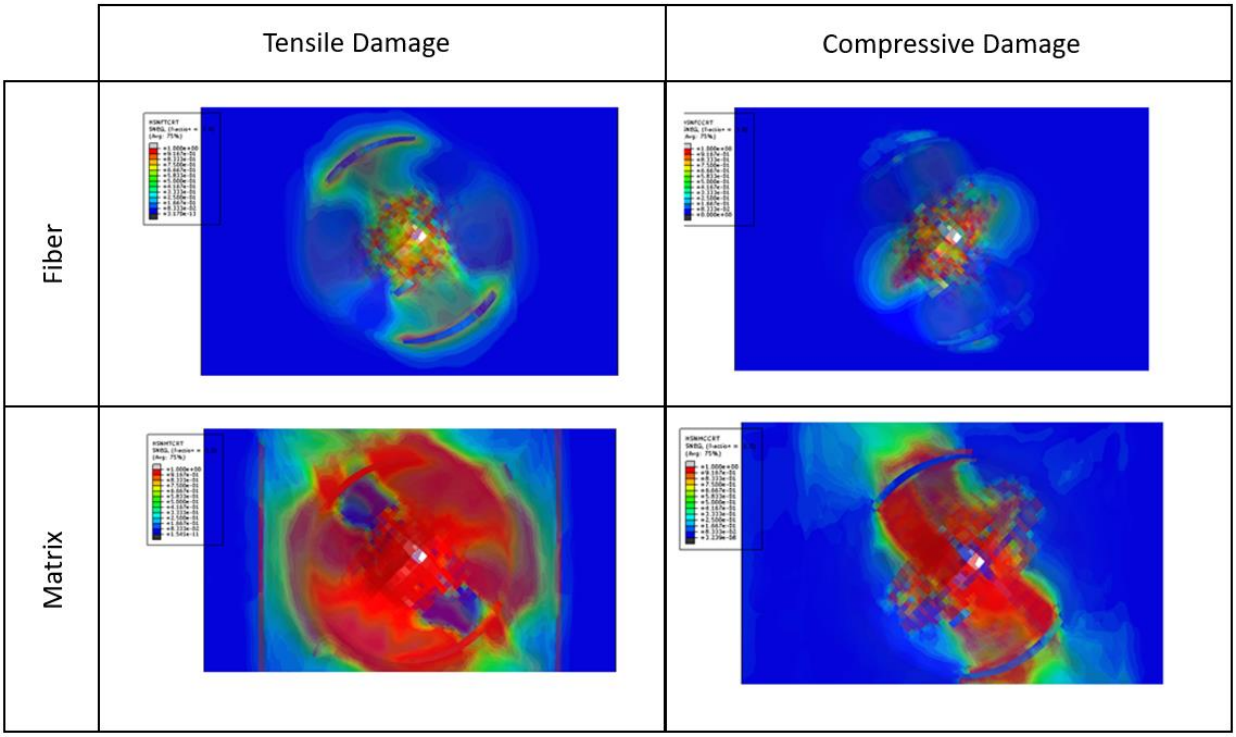


*Figure 5-35: Moving clockwise from the top left: Fibre Tension, Fibre Compression, Matrix Compression and Matrix Tension for the [(602/02/-60)2]s 25J impact*

The Force vs. Displacement curve captures the general trend of the experimental data in Figure 5-33, but does not capture the peak; the Velocity vs. Displacement curve shows very good

correlation until 5.0mm of displacement as well, but does not match in the highly damage regime of the impact event. The damage energy in the FEM begins accumulating at 1.6mm of displacement but is negligible until 1.7mm of Tupper displacement. At this displacement, the test Force-Displacement shows a clear change in stiffness at 1.7mm of displacement matching the where the first appreciable change in damage energy is observed in the FEM.

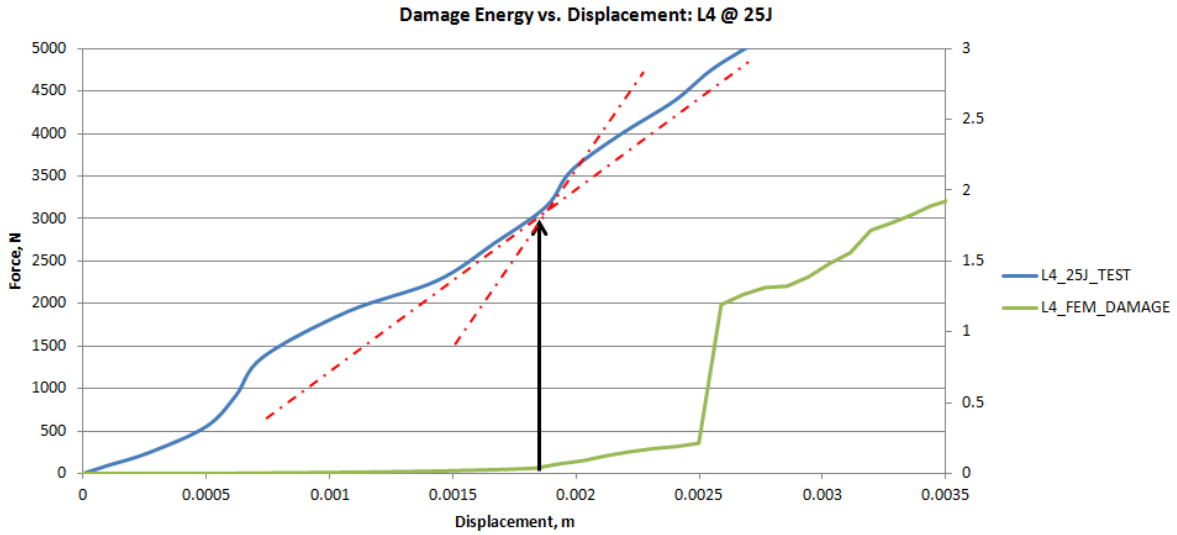


*Figure 5-36: Energy vs. Displacement for [(60₂/0₂/-60)₂]ₛ 25J; shows a clear change in stiffness of the coupon at the point the FEM predicts onset of damage*

The FEM provides a good, if not conservative, prediction for the onset of damage in the L4 coupon for the 25J condition. The change in stiffness of the coupon is noticeable at the displacement predicted by the FEM, but are not as obvious others, hence validating the implication of the prediction being conservative in nature.

## 5.2 FULL TEST SIMULATION

### 5.2.1 *Results for $[(0/90)_3]_s$ laminate at 10J*

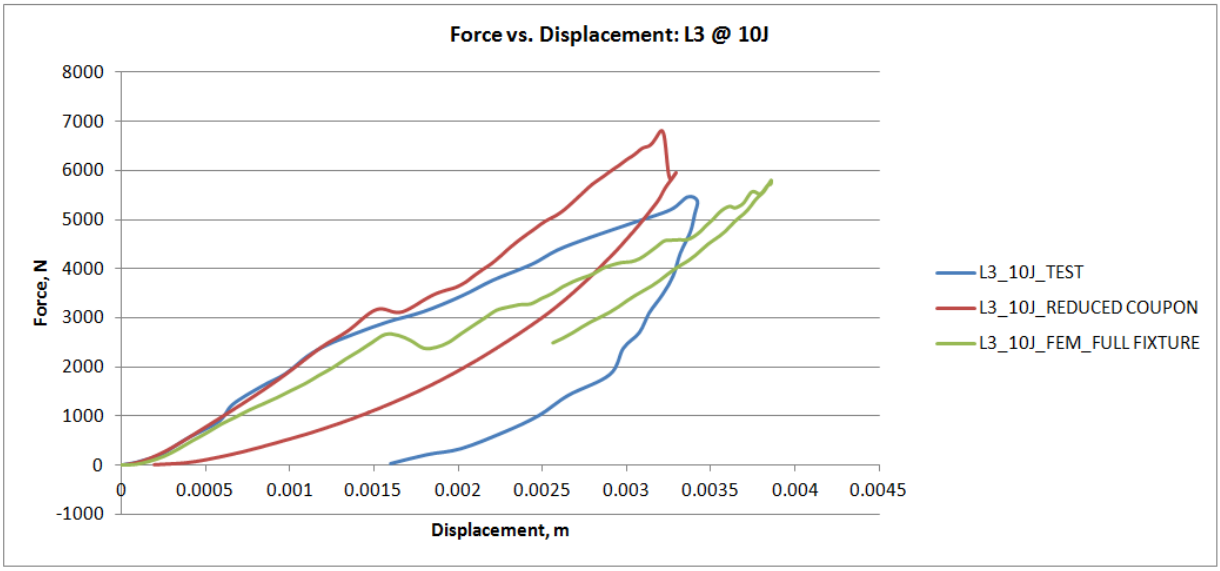


*Figure 5-37: Force vs. Displacement for $[(0/90)_3]$s 10J impact using the full fixture FEM*

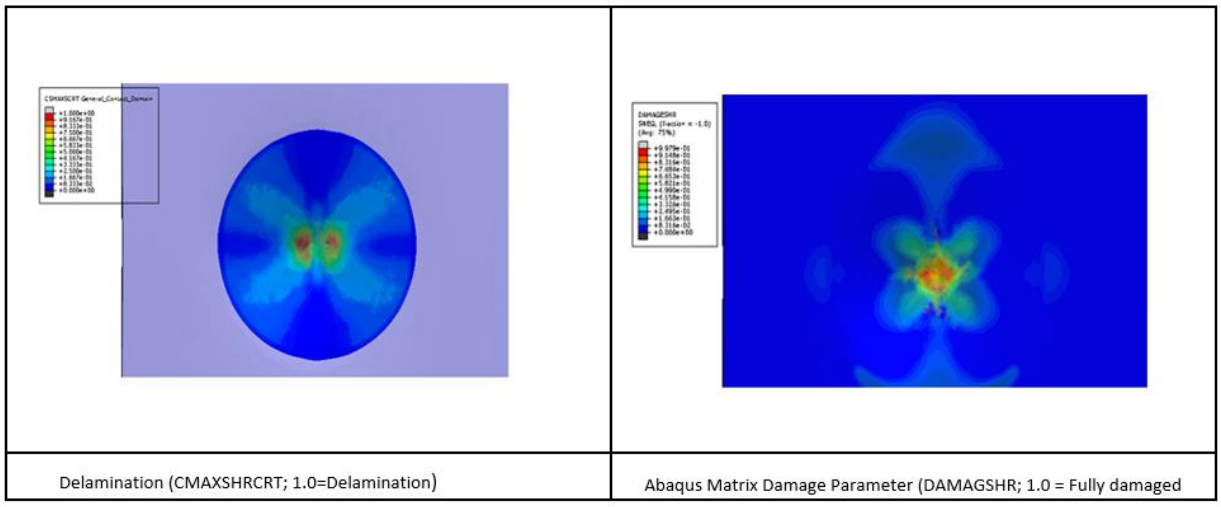


*Figure 5-38: Delamination State (left) and Matrix Damage (right) at peak cross head deflection for $[(0/90)_3]$s 10J impact (Full Fixture)*

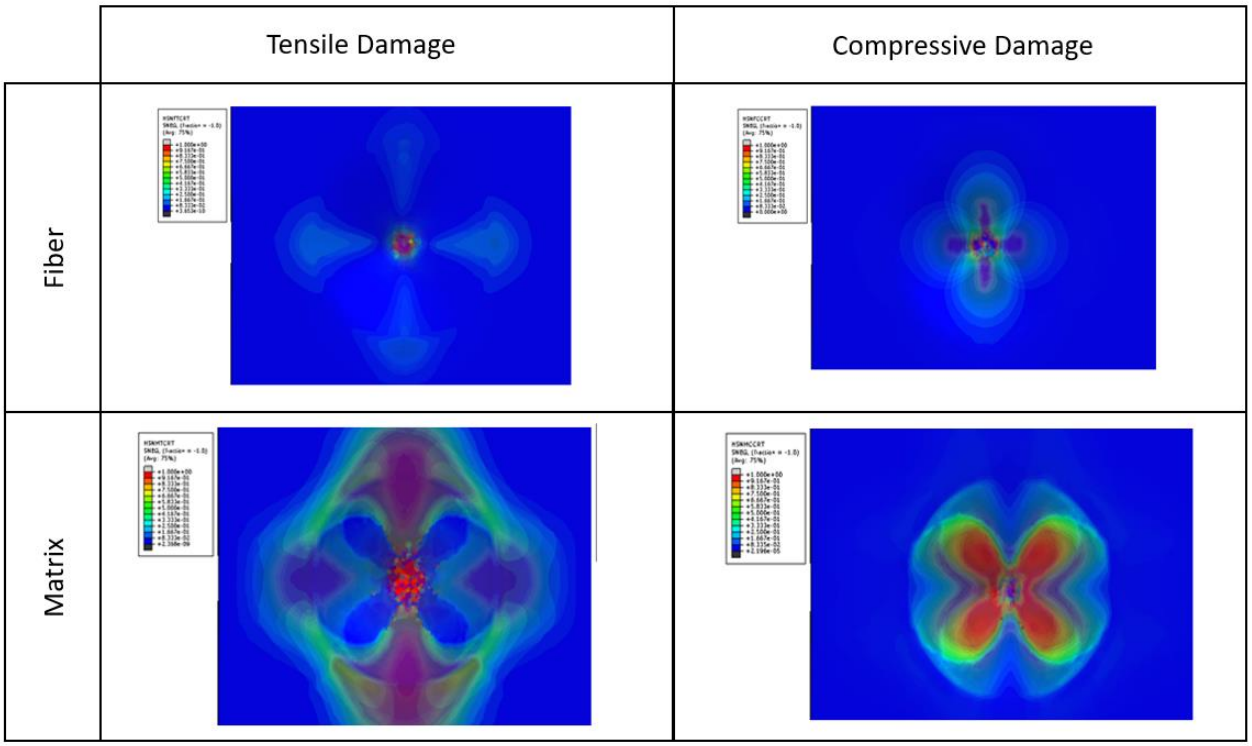


*Figure 5-39: Moving clockwise from the top left: Fibre Tension, Fibre Compression, Matrix Compression and Matrix Tension for the [(0/90)$_3$]s 10J impact (Full Fixture)*

Figure 5-35 displays the Force-Displacement curves for the experiment, as well as the reduced coupon and the full fixture simulation, which shows the Force-Displacement curve for the full fixture being less stiff than the test data and the reduced coupon being stiffer, noticeably after 0.06mm of displacement. This indicates that the configuration of the full fixture may be too compliant.

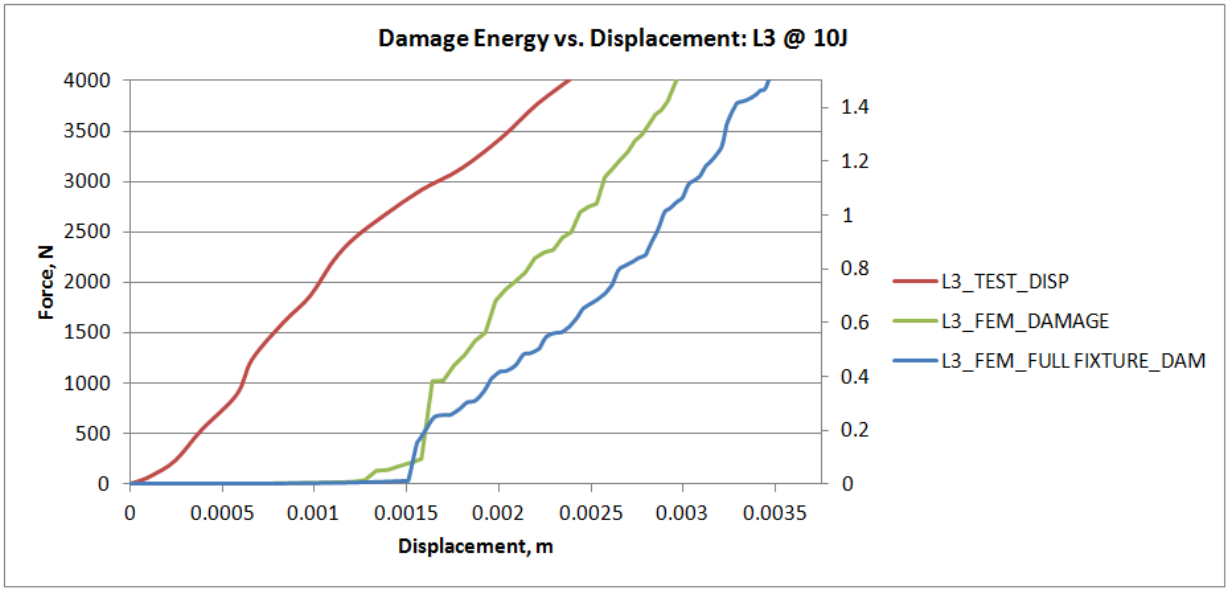


*Figure 5-40: Energy vs. Displacement for $[(0/90)_3]_s$ 10J; detailed FEM predicts a slightly later onset of damage than the reduced coupon.*

The onset of damage in the full fixture model happens at a displacement of 1.50 mm of deflection, versus 1.23mm for the reduced coupon, being a 22.3% difference. Based on Figure 5-21, which shows the change in stiffness occurring at 1.29 mm of displacement, enforces the hypothesis asserted above that the fixture may be too compliant.

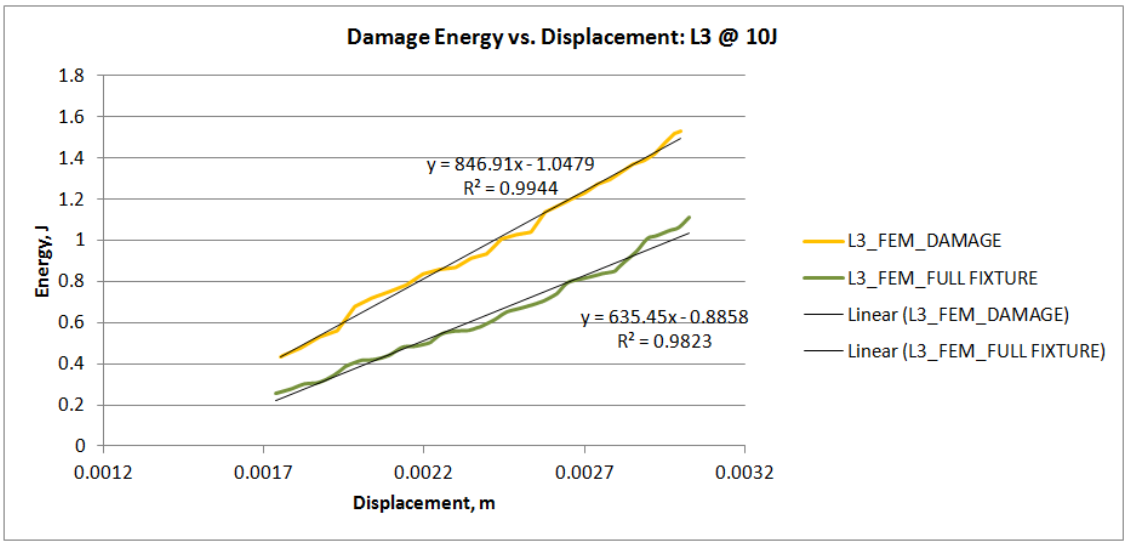


*Figure 5-41: Energy release rate comparison for full fixture and reduced coupon for L1 at 10J*

The slopes of the damage energy curves for the reduced coupon and the full fixture FEM are similar but are 25% different (Figure 5-39), with the full fixture FEM absorbing less energy, enforcing the difference in compliance observed in the forces vs. stroke curves. While the fixture being too soft may affect the onset of delamination, in terms of the damage plots in Figure-36 and Figure -37, the results should still be considered valid and will be compared to the results in Figure 5-19 and Figure-20. The comparisons between the reduced coupon and the full fixture coupons are presented in Figures 5-40 thru 5-42.

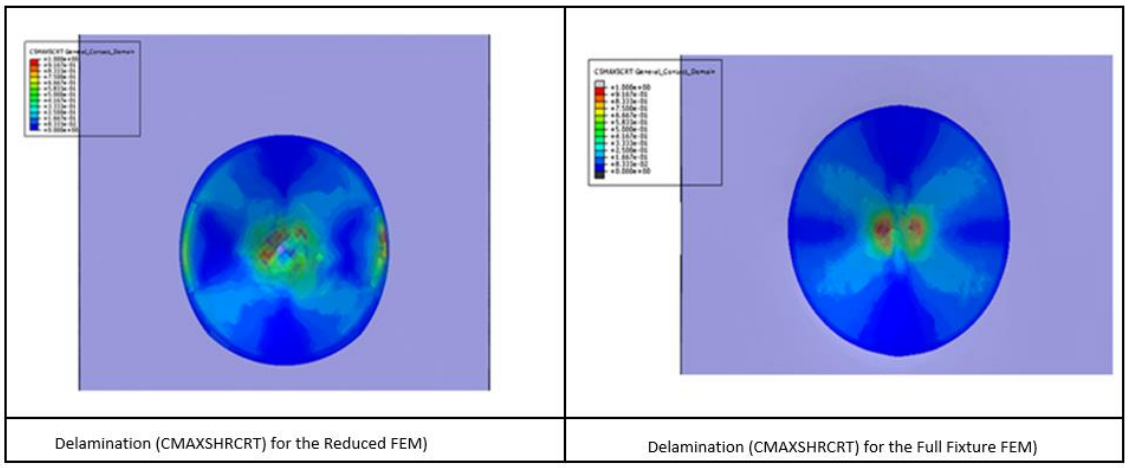


*Figure 5-42: Comparison of the delamination fringes for the reduced coupon (left) and full fixture with the refined mesh (right)*

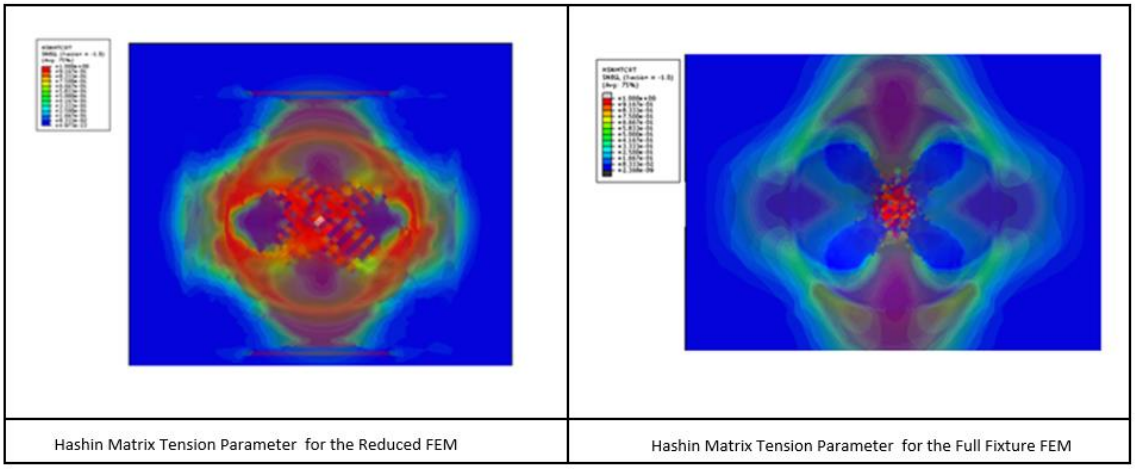


*Figure 5-43: Comparison of the Hashin Matrix Tension Failure variable for the reduced coupon (left) and full fixture with the refined mesh (right)*

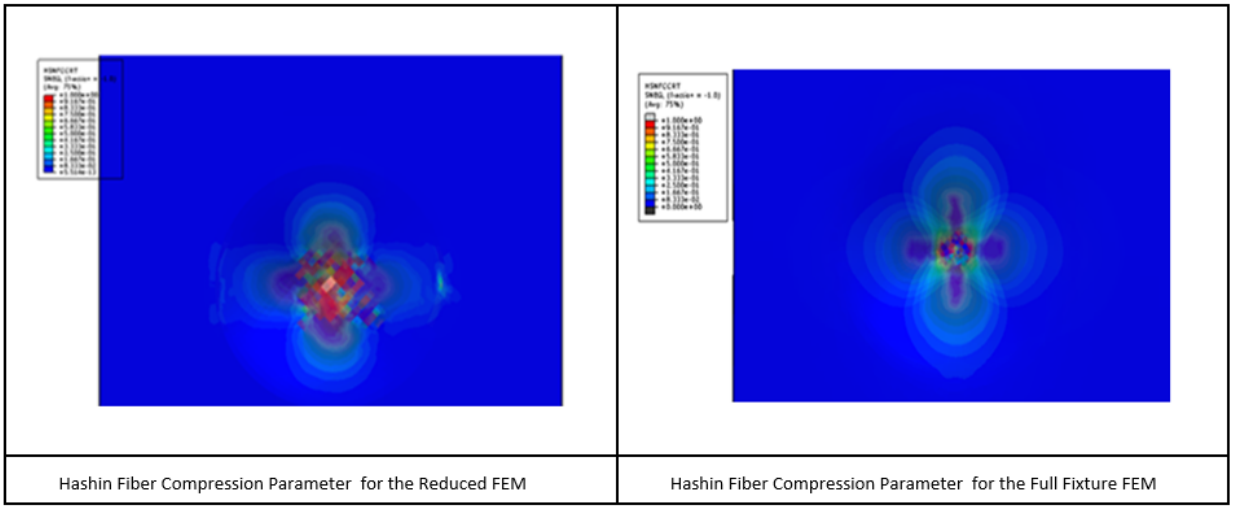


*Figure 5-44: Comparison of the Hashin Fiber Compression Failure variable for the reduced coupon (left) and full fixture with the refined mesh (right)*

The comparison presented in figures 5-40 thru 5-42 displays the same trends between the reduced coupon and the full fixture simulation. Figure 5-41 shows the difference in matrix tension damage parameter, while similar in nature, shows significantly more damage than the reduced coupon. The delamination and the fiber compression variables in Figure 5-40 and 5-42 respectively, display the same trends and similar magnitude, but the with the refined meshes of the full fixture coupons displaying much cleaner transitions when the fringes are viewed with averaged fringe plots.

# Chapter 6. CONCLUSIONS AND RECCOMENDATIONS

From the data presented, the reduced coupon model provides a reasonable means of predicting the onset of damage in the composites subjected to dynamic transverse loading. While the methodology employed was not able to provide sufficient correlation to the Force-Displacement and Velocity-Displacement curves obtained by Briggs [4], particularly in the post damage regime, it did provide a means of predicting the onset of damage in composites that presents itself being fairly inexpensive in using "off-the-shelf" components in a commercial FEA code.

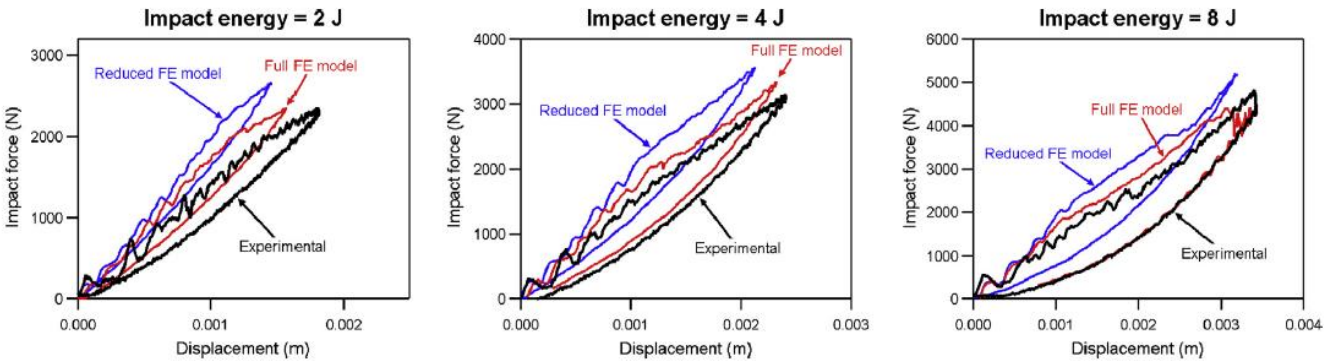


*Figure 6-1: Figure 9 from [10] displaying the same trend in load stroke as displayed in the LVI impact performed in Section 5*

Based on the correlation presented in Figure 6-1, the response predicted above match those obtained by other others in terms of coupon response, leading to the following conclusion that without further testing and characterization of the B450R test fixture, the energy lost to the system and the matching of stiffness's in the FEM to the fixture [14], the post damaged response cannot be accurately characterized. The Force-Displacement curves displayed in figure 8-1 also display the same trend of the fully defined FEM's (which are of much greater fidelity than the reduced model) as observed in this research, which is that the reduced coupons are stiffer in the post damaged response than the test data, which the refined coupons are less stiff than the test data after damage initiation.

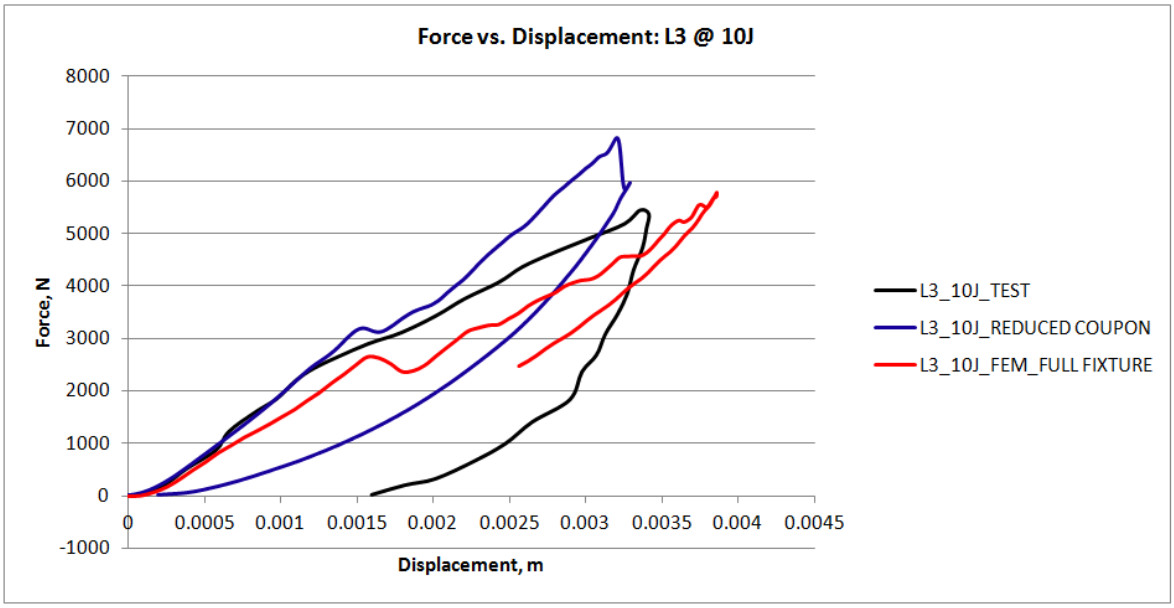


*Figure 6-2: Reduced coupon and full fixture model of the $[(0/90)_3]_s$ 10J condition*

## 6.1 SUMMARY

- Using experimental data collected by Briggs [4], material models were developed for application using the Hashin failure Criterion in Abaqus/Explicit.
- Mode II fracture models are developed using an iterative solution to match the transverse shear stiffness of the Three Point Bend and Edge Notch Failure experimental data.
- Two types of numerical models were generated:
    - Reduced coupon: Velocity based boundary conditions to mimic the B450R testing fixture.
    - Full Fixture: B450R fixture is modeled to obtain more realistic boundary conditions and the mesh of the coupon is finer than those used in the reduced coupons.
- The simulations match the onset of damage in the Low Velocity Impact experiments
- The full fixture simulation provided a near identical answer to the reduced coupon simulations in terms of the ability to predict the onset of damage.

## 6.2 FUTURE WORK

The work performed has provided a good starting point to accurately predict the onset of damage in composites under transverse impact events, but needs to be expanded to be able to predict the state of damage in laminates, particularly through thickness crushing and delamination. Consideration for future work includes:

- Performing experiments similar to those performed in [4, 35] and perform Non-Destructive testing to obtain actual damage patterns in the laminate

- Develop a user defined material model for Abaqus and/or LS-Dyna employing 3D solid elements that considers through thickness damage in laminated materials

- Develop a user defined material model for Abaqus and/or LS-Dyna to evaluate interlaminar fracture

# BIBLIOGRAPHY


[1] Smith, B, "*Centenial of Flight: The Boeing 777*", The Boeing Company, 2003

[2] Marks, P., "*Aviation- The shape of wings to come*", New Scientist, 2005

[3] Davies, G., Zhang, X., "*Numerical Modeling of impact damage in composites*", Composites 25(5) 1994, pp. 342-350

[4] Briggs, T., "*Rate Dependent and Low Velocity Impact Characterization of Composites"*, Ph.D Dissertation, 2010, University of Washington, Seattle, WA

[5] Abaqus Users Manual, version 6.14, Simulia, 2015

[6] Hallquist, J.O., "*LS-DYNA users manual*", LSTC, 2016

[7] Fawcett, A.J., Oakes, G.D., "*Boeing Composite Airframe Damage Tolerance and Service Experience",* The Boeing Company

[8] Shyr, T.W., Pan, Y.H, "*Impact Resistance and Damage Charcteritics of Composite Laminates",* Composite Structures 62, 2003, pp. 193-203

[9] Dhaliwal, G., Newaz, G., "*Modeling Low Velocity Impact of Carbon Fiber Reinforced Laminates (CARALL)"*, Journal of Dynamic Behaviour 99( 2), 2016, pp. 181-193

[10] Laird, G., *www.predictiveengineering.com*

*[11]* Becz, S., Hurtado, J., Lapczyk, I., "*Analysis of Barely Visible Impact Damage for Composite Structures*", 16th International Conference on Composite Materials, 2007

[12] He, Q., Gan, H., Jiao, D., "*An Explicit Time-Domain Finite Element Method That is Unconditionally Stable",* Purdue University, 2011

[13] Fierz, B, "*Stabilizing Explicit Dynamic Finite Element Simulations*", Ph.D dissertation, 2013, ETH, Zurich, Switzerland

[14] Shojaei, A., Guogjang, L., Tan, P.J, "*Dynamic Delamination in Laminated Fiber Reinforced Composites: A Continuum Damage Mechanics Approach*", International Journal of Solids and Structures 71, 2015, pp. 262–276

[15] Feng, D., Aymerich, F., "*Finite Element Modeling of Damage Induced by Low-Velocity Impact on Composite Laminates*", Composite Structures 108, 2014, pp. 161-171

[16] Muflahi, S.A., Mohamed, G., Hallet, S.R.,"*Investigation of Delamination Modeling Capabilites for Thin Composite Structures in LS-DYNA*", 13th International LS-DYNA Users Conference, 2013

[17] Johnson, A.F., Holzapfel, M., "Influence of delamination of impact damage in composte structures", Composite Science and Technology 66, 2006, pp. 807-815

[18] Razi, H., Kobayashi, A.S., "Delamination in Cross-Ply Laminated Composite Subjected to Low Velocity Impact", AIAA Journal 8 (31), 1993

[19] "*Appendix O: The Origins of FEA*", Colorado State University, ME320 Course Notes

[20] Turner, M.J., Clough, R.W., Martin, H.C., "*Stiffness and Deflection Analysis of Complex Structures*", Journal of the Aeronautical Sciences 9 (23), 1956

[21] Benson, J., "*The History of LS-DYNA",* LSTC, 2005

[22] Nimmala, S. "*A Comparison of DYNA3D, NIKE3D and LS-DYNA"*, Oregon State University, 2012

[23] Murakami, S. "*Continuum Damage Mechanics*", Springer Science, 2012

[24] Tuttle, M., "*Structrual Analysis of Polymeric Composite Materials, 2nd edition*", 2012, CRC Press

[25] Hashin, Z., "*Failure Criteria for Unidirectional Fiber Composites*", Journal of Applied Mechanics 47, 1980, pp. 329–334

[26] Matzenmiller, A., Lubliner J., Taylor, R.L., "*A Constitutive Model for Anisotropic Damage in Fiber-Composites*" Mechanics of Materials 20, 1995, pp. 125–152

[27] Hosur, M.V, Alexander, J., Vaidya, J., "*High Strain Rate Compression Response of Carbon/Epoxy Laminated Composites*", Composite Structures 52, 2001, pp. 405-471

[28] Hinton, M.J., Kaddour, A.S, Soden, P., "*A Comparison of the Predictive Capabilites of Current Failure Theories for Composite Laminates Judged Against Experimental Evidence*", Composites Science and Technology 62, 2002, pp. 1725-1797

[29] Hinton, M.J., Kaddour, A.S, Soden, P., "*A Further Assessment of the Predictive Capabilities of Current Failure Theories for Composite Laminates: Comparison with Experimental Evidence*", Composites Science and Technology 64, 2003, pp. 549-588

[30] Federal Aviation Administration, FAA Advisory Curcular AC No: 20-107B, 2009

[31] Mabsen, G., Deobald, L., Dopker, B., "*Fracture Interface Elements for Static and Fatigue Analysis",* 16th International Conference on Composite Materials (ICCM-16), 2003, Kyoto, Japan

[32] Camanho, P., Davila, C., Pinho, S., "*Mechanical Response of Composites",* Springer Science, 2008

[33] Diehl, T., "*Using ABAQUS Cohesive Elements to Model Peeling of an Epoxy-bonded Aluminium Strip: A Benchmark Study for Inelastic Peel Arms*", 2006 , Abaqus Users Conference

[34] Sankar, B.V., "*A Finite Element for Modeling Delamination is Composite Beams*", Computers and Structures 38, 1991, pp. 239-246

[35] Belingardi, G., Vadori, R., "*Low Velocity Impact Tests of Laminate Glass-Fiber-Epoxy Matrix Composite Material Plates",* 2002, International Journal of Impact Engineering 27, pp. 213-229

[36] Wade, B., Feraboli, P., "*Simulating Laminated Composites using LS-DYNA Material Model MAT54 Part I: [0] and [90] Ply Single Element Investigation",* 2012, University of Washington, Seattle, WA

# APPENDIX A: EXPERIMENTAL DATA

Appendix A.1: Longitudinal Extensional Data

| Specimen Label | Loading Rate (mm/min) | E11 (Gpa) | Poisson Ratio | Failure Stress (Mpa) |
|---|---|---|---|---|
| T0_01 | 3 | 137 | 0.18 | 1990.6 |
| T0_02 | 3 | 146.8 | NA | 2061.4 |
| T0_03 | 3 | 130.4 | 0.13 | 1994.4 |
| T0_04 | 3 | 133.4 | 0.1 | 2065.2 |
| T0_05 | 5 | 135.9 | 0.07 | 2259.2 |
| T0_06 | 5 | 132.4 | 0.08 | 1624.9 |
| T0_07 | 5 | 129.7 | 0.08 | 2054 |
| T0_08 | 15 | 133.2 | 0.14 | 2154 |
| T0_09 | 15 | 135.5 | 0.17 | NA |
| T0_10 | 15 | 145.7 | 0.08 | NA |
| T0_11 | 45 | 170.7 | 0.38 | NA |
| T0_12 | 45 | 128.2 | 0.32 | NA |
| T0_13 | 45 | 145.7 | 0.05 | NA |
| T0_14 | 135 | 138.2 | 0.11 | NA |
| T0_15 | 135 | 140.8 | 0.15 | NA |
| T0_16 | 135 | 151.9 | 0.05 | NA |
| T0_17 | 405 | 149.1 | NA | NA |
| T0_18 | 405 | 140.4 | 0.14 | NA |
| T0_19 | 405 | 133.1 | 0.08 | NA |

*Table 14: Longitudinal Extensional data collected by Briggs [4]*

| Loading Rate (mm/min) | Avg E11 | E11_STD | Avg PR | PR_STD |
|---|---|---|---|---|
| 3 | 136.9 | 7.1 | 0.13 | 0.04 |
| 5 | 132.7 | 3.1 | 0.08 | 0.01 |
| 15 | 139.4 | 5.5 | 0.13 | 0.05 |
| 45 | 148.2 | 21.4 | 0.25 | 0.18 |
| 135 | 143.6 | 7.3 | 0.1 | 0.05 |
| 405 | **140.9** | 8 | 0.11 | 0.04 |

*Table 15: Averages of the data in Table 11*

Appendix A.2: Transverse Extensional Data

| Specimen Label | Loading Rate (mm/min) | E22 (Gpa) | Poisson Ratio | Failure Stress (Mpa) |
|---|---|---|---|---|
| T90_01 | 3 | 7.8 | 0.13 | 37.9 |
| T90_02 | 3 | 6.79 | 0.08 | 37.5 |
| T90_03 | 3 | 7.14 | 0.1 | 41 |
| T90_04 | 5 | 8 | 0.17 | 40.1 |
| T90_05 | 5 | 8.83 | 0.14 | 31.1 |
| T90_06 | 5 | 8.91 | 0.14 | 43.6 |
| T90_07 | 15 | 8.26 | 0.1 | 46.4 |
| T90_08 | 15 | 8.75 | 0.14 | 43.4 |
| T90_09 | 15 | 6.48 | 0.08 | 30.7 |
| T90_10 | 15 | 5.23 | 0.07 | 43.1 |
| T90_11 | 45 | 7.75 | 0.13 | 39.4 |
| T90_12 | 45 | 7.14 | 0.09 | 40.7 |
| T90_13 | 45 | 7.7 | 0.11 | 49 |
| T90_14 | 135 | 7.79 | 0.09 | 37.4 |
| T90_15 | 135 | 7.49 | 0.07 | 30.3 |
| T90_16 | 135 | 7.32 | 0.06 | 39.6 |
| T90_17 | 405 | 7.89 | 0.08 | 36.2 |
| T90_18 | 405 | 6.75 | 0.09 | 35.7 |
| T90_19 | 405 | 8.68 | 0.1 | 27.6 |

*Table 16: Transverse Extensional data collected by Briggs [4]*

| Loading Rate (mm/min) | Avg E22 (Gpa) | E22_STD (Gpa) | Avg PR | PR_STD |
|---|---|---|---|---|
| 3 | 7.24 | 0.51 | 0.1 | 0.02 |
| 5 | 8.58 | 0.5 | 0.15 | 0.02 |
| 15 | 7.18 | 1.63 | 0.1 | 0.03 |
| 45 | 7.53 | 0.34 | 0.11 | 0.02 |
| 135 | 7.53 | 0.24 | 0.07 | 0.02 |
| 405 | **7.77** | 0.97 | 0.09 | 0.01 |

*Table 17: Averages of the data in Table 13*

Appendix A.3: Shear Modulus Data

| Specimen Label | Loading Rate (mm/min) | G12 (Gpa) | Failure Stress (Mpa) |
|---|---|---|---|
| G12_01 | 3 | 2.27 | 55.56 |
| G12_02 | 3 | 2.19 | 69.72 |
| G12_03 | 3 | 2.38 | 72.54 |
| G12_04 | 5 | 2.18 | 72.95 |
| G12_05 | 5 | 2.36 | 73.67 |
| G12_06 | 45 | 2.53 | 75.16 |
| G12_07 | 45 | 2.28 | 74.72 |
| G12_08 | 45 | 2.46 | 75.27 |

*Table 18: Shear modulus data collected by Briggs [4]*

| Loading Rate (mm/min) | Avg G12 (Gpa) | G12_STD (Gpa) | Avg Failure Stress (Mpa) |
|---|---|---|---|
| 3 | 2.28 | 0.09 | 65.94 |
| 5 | 2.27 | 0.13 | 73.31 |
| 45 | **2.42** | 0.13 | **75.05** |

*Table 19: Averages of the values in Table 15*

# APPENDIX B: FEA DATA

Appendix B.1: Material Model Data

Material model for uni-directional tape

```
**-------------------------------------------------------------
*Material, name=uni_tape_dam
*Damage Initiation, criterion=HASHIN
2.007e+09,1.264e+09,3.88e+07,6.75e+07,7.5e+07,7.5e+07
*Damage Evolution, type=ENERGY
142954, 56731.99, 982, 2931.95
*Density
1522.,
*Elastic, type=LAMINA
1.409e+11, 7.77e+09,      0.3, 2.42e+09, 2.42e+09, 2.42e+09
```

Material model for interplay data

```
*Surface Interaction, name=interface
*Friction
0.,
*Surface Behavior, pressure-overclosure=HARD
*Cohesive Behavior, REPEATED CONTACTS
 1e+13, 1e+13, 1e+13
*Damage Initiation, criterion=MAXS
 1e+30, 1.4e+08,   1.4e+08
*Damage Evolution, type=ENERGY
2213
```